ACCURACY IMPROVEMENTS OF NIRS AND INVESTIGATION OF MUSCLE OXIDATIVE METABOLISM

by

Ömer Şayli

B.S., E.E., Boğaziçi University, 1999

M.S., E.E., Boğaziçi University, 2002

Submitted to the Institute of Biomedical Engineering

in partial fulfillment of the requirements

for the degree of

Doctor

of

Philosophy

Boğaziçi University

2009

ACKNOWLEDGMENTS

Looking back, there were difficult times.. Praise be to Allah..

I am grateful to my family for their patience and support. I also like to thank my relatives and friends.

I'd like to thank to my thesis advisor Assoc. Prof. Dr. Ata Akın. His enthusiasm about the NIRS motivated a lot of theses, including this one. I have been in his lab. group from nearly the beginning, and being in this group acquired me experience in clinical studies on muscle metabolism and brain hemodynamics, and mentoring some master thesis studies. I also had opportunity of witnessing to stages of development of a device we used in our measurements.

I thank to the anonymous reviewers of Journal of Optics Express who rejected an earlier version of our article on fat effect on NIRS measurements. The comments and suggestions of these reviewers really helped us a lot in shaping the direction of our research, in making us clear what can we do. This study was changed to different content and published, however in another journal. I also like to say I have benefited a lot from our group member and Ph.D. student E. Burteçin Aksel who has Physics degree. He has been the other person in our group who worked using Monte Carlo simulations. Our discussions on the Monte Carlo simulations and his help on the points where I needed assistance helped me a lot.

Thanks to the staff of Instrumentation Lab. including Uzay E. Emir, Murat Tümer, Ercan Kara and Deniz Nevşehirli. Uzay was the leading person in the development of NIRS device and was involved in all first studies on brain and muscle measurements in the lab. He really gave a big effort. His dedication to the lab. and his work discipline were big factors in the progress of NIRS studies in our lab. Murat Tümer made a big contribution to the development of NIRS device which we used in

our measurements, moreover he did maintenance of it. I'd like to thank also Hasan Ayaz, Emir Alkaş and Ömer Sever, who have written versions of NIRS software. Ercan Kara and Deniz Nevşehirli made a lot help in maintenance and improvement of NIRS device as well as solving numerous technical difficulties we have encountered.

I would also like to all the people in our group and in Biomedical Engineering Institute, including Mustafa Zahid Yıldız, Fatih Akkentli, Yüksel Yazıcı, İsmail Burak Parlak, Gökçen Yıldız, Sinem Burcu Erdoğan, R. Koray Çiftçi, Elif Kubat, Deniz Duru, Özgür Tabakoğlu, Özgüncem Bozkulak, Gökhan Ertaş, Hakan Solmaz, Yahya Civelek, Serkan Karaca, Barış Özkerim, Serhan Kalsın, Nermin Topaloğlu, Mehmet Kocatürk, Volkan Taşçıoğlu and Erhan. The friendly environment in this Institute deserves to mention.

I will always remember our group member Mustafa Fidan who we lost in an airplane accident, among other people and bright scientists. May Allah have mercy on them.

Other students in our group whom we worked together all made contributions to the thesis, since we were also new to the topic. Their studies were all progression steps in our studies. The muscle studies were in fact started with the master theses works of Devrim Erdem, Akın Yücetaş, Nihan Yıldırım. The muscle study part of this thesis could not be done without the experience and knowledge we acquired in these studies. I'd like to mention Devrim Erdem in whose thesis study detailed muscle NIRS measurements were taken with different protocols and combined NIRS and EMG measurements were started in our lab.

Our cooperation with Assoc. Prof. Erdem Kaşıkçıoğlu from İstanbul University, Çapa Medical School, 'Spor Hekimliği Anabilim Dalı' has been fruitful. I was also involved in Ph.D. study of Dr. Mustafa Dinler, part of this cooperation. I'd like to thank to them, my experience with clinical studies increased with this collaboration.

I'd like to express my gratitude to Prof. Birol Çotuk from Marmara University,

Physical Education and Sports School. The muscle metabolism investigation part of the thesis could not be done so easily without his group's support. He has assisted me a lot both in providing environment for muscle measurements and with theoretical discussions on the topic. His students Bilal Biçer, Orkun Pelvan, Selda Uzun helped finding volunteers for the measurements, in conducting the muscle measurements, and in the theoretical discussions on the muscle metabolism. The muscle measurements were taken in Marmara University, 'Spor Bilimleri ve Sporcu Sağlığı Araştırma ve Uygulama Merkezi'. I'd like to thank again Prof. Birol Çotuk and Nuri Topsakal for providing us this facility. It has been really a pleasure for me to have an opportunity to work with this group.

I'd like to thank to my thesis committee. Three of them (including Assoc. Prof. Dr. Yasemin Kahya, Assoc. Prof. Dr. Can Yücesoy) were also in my thesis progress committee. I still remember the comment of Assoc. Prof. Dr. Can Yücesoy, who in the very early time of the study -in a progress report presentation- said something with meaning that 'Ph.D. is going from one point to another, determine that key topic, first do this, then you can do the other things you want afterwards'. Our thesis study at first included a lot of seemingly diverse topics but this comment helped me to choose a topic and concentrate on that first. I would like to thank also Prof. Dr. Bülent Sankur for accepting me into his research group which provided my Ph.D. scholarship by TÜBİTAK and monitoring my Ph.D. progress.

I have to acknowledge the effort of all my teachers in my education, including especially my high school physics teacher Mustafa Yalçın and my primary school teacher Fatma Nihal Selçuk.

The doctoral fellowship by TÜBİTAK (The Turkish Scientific & Technological Research Council) is gratefully acknowledged.

ABSTRACT

ACCURACY IMPROVEMENTS OF NIRS AND INVESTIGATION OF MUSCLE OXIDATIVE METABOLISM

In the first part of the thesis, the effect of fat layer on continuous wave near infrared spectroscopy (cw-NIRS) measurements were investigated in detail, both in terms of underestimation error (caused by homogeneous medium assumption) and crosstalk between chromophores because of homogeneous medium assumption and wavelength dependence of mean partial path length in the muscle layer. These errors have been investigated by Monte Carlo simulations with a skin-fat-muscle layered tissue model for a two wavelength system. The errors have been found to be higher for thicker fat thicknesses. A correction algorithm was proposed with the use of wavelength dependent partial path length in the muscle layer derived with Monte-Carlo simulations. Two detector cw-NIRS system was also analyzed and compared with 1-detector cw-NIRS system. The performance was promising but true assumption of initial optical coefficients of the layers poses a challenge for the performance.

Muscle metabolism, fatigue and endurance was examined with usage of three simultaneous measurement modalities: cw-NIRS, SEMG and force-time for isometric hand grip exercise. The study revealed some physiological processes related to fatigue. A highly valued and statistically significant correlations were found between sEMG and cw-NIRS derived parameters especially at 50% maximal voluntary contraction along with biometrics for endurance prediction. These information could be important in sports applications, ergonomics, physical medicine and rehabilitation to monitor the recovery with objective parameters.

Keywords: Near infrared spectroscopy, Continuous wave near infrared spectroscopy, Monte Carlo simulations, Light propagation in tissue, Muscle oxidative metabolism, Tissue oxygenation, Endurance, Fatigue, Surface electromyography.

ÖZET

YAKIN KIZIL ALTI SPEKTROSKOPİ YÖNTEMİNİN DOĞRULUĞUNUN İYİLEŞTİRİLMESİ VE KAS OKSİDATİF METABOLİZMASININ ARAŞTIRILMASI

Tezin ilk kısmında, yağ katmanının sürekli dalga yakın kızıl altı spektroskopinin (sd-YKAS) ölçümlerine olan etkisi detaylı olarak azımsama hatası (türdeş ortam varsayımından kaynaklanan) ve türdeş ortam varsayımı ile kas katmanındaki ortalama kısmi yolun dalga boyu bağımlılığından kaynaklanan çapraz girişim terimleriyle incelenmiştir. Bu hatalar, iki dalga boylu sistem için, deri-yağ-kas katmanlı doku modeliyle yapılan Monte Carlo benzetimleriyle incelenmiştir. Hatalar kalın yağ kalınlıkları için daha yüksek bulunmuştur. Monte Carlo benzetimleriyle çıkarılan dalga boyu bağımlı kısmi yol uzunluklarını kullanan bir düzeltme algoritması önerilmiştir. İki alıcılı sd-YKAS sistemi de analiz edilmiş ve 1-alıcılı sistem ile karşılaştırılmıştır. Performans umut verici olmasına rağmen, katmanların ilk optik katsayılarının doğru varsayımı bu performans için çözülmesi gereken bir sorundur.

Kas metabolizması, yorgunluk ve dayanıklılık, eş zamanlı sd-YKAS, yüzey elektromiyografi (yEMG) ve kuvvet-zaman ölçüm teknikleri kullanılarak yapılan ölçümlerle, izometrik el sıkma egzersizi için incelenmiştir. Çalışma yorgunlukla alakalı fizyolojik süreçleri açığa çıkarmıştır. YEMG ve sd-YKAS parametreleri arasında özellikle %50 maksimal istemli kasılmada önemli değerlerde ilintilerle beraber dayanıklılık tahmini için biyometrik parametreler bulunmuştur. Bu bilgiler spor uygulamaları, ergonomi, fizik tedavi ve rehabilitasyonda toparlanmanın nesnel parametrelerle takibinde de önemli olabilir.

Anahtar Sözcükler: Yakın kızıl altı spektroskopi, Sürekli dalga yakın kızıl altı spektroskopi, Monte Carlo Benzetimleri, Dokuda ışık dağılımı, Kas oksidatif metabolizması, Doku oksijenlenmesi, Dayanıklılık, Yorgunluk, Yüzey elektromyografi.

TABLE OF CONTENTS

LIST OF FIGURES

LIST OF TABLES

LIST OF SYMBOLS

a.u.	Arbitrary Unit
h_{s}	Skin Thickness
h_{f}	Fat Thickness
h_{m}	Muscle Thickness
kg.	Kilograms
m.	Meters
mm.	Millimeters
n.u.	No Unit
O_2	Oxygen
s.	Seconds
$\dot{V}O_2$	Oxygen Consumption
μ	Mean Value
σ	Standard Deviation

LIST OF ABBREVIATIONS

ATT	Adipose Tissue Thickness
BMI	Body Mass Index
cw-NIRS	Continuous Wave Near Infrared Spectroscopy
CC	Correlation Coefficient
CNS	Central Nervous System
COV	Coefficient Of Variation
DWS	Diffusing-Wave Spectroscopy
EMG	Electromyography
FD-NIRS	Frequency Domain Near Infrared Spectroscopy
FDS	Flexor Digitorum Superficialis
GUI	Graphical User Interface
Hb	Deoxy-hemoglobin
HbO_2	Oxy-hemoglobin
MCML	Monte Carlo Multi Layer
MDF	Median Frequency
MNF	Mean Frequency
MRI	Magnetic Resonance Imaging
MU	Motor Unit
NIRS	Near Infrared Spectroscopy
NS	Not Significant
SEMG	Surface Electromyography
SRS	Spatially Resolved Spectroscopy

1. INTRODUCTION

In this thesis, use of cw-NIRS for the study of muscle metabolism was aimed, especially for aerobic metabolism. Currently because of unavailable knowledge of partial path length of light in the muscle, cw-NIRS can not give concentrations' changes of Hb and HbO_2 in absolute units. Complicating the issue there is variability of fat layer thickness among subjects.

We first performed error and accuracy analysis of cw-NIRS because of the fat layer affect which causes underestimation of the real concentration changes occurring in the muscle layer, given in Chapter 3. Underestimation error is basically caused by homogeneous medium assumption in the calculations leading to the partial volume effect. Fat layer also leads to crosstalk affect which refers the estimation of concentration change of a chromophore for which there is no real change for itself but for the other chromophore. Homogeneous medium assumption and wavelength dependence of mean partial path length in the muscle layer causes the crosstalk. This analysis was performed using Monte Carlo simulation with skin-fat-muscle tissue model for various fat thicknesses up to 15 mm. Two wavelength cw-NIRS system was assumed where the choice of first wavelength is in 675 - 775 nm range and the second wavelength is in 825 - 900 nm range. Means of absolute underestimation errors and crosstalks over considered wavelength pairs have been found to be higher for thicker fat thicknesses. Estimation errors of concentration changes for Hb and HbO_2 are calculated to be close for ischemia type protocol where both Hb and HbO_2 are assumed to have equal magnitude but opposite concentration changes. The minimum estimation errors are found for the 700/825 nm and 725/825 nm pairs for this protocol.

Continuation of error analysis part because fat layer -in Chapter 4- was the development of correction algorithms which follows the results of this study, which was performed also and compared with two other correction curves from the literature on a well known data.

Two detector system is also studied for performance compared to one detector system, in Chapter 5. In this study, partial pathlength method with two detectors based on modified Beer-Lambert law extended for heterogeneous medium with homogeneous layered regions is investigated. Using Monte Carlo simulations, comparison between this technique and single homogeneous layer assumption is done. Optical coefficients of fat and muscle layers are chosen typical for muscle tissue measurements. In the simulations, change of absorption coefficient in muscle layer was made much bigger than in fat layer. It has been found that for 2-detector partial pathlength based method, fat and muscle layer absorption coefficient change estimates are better than the homogeneous medium based modified Beer-Lambert law estimates in all simulated cases. Partial pathlengths are used in 2-detector partial pathlength based method while mean pathlength is used for 1-detector based modified Beer-Lambert law estimates, hence initial operating point is assumed to be known. In practice, getting accurate initial (resting level) optical properties of the medium and obtaining accurate partial pathlengths poses a problem for the proposed technique. An error analysis is added to this study for which initial operating point for optical coefficients of the layers is taken erroneously.

In the thesis, hand grip exercise study was also performed to investigate muscle energetics and fatigue using SEMG, cw-NIRS and force-time measurements, in Chapter 6. The aim of this study was physiological interpretation of the EMG signal, $\triangle HbO_2$ and $\triangle Hb$ curves, hand grip force curve, with specific goal was to infer parameters (biometrics) related to endurance. The subjects were rowers and canoe athletes. This study was considered to be important in exploiting the use of cw-NIRS and searching endurance and fatigue background mechanisms. These type of researches are valuable also in ergonomics to make work places healthier for employees. There is also need for such biometrics in physical medicine and rehabilitation to monitor the recovery with objective parameters. This way, evaluation of physical training programs could be possible.

2. BACKGROUND

2.1 Basic Tissue Optics and Properties of Biological Tissues

Light propagation in the tissues can be used for both diagnostic and therapeutic applications. More properly, interaction of electromagnetic waves with tissues When the light fluence rate is small, it can be used for diagnostic purposes [1, 2]. In the diagnostic domain, light propagation in tissue are determined by the wavelength dependent absorption and scattering properties, anisotropy and refractive index. In the biological tissues, scattering effect is dominant. Another parameter is refractive index which is nearly 1.40 for most tissues [3]. Scattering, reflection and refraction are caused by the refractive index mismatches, i.e. at the boundaries of two tissues. Fresnel's laws are used to model interactions at these boundaries.

Diagnostic application use small fluence rates of light. When the fluence rate of light is high, destructive changes occur. They are categorized as photochemical, thermal, photoablative and electromechanical. Photochemical type change is basically caused by absorption of light by molecules in the tissue. This technique is used in photodynamic therapy by photosensitizer molecules injected to the cancereous lesions of interest excited by light of a specific wavelength. Thermal effect is because of deposition of thermal energy. Photoablative effect is caused by photo-dissociation of biopolymers and following fragment desorption. Very high fluence rates is responsible for dielectric breakdown of tissue and formation of plasma, called electromechanical effect. This plasma expands at a high rate leading to shock wave [1].

In diagnostic domain, absorption and scattering interactions are taken into consideration which are linear and time-invariant [1].

2.1.1 Absorption

Molecules in tissue absorb photon energy in a quantized fashion when the photon energy match needed transition energy. The process is not followed by emission of another photon. The excited photon returns to the ground state by conversion of absorbed energy into thermal energy through inter-molecular de-excitation processes (i.e. molecular vibrations and rotations) and extra-molecular de-excitation processes (molecular motion, collisions). The probability of a survival for photon length L (can be straight line or due to multiple scattering) is given by $e^{-\mu_a \cdot L}$, μ_a being absorption coefficient. The absorption coefficient μ_a ([length^{-1}], usually given in mm^{-1} or cm^{-1}) models probability per unit length of a photon being absorbed. It is equal to $\mu_a = \epsilon \cdot c$ where ϵ is specific absorption coefficient of the absorbing compound ([molar^{-1}·cm^{-1}] and c is the concentration of the compound ([molar]). The Beer-Lambert law gives the input and output light intensities of the geometry given in Figure 2.1 (A) as

$$A = \mathrm{OD} = \log_e (I_o/I) = \epsilon(\lambda)\, c\, r \tag{2.1}$$

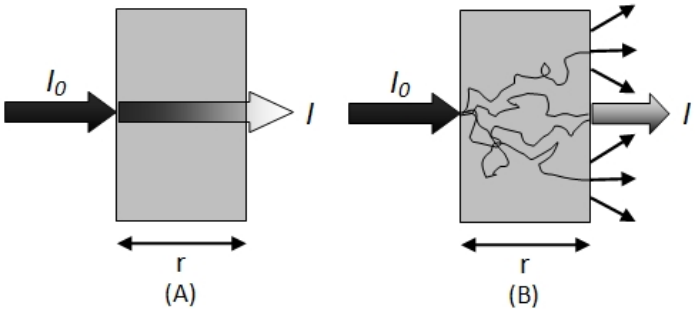

Figure 2.1 Light intensity drop through A) absorbing (and non-scattering) and B) scattering (and non-absorbing) mediums

which relates output intensity I for collimated input light intensity I_0. The medium is non-scattering and homogenous. The absorbance and light intensity drop is represented by A and it is used interchangeably with OD, called optical density. Another parameter is transmittance T, which is reciprocal of A. The specific absorption

coefficient $\epsilon(\lambda)$ is a function of wavelength λ. When logarithm base 10 is employed, the ϵ is called specific extinction coefficient (and μ_a is called extinction coefficient). Beer-lambert law is given as below for solutions containing multiple absorbing compounds;

$$\mathrm{OD} = \ln\left(I_o/I\right) = \epsilon_1(\lambda)\, c_1\, r + \epsilon_2(\lambda)\, c_2\, r + \ldots + \epsilon_n(\lambda)\, c_n\, r \tag{2.2}$$

Absorbed high energy (i.e. wavelengths less than 500 nm) leading to excitation of the atom or molecule can lead to following photochemical reaction [4].

2.1.2 Scattering

Scattering event by interaction with a scattering particle changes the initial direction of the photon by preserving the energy if it is elastic scattering, otherwise it is quasi-elastic or inelastic scattering. Inelastic scattering types are fluorescence and phosphorescence, Raman scattering, Brillouin scattering. In the near-infrared region for the tissues, elastic scattering is the type of scattering interest, i.e. modeled with Rayleigh and Mie scattering. Microscopic spatial fluctuations in refractive index causes scattering, i.e. cell membranes and organelles. Scattering is also wavelength dependent. Even if elastic scattering takes place, intensity loss happens since light direction is lost (i.e. light becomes incoherent). Scattering coefficient μ_s [mm^{-1}] can be described as cross sectional area of scattering event taking place per unit volume of a medium. It can also be defined as the probability per unit length travel of a photon being scattered. Transmission probability for length L of a photon is given by $e^{-\mu_s \cdot L}$. The light attenuation for homogeneous scattering and non-absorbing medium is formulated as;

$$\ln\left(I_o/I\right) = -\mu_s \cdot L \tag{2.3}$$

The mediums in real case are both absorbing and scattering. The final light intensity is formulated with modified Lambert-Beer Law for such cases;

$$\mathrm{OD} = \ln\left(I_o/I\right) = \epsilon(\lambda)\, c\, \mathrm{DPF}(\lambda)\, r + G(\lambda) \tag{2.4}$$

where again I is the intensity of the detected light, r is the minimal geometric distance between light source and detector, and DPF(λ) is the differential path length factor. DPF(λ) equals mean optical path length of the photons ($<L^{\lambda}>$) divided by r. $G(\lambda)$ factor is due to medium geometry and light scattering.

Some of the other fundamental parameters used to define optical properties of tissues are the reduced scattering (also called transport scatter) coefficient ($\mu_s' = \mu_s(1-g)$) and total attenuation coefficient ($\mu_t = \mu_a + \mu_s'$). Reduced scatter coefficient is the effective number of isotropic scatterers per unit length [5]. It combines the scattering coefficient and anisotropy factor g. This parameter is useful in modeling light transport through the tissue in the visible and near-infrared light for the scattering-dominated light transport which is called diffusion regime. It can be understood such that multiple anisotropic scatterings with mean free path length of $1/\mu_s$ is equivalent to isotropic single bigger step with a reduced free mean path length of $1/\mu_s'$ [6]. Anisotropy

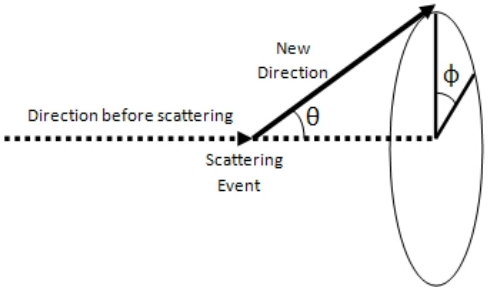

Figure 2.2 Deflection (θ) and azimuthal (ϕ) scattering angles

property (represented by g) is equal to average cosine of the scattering function and gives information about preserved forward direction for each scattering. The value of g is -1, 0 and 1 for complete reverse scattering, isotropic scattering and complete forward scattering. Angular dependence of scattering is modeled by scattering functions, the mostly used one is Henyey-Greinstein function. This function was originally used to model light scattering of interstellar dust but it also has a good performance for the purpose of scattering modeling in tissues. The scattering deflection angle θ (in 0 to π

range) is modeled with Henyey Greenstein function as follows;

$$p(\theta) = \frac{1}{4\pi}\frac{1-g^2}{(1+g^2-2g\cos(\theta))^{3/2}} \tag{2.5}$$

such that $\int_0^\pi p(\theta)2\pi\sin(\theta) = 1$, where g equals the expectation value of $\cos(\theta)$.

In Monte Carlo simulations, isotropic scattering is assumed using Principle of Similarity [7] which asserts that the photon distributions will be identical for two mediums with same light sources when absorption coefficients and reduced scattering coefficients are equal. Hence instead of anisotropic scattering with scattering coefficient μ_s and anisotropy factor g, isotropic scattering is assumed where the used reduced scattering coefficient is equal to $\mu_s(1-g)$.

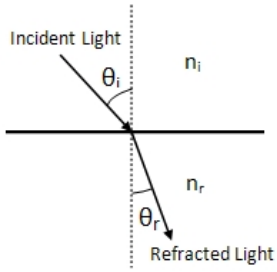

Figure 2.3 Refraction of light

Traveling light has different speeds and wavelengths in different mediums, but maintains its frequency. The speed of light in a medium divided by the speed of light in vacuum equals refractive index (n) for that medium. When light enters from one medium to another one, the angles of incidence (θ_i) and reflection (θ_r) are related to each other by refractive indices formulated by the Snell's law;

$$n_i\sin(\theta_i) = n_r\sin(\theta_r) \tag{2.6}$$

where n_i and n_r are angles of incident and refracted light, respectively measured with respect to normal. Direction change of the light from one medium to another one is because of the changing wavelength. The fractions of light transmitted to other

medium and reflected part are formulated by Fresnel equations.

The mostly used methods for modeling light transport in tissue are diffuse approximation and Monte Carlo, both of them ignores wave property of the light. Absorption and scattering events of photon are used instead. In diffuse approximation analytical approach to the so called radiative transfer equation (RTE) describing photon migration is used. Monte Carlo method is a stochastic approach to photon propagation. Diffuse approach requires $\mu_s' \gg \mu_a$. Monte Carlo technique can be used to model light propagation in regions where μ' is low (i.e. in cerebrospinal fluid) whereas diffusion approximation fails. Diffuse approximation is also not accurate at close neighborhood of light source (i.e. closer than ${\mu_s'}^{-1}$ or μ_t^{-1} depending on source) [8].

2.2 Light Absorbing Chromophores in Tissue

Tissues have typical absorption characteristics related to these compounds' optical properties depending also on their concentrations in the tissue of interest. Main light absorbers in the tissues are water, deoxy- and oxy-hemoglobin, deoxy- and oxy-myoglobin, and cytochrome-c-oxidase in the wavelength region of interest, near-infrared region. In the near-infrared range which is from 700 to 1000 nm, absorption of light is minimum which allows diagnostic and therapeutic applications possible which is drive for the calling of this band as 'diagnostic and therapeutic window'. Light absorption of water is especially low in the near infrared range which allows more penetration depth into the tissue. However absorption of light by water is still high because of its high concentration. Total absorption coefficient is summed by same proportion of water absorption. The water content is about 90% in neonatal brain and 80% of its weight for adult brain [9]. Outside these wavelength range, water and other chromophores (i.e. DNA, protein and other molecules in the ultraviolet range) cause very little penetration. In the tissues blood vessels are strong absorbers whereas their fraction is low in tissues. In the epidermis layer of skin, melanosomes are present with strong absorbance with low volume fraction (nearly 10% with 5% volume fraction of blood with 45% hematocrit). Strong absorbers with low volume fractions lead to moderate con-

tribution to average absorption coefficient which determines light transport although local absorption properties are governed by the strong absorber(s) [6].

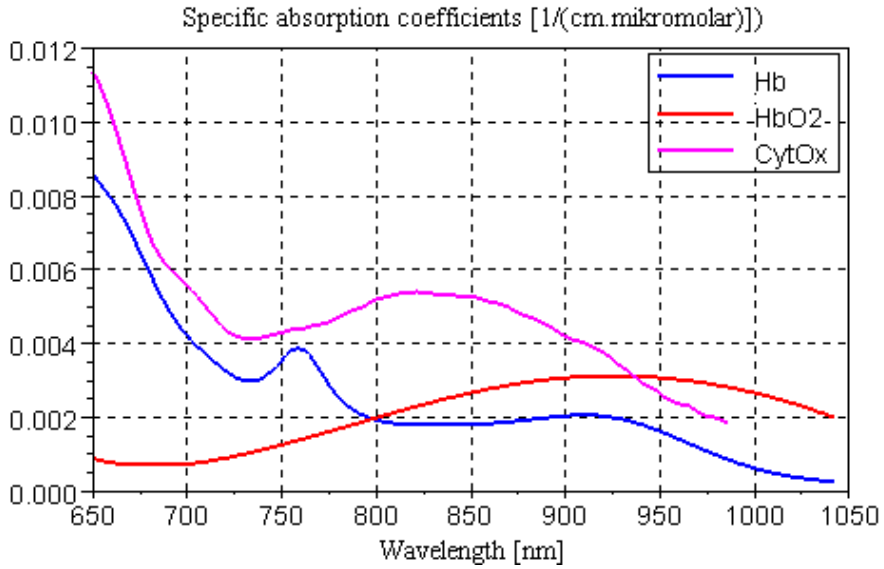

Figure 2.4 Specific absorption coefficients (for log base e) of Hb, HbO_2 and CytOx (difference between oxidised and reduced forms of cytochrome-c-oxidase)

Hb and HbO_2 have same absorption coefficients at the isobestic point near 800 nm. There is also myoglobin in muscle tissue which has indistinguishable absorption spectra to hemoglobin [10]. In the 'optic window' range, HbO_2 has higher absorption than Hb for wavelengths greater than the isobestic point.

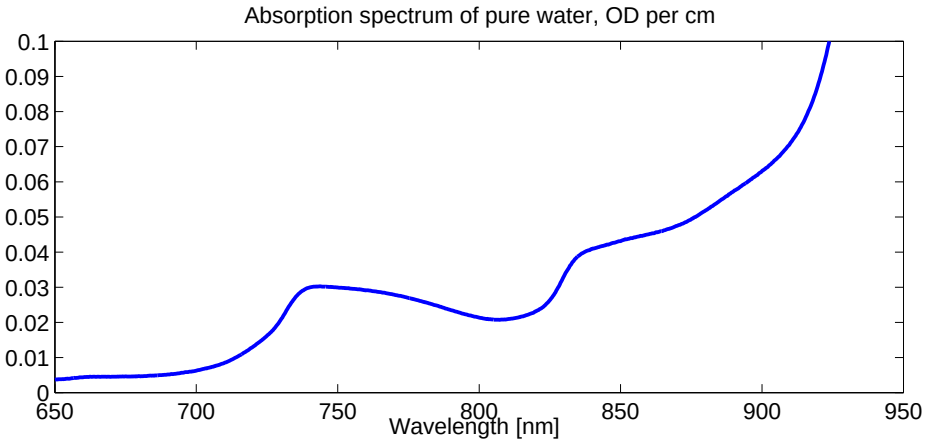

Figure 2.5 Absorption spectrum of pure water at 37° from Hollis [14]

Cytochrome-c-oxidase is of special interest respiratory chain enzyme. Oxidised form of cytochrome-c-oxidase has strong absorption band centered at 830 nm with 200 nm FWHM, which disappears when the enzyme is reduced [9]. The concentration

of cytochrome-c-oxidase is low compared to hemoglobin, at least one order of magnitude below [11]. Total concentration of cytochrome-c-oxidase does not change whereas oxidised/reduced forms change proportions.

Lipid absorption coefficient is comparable to water but it has a peak absorption at 930 nm and water absorption peak at 970 nm is missing [8]. Lipid content is 5% of the total wet weight of infant's brain, where the percentage goes up to 8% and 17% in the grey matter and white matter, respectively in the adulthood [9]. In the muscle tissue, thickness of superficial fat layer varies and can be thicker than 10 mm leading to much less probed volume of muscle layer. This special problem is investigated in detail in this thesis.

Oxidised-reduced forms of cytochrome-c-oxidase, oxygenated-deoxygenated forms of Hb/Mb concentrations change dynamically depending on tissue oxygen utilization and oxygen supply whereas concentrations of water, lipid, melanosome etc. don't change hence causing constant absorption [2]. However blood volume changes could cause some changes.

2.3 Near Infrared Spectroscopy

Biological tissues attenuate intensity of the transmitted light and also spread the transmitted light pulse. Hence it is stated that photon diffusion encodes the tissue characteristics upon the timing of the delayed pulse and upon the received intensity time profile [12]. There are different NIRS techniques: continuous wave near infrared spectroscopy (cw-NIRS), spatially resolved spectroscopy (SRS), time domain spectroscopy and frequency domain spectroscopy. cw-NIRS uses detected intensity changes of a constant light sources of different wavelengths (in the form of pulses generally) to calculate concentration changes of light absorbing chromophores. Spatially resolved spectroscopy is similar to cw-NIRS and finds concentration changes of the light absorbing chromophores but it has also ability to find oxygen saturation of hemoglobin. This technique uses multiple detectors and employs derivative of attenuation change

with respect to distance. Phase modulation (frequency domain, also called intensity modulated) and time resolved spectroscopy (time domain) techniques offer absolute concentrations of Hb/HbO_2 but require more complex systems, shown in Figure 2.6 from Delpy and Cope [13]. Received intensity pulse's time delay and phase shift are the parameters used in the frequency and time domain techniques, respectively besides detected light intensity. There are also broadband NIRS techniques. These methods use whole white light spectrum and second derivative of it [14] giving absolute concentrations.

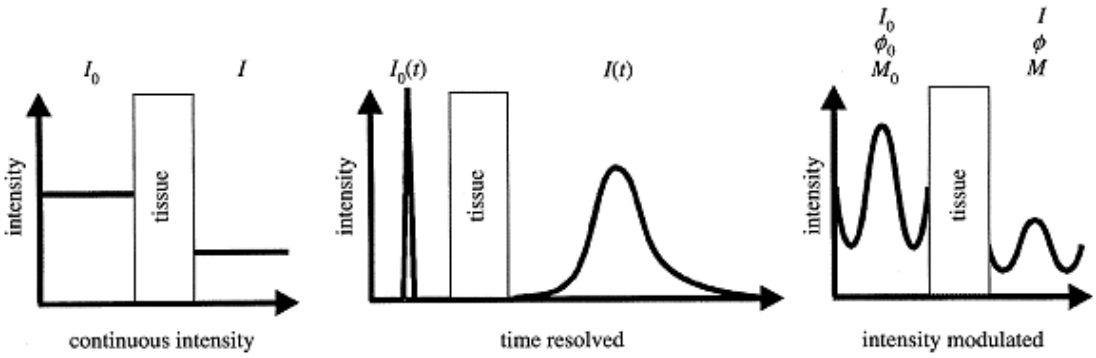

Figure 2.6 Some NIRS instrumentation types, from Delpy and Cope [19]

Diffusing-wave spectroscopy DWS (diffuse correlation spectroscopy) is a relatively new method, utilizing speckle (bright and dark spots) patterns in the tissue lasers from interference of light when light of large coherence laser goes through different pathways through the tissue. Change in this pattern with time with autocorrelation of the pattern yields information about blood flow [14].

2.3.1 Assessment of Heating Effects in NIRS

Heating effect of the light in the near infrared range is investigated by Ito *et al.* (2000) [15]. Low intensity continuous infrared laser light induced a maximal temperature change of approximately 0.1°C/mW on the skin surface and 0.04°C/mW at a depth of 1 mm in ex vivo tissue samples ($\lambda = 789$ nm). Similar temperature changes which ranged from 0.11 to 0.02°C/mW at depths of 0.5-1.5 mm, respectively, were found in the forearm measurements. To increase the normal skin temperature of 31°C

to the harmful 41°C (above which tissue damage occurs), 100 times greater than the maximum rise during 1 mW continuous wave radiation is required.

Compared to sunlight intensity in a sunny day (50 mW/cm^2), Bozkurt and Onaral (2000) [16] report that typical LED intensity (i.e. L730-805-850-40B32 Epitex Inc., λ = 730, 805 and 850 nm) is 25 - 50 mW/cm^2 and has typical power of 9 mW. They found less than 0.5°C temperature increase in the skin surface for typical case. They show that LED heating (in thermal junction) can cause a problem when the duty cycle increases especially in DC mode. The temperature increase can be up to 10°C/mW in the DC mode.

2.4 Continuous Wave Near Infrared Spectroscopy

Continuous Wave (cw) Near-Infrared Spectroscopy is a technique which estimates the concentration changes of optical chromophores in the tissues by measuring the detected the light intensity changes in a light detector nearby of a light source sending light in the near-infrared range through the tissue.

The cw-NIRS technique relies on the MBLL to convert detected light intensity changes into concentration changes of chromophores. For a single light absorber in a homogeneous medium, light attenuation is given by [9]

$$\mathrm{OD}^{\lambda} = \ln\left(I_o/I\right) = \epsilon^{\lambda}\, c\, \mathrm{DPF}^{\lambda}\, r + G^{\lambda} \tag{2.7}$$

where superscript λ indicates a particular wavelength, OD^{λ} is optical density, I_o is the intensity of the light sent into the tissue, I is the intensity of the detected light, ϵ^{λ} and c are the specific absorption coefficient (OD/cm/mM) and concentration (mM) of the chromophore in the medium, respectively; r (cm) is the minimal geometric distance between light source and detector, and DPF^{λ} is the differential path length factor. DPF^{λ} equals mean optical path length of the photons ($<L^{\lambda}>$) divided by r. G^{λ} factor is due to medium geometry and light scattering. The absorption coefficient of the

medium μ_a^λ is equal to $\epsilon^\lambda c$. The change in the logarithm of detected light intensity (ΔOD^λ) is proportional to concentration change of the absorber (Δc, assumed to be homogeneous and small), given by $\Delta\text{OD}^\lambda = \epsilon^\lambda \Delta c < L^\lambda >$, differential form of the MBLL. Here it is assumed that G^λ and $<L^\lambda>$ do not change during measurement. This formulation neglect the variation of $<L^\lambda>$ with μ_a^λ. In fact $<L^\lambda>$ should be replaced by its mean value computed over the range of absorption coefficient from 0 to μ_a^λ [17]. Nevertheless, MBLL formulation can still be used to determine concentration changes for small absorption changes for which $<L^\lambda>$ remains nearly constant [18, 19, 17]. Light scattering change is another issue [19].

For tissues where the main light absorbers are Hb and HbO_2,

$$\Delta\text{OD}^\lambda = \left(\epsilon^\lambda_{\text{Hb}} \Delta[\text{Hb}] + \epsilon^\lambda_{\text{HbO}_2} \Delta[\text{HbO}_2]\right) \text{DPF}^\lambda r \tag{2.8}$$

assuming a homogeneous tissue medium. For a two wavelength cw-NIRS system, concentration changes are estimated using MBLL as follows;

$$\Delta[\text{Hb}]_{\text{MBLL}} = \frac{\frac{\epsilon^{\lambda_2}_{\text{HbO}_2} \Delta\text{OD}^{\lambda_1}}{\text{DPF}^{\lambda_1}} - \frac{\epsilon^{\lambda_1}_{\text{HbO}_2} \Delta\text{OD}^{\lambda_2}}{\text{DPF}^{\lambda_2}}}{r\left(\epsilon^{\lambda_2}_{\text{HbO}_2}\epsilon^{\lambda_1}_{\text{Hb}} - \epsilon^{\lambda_1}_{\text{HbO}_2}\epsilon^{\lambda_2}_{\text{Hb}}\right)} \tag{2.9}$$

$$\Delta[\text{HbO}_2]_{\text{MBLL}} = \frac{\frac{\epsilon^{\lambda_1}_{\text{Hb}} \Delta\text{OD}^{\lambda_2}}{\text{DPF}^{\lambda_2}} - \frac{\epsilon^{\lambda_2}_{\text{Hb}} \Delta\text{OD}^{\lambda_1}}{\text{DPF}^{\lambda_1}}}{r\left(\epsilon^{\lambda_2}_{\text{HbO}_2}\epsilon^{\lambda_1}_{\text{Hb}} - \epsilon^{\lambda_1}_{\text{HbO}_2}\epsilon^{\lambda_2}_{\text{Hb}}\right)} \tag{2.10}$$

The MBLL subscript indicates that estimated concentration changes are found using homogeneous medium assumption based MBLL formulation. In general, a wavelength independent DPF is used in the MBLL calculations.

It should be noted hereby that for the considered muscle measurements, [Hb] ($[\text{HbO}_2]$) refers to combined concentrations of deoxyhemoglobin and deoxymyoglobin (oxyhemoglobin and oxymyoglobin) since hemoglobin and myoglobin have very similar absorption spectra [10].

2.4.1 Variation of DPF in NIRS Measurements

In the study of Duncan *et al.* (1995) [20], pathlength factor (DPF) variation during cuff occlusion was investigated and were found to be between 4-10%. This variation is comparable to DPF variability between individuals. Authors point out the need for continuous monitoring of optical pathlength.

2.4.2 Influence of Adipose Tissue Thickness (ATT) in NIRS

Muscle $\dot{V}O_2$ in the human flexor digitorum superficialis and FBF was found in 78 healthy subjects (skinfold thickness 1.4 to 8.9 mm) in the study of Van Beekvelt *et al.* (2001) [21] . ATT was found to have negative correlation with $\dot{V}O_2$ but it has a poor relationship with FBF. Gender difference was also attributed to ATT. Authors indicate that ATT has a substantial confounding influence on in vivo NIRS measurements.

Influence of fat layer on the near infrared measurements were investigated by using Monte Carlo simulations and experiments by Yang *et al.* (2005) [22] and Lin *et al.* (2000) [23]. It was found that if the fat thickness is less than 5 mm, subject-to-subject variation in the fat optical coefficients and thickness can be ignored [22]. It is suggested that influence of a fat layer can be eliminated by correcting the measurement sensitivity using the fat layer thickness [23].

2.5 Monte Carlo Simulations

In Monte Carlo simulation of photon propagation in biological tissues, a stochastic model is constructed in which rules of photon propagation are modeled in the form of probability distributions [24, 25, 26]. In the simulation, photons were launched with initial direction (i.e. along z-axis, perpendicular axis to tissue layers) from a point source. The events a photon encounters during propagation in the tissue are scattering and absorption. Scattering distances between two events and scattering lengths depend

on the tissue optical coefficients. Scattering angles are determined by anisotropy factor and scattering coefficient of the tissue layer. Photon movement related parameters are determined from appropriate probability density functions and photon loses weight in each scattering event. Photon movement is terminated when it escapes into air, leaves the tissue or loses its weight below a certain threshold (there is a 'roulette technique' also for the sake of conservation of energy, see Wang et al. [24]), or travels a distance longer than a predetermined length, depending also on the chosen Monte Carlo method. In this method, wave phenomena is neglected. Rationale behind this is that after multiple photon scattering phase and polarization become rapidly randomized.

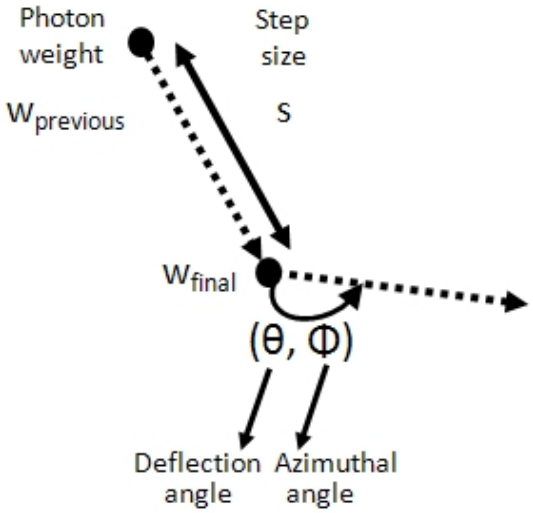

Figure 2.7 Basic events during photon movement

The photon propagation model in the Monte Carlo simulation can be summarized as;

- Launch photon into the tissue with initial weight and direction.
- Decrease the photon weight by specular reflection amount R_s, $w = w - R_s$
- In the tissue, if there is step size $\triangle s$ left from previous step move the photon by that length. Otherwise compute the new step size $\triangle s$ with the $s = -ln(\xi)/\mu_t$, ξ having uniform distribution over $(0, 1]$ and μ_t interaction coefficient equals sum of absorption coefficient μ_a and scattering coefficient μ_s. If boundary crossing happens, move the photon up to the boundary by $\triangle s_b$ and left the remaining

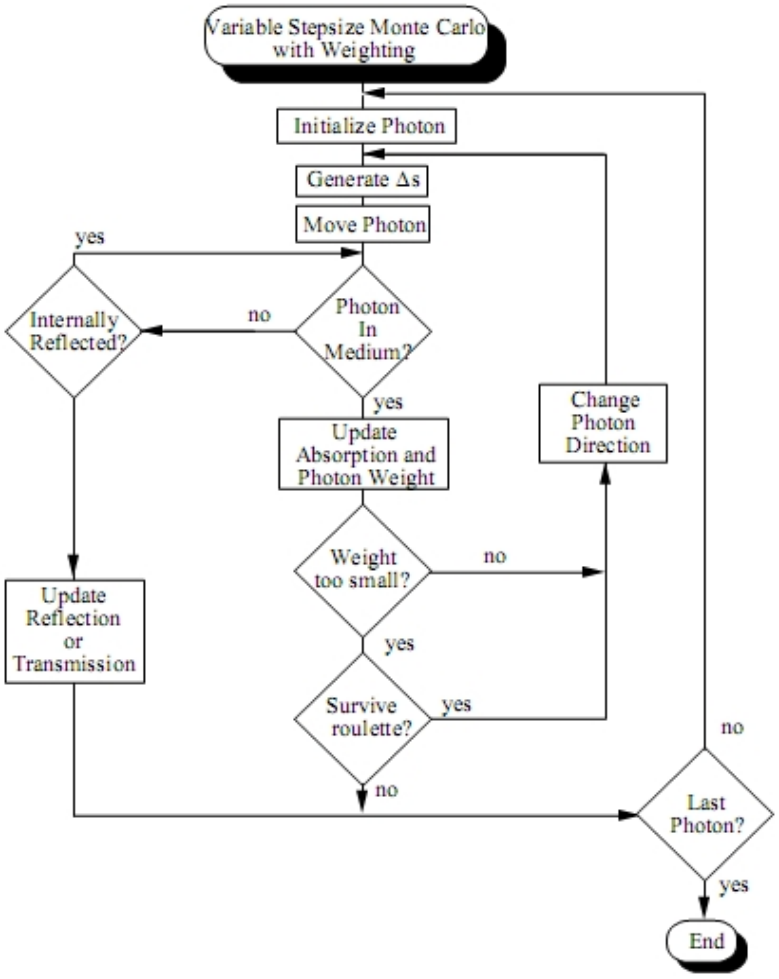

Figure 2.8 Flow chart of Monte Carlo simulations from Prahl et al. [31]

step size $\triangle s - \triangle s_b$ for next movement. For the movement, new coordinates (x, y, z) are found from directional cosines (μ_x, μ_y, μ_z) of the photon direction (scattering angle), i.e. $x = x + s\mu_x$.

- In the movement step, decrease the photon weight $w_{initial}$ by amount $\triangle w = w_{initial}\frac{\mu_a}{\mu_a+\mu_s}$, $w_{final} = w_{initial}\frac{\mu_s}{\mu_a+\mu_s}$
- In boundary crossing, internal reflection or transmission occurs and is handled using Fresnel's formulas and Snell's laws. Remaining step size after boundary crossing is updated by (from a layer with interaction coefficient of μ_{t1} to a layer with interaction coefficient μ_{t2}) $s = s\frac{\mu_{t1}}{\mu_{t2}}$
- When photon weight is below a threshold T_h, roulette law is applied. A uniform distributed random number between 0 and 1 is generated and if its greater than

$1/m$ (m is predetermined value), photon movement is terminated. Otherwise photon weight is multiplied by amount m. Since there is energy loss from terminated photons because of low weights, this step is done to conserve the energy.

- Next scatter movement angles are computed. Azimuthal angle is uniformly distributed over 0 and 2π, $\psi = 2\pi\xi$ where ξ having uniform distribution over 0 and 1. Deflection angle θ is in 0 to π range. $\cos(\theta)$ is modeled with Henyey Greenstein function.

$$p(\cos(\theta)) = \frac{1-g^2}{2(1+g^2-2g\cos(\theta))^{3/2}} \tag{2.11}$$

g is anisotropy factor and is between -1 and 1, and equals the expectation value of $\cos(\theta)$. Using a random sampling technique which is done by equating the cumulative distribution function of available computer generated random number ξ having uniform distribution over 0 and 1 with the cumulative distribution function of $p(cos(\theta))$, following sampling equation is obtained;

$$\cos(\theta) = \begin{cases} \frac{1}{2g}\left[1+g^2-\left(\frac{1-g^2}{1-g+2g\xi}\right)^2\right] & g \neq 0 \\ 2\xi - 1 & g = 0 \end{cases}$$

- When photon weight is below a threshold T_h, roulette law is applied. A uniform distributed random number between 0 and 1 is generated and if its greater than $1/m$ (m is predetermined value), photon movement is terminated. Otherwise photon weight is multiplied by amount m. Since there is energy loss from terminated photons because of low weights, this step is done to conserve the energy.

- Photon movement is also terminated when it leaves the tissue.

- When a photon is terminated, another photon is launched until desired photon number is achieved which is typically a large number to ensure obtaining the stable (accurate) statistic of a physical quantity of interest.

2.6 Usage of Near Infrared Spectroscopy in Muscle Studies and Sports Medicine

Since introduction of the possibility of using infrared light for monitoring tissue oxygenation changes, there has been a progress both in the technology of the NIRS and widespread investigation of usage of NIRS in muscle studies, mostly in the form of research work. Articles of Hamaoka et al. [27], Wolf et al. [14], Quaresima et al. [28], Boushel et al. [29], Boushel and Piantadosi [30], Neary [31], Ferrari et al. [32], are good summaries on the topic. Main advantage of this technique is that it allows non-invasive muscle metabolism investigation locally whereas invasive blood sampling and non-invasive expired/inhaled gas measurements give global muscle activity related information. MRI and MRS (i.e. ^{31}P,^{1}H, ^{23}Na-MRS) methods enables computation of crucial parameters such as inorganic phosphate (Pi), PCr breakdown rate and recovery (using ^{31}P-MRS), intracellular pH (from chemical shift of the Pi peak from the PCr peak), calculation of ADP and AMP concentrations from creatine kinase and adenylate kinase equilibria etc. However the method is complex and expensive. Besides experiment protocols that can be done inside the MRI scanner is limited. Investigated volume and voxel size in MRI/MRS depends on the system (i.e. magnet power (1.5 - 12 Tesla) and surface coil). In fact NIRS is also limited in giving local information because the probed muscle volume is confined close to the muscle surface, depending on the source-detector distance. Probed depth is roughly half of the source-detector distance for muscle measurements [33, 34, 35, 36], i.e. for the 2.5 cm optode distance, penetration depth would be 1.25 cm.

NIRS measurements give information about Hb/Mb concentration and oxygen saturation in weighted average of small blood vessels, capillaries with less than 1 mm diameter, and intercellular sites of oxygen uptake [37, 38, 39] since photons are unlikely to pass through large vessel because of high absorption [37]. The absorption through arterioles, capillaries and venules are low, in contrast. Hence changes in single muscle fibers can not be detected because of sensitivity of the technique [40].

Since differentiating between oxygen supply and demand is difficult, short duration arterial occlusion protocol is applied to derive oxygen consumption rate dependent changes with NIRS, i.e. to get decline rate of HbO_2 and increase in Hb rate. Since venous return is occluded, blood volume stays constant (assumed to) and oxygen uptake by the tissue converts HbO_2 pool to Hb. Employing NIRS, venous occlusion protocol is also applied to get blood flow proportional changes and muscle oxygen consumption using Hb and HbO_2 increase rates. HbO_2 increase is due to inflow of arterial blood and veneous occlusion, while Hb increase is due to mostly venous occlusion and oxygen consumption and to a lesser extent to Hb content in the arterial blood (i.e. 3%) [41]. Calculations with venous sampling need some additional measurements, such as blood sampling or arterial O_2 saturation from pulse oximeter [42]. The arterial or venous occlusion protocols require stopping the exercise hence are based on the assumption that measured values at the immediate end of exercise reflect the true values during the exercise [27].

With NIRS techniques of TRS or FDS, one may get absolute rates of oxygen consumption but with cw-NIRS percentage rates can be given or used DPF value dependent absolute units are given. Arbitrary units is also used cw-NIRS studies because of this problem. Because of the lack of true mean path length in the muscle layer in cw-NIRS technique, 5 to 6 minutes arterial occlusion at the start of an experiment was done in some cw-NIRS studies to get a scaling. Motivation behind this method physiological calibration with this method would have smaller interindividual variation compared to larger interindividual variation of DPF [43]. Although TRS, FDS Systems give values of the Hb/HbO_2 concentrations in absolute units, cw-NIRS requires relatively simple system both in terms of hardware and software. Also with cw-NIRS, signals proportional to blood flow rate with venous occlusion, oxygen consumption with arterial occlusion, concentration changes in HbO_2 and Hb can all be measured, quantification problem still remaining.

NIRS has been used in numerous basic physiological research and sports medicine investigations.

Studies of Chance *et al.* (1992) [44] and Hamaoka *et al.* (1992) [45] were the first studies on rowers. Ding *et al.* (2001) [38] also studied quadriceps muscle oxygen desaturation in athletes and control group after exhausting cycling exercise, which was found to be significantly reduced in athletes. Bhambhani *et al.* (1998) [46] studied arm cranking and leg cycling using NIRS for gender and exercise mode difference. Takaishi *et al.* (2002) [47] investigated the effects of cycling experience and pedal cadence on the NIRS parameters on non-cyclists, triathletes and cyclists. Bringard and Perrey (2004) [48] compared vastus lateralis deoxygenation kinetics measured by NIRS and pulmonary kinetics realized in an intermittent bilateral knee-extension exercise (3-s contraction 3-s relaxation) at 40% MVC for 10 min. It is found that deoxygenation kinetics at the onset of exercise followed an exponential time course at a significant faster rate than pulmonary O_2 uptake ($\dot{V}O_{2,\text{pulmonary}}$) which reflects a mismatch between local oxygen consumption and perfusion. In a study by Tachi *et al.* (2004) [49], subjects performed intermittent static dorsiflexion at 50% of MVC up to exhaustion with the right leg either up or down relative to heart. Same exercises were performed with/without occluding muscle blood flow. They found decreased endurance time, lower blood volume and lower oxygen saturation (NIRS), and faster MF decrease and integrated EMG increase related to fatigue in the leg up position.

Lower back muscles were investigated using NIRS, EMG and MMG by Yoshitake *et al.* (2001) [50].

van Beekvelt *et al.* [51] searched oxygen consumption of human flexor digitorum superficialis muscle for various workloads. Hicks *et al.* (1999) [52] investigated isometric load contraction in the forearm at 10% and 30% MVC under normoxia and hypoxia (14% inspired O_2) using NIRS (muscle oxygenation of center of the wrist flexors). Kime *et al.* (2003) [53] did a maximal voluntary isometric handgrip exercise for 10 sec. in 7 healthy male subjects. They tested their hypothesis that higher oxidative capacity muscle shows slower muscle reoxygenation after maximal short term isometric exercise because reoxy-rate may be influenced more by muscle $\dot{V}O_2$ than by O_2 supply. The authors found negative correlation ($r^2 = 0.727$) between Reoxy-rate calculated from NIRS and $\dot{V}O_2$ for finger flexor muscle but not with FBF. This finding supports their

hypothesis.

In a study by Praagman *et al.* (2003) [54], NIRS measurements were taken along with EMG measurements in the human forearm muscles biceps breve and brachioradiolis. Magnitude of the surface EMG signals and oxygen consumption rate using NIRS were found to be linear when a force (torque) is applied by the subject, except some moments.

It has been also used in investigations of peripheral vascular diseases in Kragelj *et al.* [55], McCully *et al.* [56]. Intermittent claudication (IC) in patients was investigated using NIRS by Komiyama *et al.* (2000) [57].

2.6.1 Variability and Reproducibility of NIRS Measurements

Van Beekvelt *et al.* (1992) [51] investigated $\dot{V}O_2$ in the human flexor digitorum superficialis muscle at rest and 10-90% MVC isometric exercise. Six subjects did the same experiment on three separate days. The within subject variability for each workload was found to be 15.7 to 25.6%. Hence they concluded that i)local oxygen consumption at rest as well as during exercise at a broad range of work intensities can be measured reliably by NIRS, applied to a uniform selected subject population ii)moreover NIRS is also robust enough to measure over separate days and at various workloads.

Kragelj *et al.* (2000) [58] looked at the variability of NIRS parameters such as $\dot{V}O_2$, recovery times, time to peak values, hyperemic response after release of the cuff expressed as a percentage (for Hb and HbO_2). NIRS instrument was positioned on the dorsal and lateral surfaces of the foot between the fourth and fifth digits, and measurements were taken in transmission mode. Five minutes of occlusion was applied. Same protocol was repeated on each subject four to six times. Mean values of coefficient of variability ranged from 6% to 30% (mean value 17%) indicating measurements were reproducible.

3. CROSSTALK AND ERROR ANALYSIS OF FAT LAYER ON CONTINUOUS WAVE NEAR-INFRARED SPECTROSCOPY MEASUREMENTS

Near infrared spectroscopy (NIRS) is increasingly used as an optical noninvasive method to monitor the changes in tissue oxygenation in brain [9, 59, 60], breast [61] and particularly in muscle tissues [62, 28, 27]. Continuous wave near-infrared spectroscopy (cw-NIRS) is based on steady-state technique where the changes in the detected light intensities at multiple wavelengths are converted to concentration changes of oxygenation sensitive chromophores. Typically cw-NIRS is used in muscle physiology studies for calculation of oxygen consumption and blood flow values. Spatially resolved spectroscopy [63] along with frequency and time domain techniques are other NIRS methods [64, 65] which have the capability of quantifying absolute concentrations.

NIRS techniques suffer inaccuracies for the heterogonous tissue structures when the homogeneous medium assumption is made for the sake of simplicity [66, 67]. In fact, there are solutions based on complex layered models [68, 69, 66, 67, 70, 71, 72, 73, 74, 75] for NIRS. The degree of inaccuracy because of the homogeneous medium assumption depends on the region of interest, geometry, optical coefficients of the structures in the tissue, source-detector distance and the choice of NIRS technique [36, 18, 76, 77, 23, 69, 66, 67, 78, 79]. Hence, the estimated parameter (i.e., absorption coefficient change) could be related to a layer's (or to combination of layers) property, or it may not be related to any property of any one of those layers at all [80, 69, 67].

Muscle tissue has superficial skin and fat layers. Fat layer has varying thicknesses between subjects and has lower absorption coefficient than the underlying muscle layer, masking the muscle's optical parameters hence making it difficult to determine optical coefficients and quantify concentration changes in the lower muscle layer. It has been shown experimentally that adipose tissue causes sensitivity and linearity problems [81, 82, 83, 84, 85, 86, 23, 87], underestimation of oxygen consumption [21] in muscle cw-

NIRS measurements in which modified Beer-Lambert law (MBLL) with homogeneous medium assumption is used. These problems are mainly related to the so called partial volume effect, which refers to the fact that hemodynamic changes occur in a volume smaller than that assumed by homogeneous medium assumption [88, 76, 77].

Crosstalk in NIRS measurements refers to the measurement of chromophore concentration change although no real change happens for that chromophore but for other chromophores' concentrations [89, 90, 91, 92, 76, 77]. This is caused again by the homogeneous medium assumption with the use of mean optical path length instead of wavelength dependent partial optical path length in the tissue layer of interest where the concentration changes occur (i.e. muscle or gray matter in the brain). There are detailed studies on the analysis of the crosstalk effect for brain measurements, while as we know, there is only one study of Iwasaka and Okada [93] on the crosstalk effect for muscle measurements, where the analysis was done for a fixed fat thickness of 4 mm.

The effect of adipose tissue layer on the cw-NIRS measurements with the homogeneous medium assumption using MBLL is investigated in our study by Monte Carlo simulations for a two wavelength system. Simulations were performed for a homogeneous layered skin-fat-muscle heterogeneous tissue model with varying fat thickness up to 15 mm. The wavelengths are in 675- to 775-nm range for the first wavelength and in 825- to 900-nm range for the second wavelength, and in total 24 wavelength pairs were used. For the considered wavelengths and fat thicknesses, mean partial path lengths in the three layers and detected light intensities were found. An error analysis for estimated concentration changes was analyzed by partitioning the error into an underestimation term for a real change in muscle layer and a crosstalk term, where the aims are the investigation of the fat layer thickness effect and a search for wavelength pairs that result in low errors. An error analysis for a particular measurement protocol of vascular occlusion is also discussed.

3.1 Theory

3.1.1 Homogeneous Medium Assumption

The cw-NIRS technique relies on the MBLL to convert detected light intensity changes into concentration changes of chromophores. For a single light absorber in a homogeneous medium, light attenuation is given by [9]

$$\mathrm{OD}^{\lambda} = \ln\left(I_o/I\right) = \epsilon^{\lambda}\, c\, \mathrm{DPF}^{\lambda}\, r + G^{\lambda} \tag{3.1}$$

where superscript λ indicates a particular wavelength, OD^{λ} is optical density, I_o is the intensity of the light sent into the tissue, I is the intensity of the detected light, ϵ^{λ} and c are the specific absorption coefficient (OD/cm/mM) and concentration (mM) of the chromophore in the medium, respectively; r (cm) is the minimal geometric distance between light source and detector, and DPF^{λ} is the differential path length factor. DPF^{λ} equals mean optical path length of the photons ($<L^{\lambda}>$) divided by r. G^{λ} factor is due to medium geometry and light scattering. The absorption coefficient of the medium μ_a^{λ} is equal to $\epsilon^{\lambda}c$. The change in the logarithm of detected light intensity ($\Delta\mathrm{OD}^{\lambda}$) is proportional to concentration change of the absorber (Δc, assumed to be homogeneous and small), given by $\Delta\mathrm{OD}^{\lambda} = \epsilon^{\lambda}\Delta c\, < L^{\lambda} >$, differential form of the MBLL. Here it is assumed that G^{λ} and $<L^{\lambda}>$ do not change during measurement. This formula and Eq. 3.1 of MBLL neglect the variation of $<L^{\lambda}>$ with μ_a^{λ}. In fact $<L^{\lambda}>$ should be replaced by its mean value computed over the range of absorption coefficient from 0 to μ_a^{λ} [17]. Nevertheless, MBLL formulation can still be used to determine concentration changes for small absorption changes for which $<L^{\lambda}>$ remains nearly constant [18, 19, 17]. Light scattering change is another issue [19].

For tissues where the main light absorbers are Hb and $\mathrm{HbO_2}$,

$$\Delta\mathrm{OD}^{\lambda} = \left(\epsilon_{\mathrm{Hb}}^{\lambda}\Delta[\mathrm{Hb}] + \epsilon_{\mathrm{HbO_2}}^{\lambda}\Delta[\mathrm{HbO_2}]\right)\mathrm{DPF}^{\lambda} r \tag{3.2}$$

assuming a homogeneous tissue medium. For a two wavelength cw-NIRS system, con-

centration changes are estimated using MBLL as follows;

$$\Delta[\mathrm{Hb}]_{\mathrm{MBLL}} = \frac{\frac{\epsilon^{\lambda_2}_{\mathrm{HbO_2}}\Delta\mathrm{OD}^{\lambda_1}}{\mathrm{DPF}^{\lambda_1}} - \frac{\epsilon^{\lambda_1}_{\mathrm{HbO_2}}\Delta\mathrm{OD}^{\lambda_2}}{\mathrm{DPF}^{\lambda_2}}}{r\left(\epsilon^{\lambda_2}_{\mathrm{HbO_2}}\epsilon^{\lambda_1}_{\mathrm{Hb}} - \epsilon^{\lambda_1}_{\mathrm{HbO_2}}\epsilon^{\lambda_2}_{\mathrm{Hb}}\right)} \tag{3.3}$$

$$\Delta[\mathrm{HbO_2}]_{\mathrm{MBLL}} = \frac{\frac{\epsilon^{\lambda_1}_{\mathrm{Hb}}\Delta\mathrm{OD}^{\lambda_2}}{\mathrm{DPF}^{\lambda_2}} - \frac{\epsilon^{\lambda_2}_{\mathrm{Hb}}\Delta\mathrm{OD}^{\lambda_1}}{\mathrm{DPF}^{\lambda_1}}}{r\left(\epsilon^{\lambda_2}_{\mathrm{HbO_2}}\epsilon^{\lambda_1}_{\mathrm{Hb}} - \epsilon^{\lambda_1}_{\mathrm{HbO_2}}\epsilon^{\lambda_2}_{\mathrm{Hb}}\right)} \tag{3.4}$$

The MBLL subscript indicates that estimated concentration changes are found using homogeneous medium assumption based MBLL formulation. In general, a wavelength independent DPF is used in the MBLL calculations.

It should be noted hereby that for the considered muscle measurements, [Hb] ([HbO_2]) refers to combined concentrations of deoxyhemoglobin and deoxymyoglobin (oxyhemoglobin and oxymyoglobin) since hemoglobin and myoglobin have very similar absorption spectra [10].

3.1.2 Underestimation Error and Crosstalk

For muscle cw-NIRS measurements, a more realistic tissue model should contain skin, fat, and muscle tissue layers. Measured optical density change can be written as [18];

$$\Delta\mathrm{OD}^{\lambda} = \Delta\mu_{a,\mathrm{s}} <L^{\lambda}_{\mathrm{s}}> + \Delta\mu_{\mathrm{a,f}} <L^{\lambda}_{\mathrm{f}}> + \Delta\mu_{\mathrm{a,m}} <L^{\lambda}_{\mathrm{m}}> \tag{3.5}$$

where $<L^{\lambda}_{\mathrm{s}}>$, $<L^{\lambda}_{\mathrm{f}}>$, and $<L^{\lambda}_{\mathrm{m}}>$ are the mean partial path lengths of the detected light and $\Delta\mu_{a,\mathrm{s}}$, $\Delta\mu_{a,\mathrm{f}}$, $\Delta\mu_{a,\mathrm{m}}$ are the homogeneous absorption changes in the skin, fat, and muscle layers, respectively. Assuming that the concentration changes mainly occur in the muscle layer, Eq. (3.5) becomes

$$\Delta\mathrm{OD}^{\lambda} \cong \left(\epsilon^{\lambda}_{\mathrm{Hb}}\Delta[\mathrm{Hb}]_{\mathrm{m}} + \epsilon^{\lambda}_{\mathrm{HbO_2}}\Delta[\mathrm{HbO_2}]_{\mathrm{m}}\right) <L^{\lambda}_{\mathrm{m}}> \tag{3.6}$$

where $\Delta[\mathrm{Hb}]_{\mathrm{m}}$ and $\Delta[\mathrm{HbO_2}]_{\mathrm{m}}$ are the real concentration changes in the muscle layer. Substituting Eq. (3.6) for measured optical density changes $\Delta\mathrm{OD}^{\lambda}$ in Eqs. (3.3) and

(3.4), the estimated concentration changes using MBLL can be written as [77];

$$\Delta[\mathrm{X}]_{\mathrm{MBLL}} = U_{\mathrm{X}}\Delta[\mathrm{X}]_{\mathrm{m}} + C_{\mathrm{X}}\Delta[\mathrm{O}]_{\mathrm{m}} \tag{3.7}$$

where X represents the chromophore being either Hb or HbO_2 and O represents the other chromophore, HbO_2 or Hb. $\Delta[\mathrm{X}]_{\mathrm{m}}$ and $\Delta[\mathrm{O}]_{\mathrm{m}}$ are the real concentration changes in the muscle layer, U_{X} corresponds to the underestimation of $\Delta[\mathrm{X}]_{\mathrm{m}}$, and C_{X} represents crosstalk from other chromophore $\Delta[\mathrm{O}]_{\mathrm{m}}$ to estimated $\Delta[\mathrm{X}]_{\mathrm{MBLL}}$, given by

$$U_{\mathrm{Hb}} = \frac{\epsilon_{\mathrm{Hb}}^{\lambda_1}\epsilon_{\mathrm{HbO_2}}^{\lambda_2} l^{\lambda_1} - \epsilon_{\mathrm{Hb}}^{\lambda_2}\epsilon_{\mathrm{HbO_2}}^{\lambda_1} l^{\lambda_2}}{\epsilon_{\mathrm{Hb}}^{\lambda_1}\epsilon_{\mathrm{HbO_2}}^{\lambda_2} - \epsilon_{\mathrm{Hb}}^{\lambda_2}\epsilon_{\mathrm{HbO_2}}^{\lambda_1}} \tag{3.8}$$

$$U_{\mathrm{HbO_2}} = \frac{\epsilon_{\mathrm{Hb}}^{\lambda_1}\epsilon_{\mathrm{HbO_2}}^{\lambda_2} l^{\lambda_2} - \epsilon_{\mathrm{Hb}}^{\lambda_2}\epsilon_{\mathrm{HbO_2}}^{\lambda_1} l^{\lambda_1}}{\epsilon_{\mathrm{Hb}}^{\lambda_1}\epsilon_{\mathrm{HbO_2}}^{\lambda_2} - \epsilon_{\mathrm{Hb}}^{\lambda_2}\epsilon_{\mathrm{HbO_2}}^{\lambda_1}} \tag{3.9}$$

$$C_{\mathrm{Hb}} = \frac{\epsilon_{\mathrm{HbO_2}}^{\lambda_1}\epsilon_{\mathrm{HbO_2}}^{\lambda_2}}{\epsilon_{\mathrm{Hb}}^{\lambda_1}\epsilon_{\mathrm{HbO_2}}^{\lambda_2} - \epsilon_{\mathrm{Hb}}^{\lambda_2}\epsilon_{\mathrm{HbO_2}}^{\lambda_1}}(l^{\lambda_1} - l^{\lambda_2}) \tag{3.10}$$

$$C_{\mathrm{HbO_2}} = \frac{\epsilon_{\mathrm{Hb}}^{\lambda_1}\epsilon_{\mathrm{Hb}}^{\lambda_2}}{\epsilon_{\mathrm{Hb}}^{\lambda_1}\epsilon_{\mathrm{HbO_2}}^{\lambda_2} - \epsilon_{\mathrm{Hb}}^{\lambda_2}\epsilon_{\mathrm{HbO_2}}^{\lambda_1}}(l^{\lambda_2} - l^{\lambda_1}) \tag{3.11}$$

where $l^{\lambda} = <L_{\mathrm{m}}^{\lambda}>/(\mathrm{DPF}^{\lambda} \times r)$. For a theoretical case of zero skin and fat thicknesses, mean optical path length $<L^{\lambda}>$ will be equal to $<L_{\mathrm{m}}^{\lambda}>$ which can be accurately measured by time or frequency domain NIRS systems. Hence this value can be used to find DPF^{λ} factor, i.e., $\mathrm{DPF}^{\lambda_1} = <L_{\mathrm{m}}^{\lambda_1}> /r$ and $\mathrm{DPF}^{\lambda_2} = <L_{\mathrm{m}}^{\lambda_2}> /r$. Underestimation terms U_{Hb} and $U_{\mathrm{HbO_2}}$ then have ideal values of 1 because both l^{λ_1} and l^{λ_2} are equal to one. Crosstalk terms C_{Hb} and $C_{\mathrm{HbO_2}}$ are null since l^{λ_1} and l^{λ_2} would be one, making their difference zero. However in practice, there are these superficial layers and measurement of $<L_{\mathrm{m}}^{\lambda}>$ alone is not possible. Magnitudes of crosstalk terms C_{Hb} and $C_{\mathrm{HbO_2}}$ are proportional to the difference of $l^{\lambda_1} - l^{\lambda_2}$. For the use of wavelength independent DPF, C_{Hb} and $C_{\mathrm{HbO_2}}$ are zero when $<L_{\mathrm{m}}^{\lambda_1}>=<L_{\mathrm{m}}^{\lambda_2}>$. Hence, one of the ways to minimize crosstalk is to utilize a wavelength pair for which partial optical path length in the layer of interest (i.e., gray matter in the brain) are equal [94]. In summary, the magnitude of underestimation and crosstalk terms depend on the wavelength dependence of specific absorption coefficients, choice of DPF^{λ} factors, which are used instead of unavailable $<L_{\mathrm{m}}^{\lambda}> /r$.

A common definition for crosstalk is the ratio of the estimated concentration change of the chromophore X for which no change happens to the estimated concentration change of the chromophore O for which real change is induced [91, 94], denoted as $C_{\mathrm{O}\to\mathrm{X}}$. According to this definition and previous formulation, $C_{\mathrm{HbO_2}\to\mathrm{Hb}}$ and $C_{\mathrm{Hb}\to\mathrm{HbO_2}}$ are

$$C_{\mathrm{HbO_2}\to\mathrm{Hb}}(\%) = 100 \times C_{\mathrm{Hb}}/U_{\mathrm{HbO_2}} \tag{3.12a}$$

$$C_{\mathrm{Hb}\to\mathrm{HbO_2}}(\%) = 100 \times C_{\mathrm{HbO_2}}/U_{\mathrm{Hb}} \tag{3.12b}$$

In this study, underestimation error (%) refers to (1-U_{X}) $\times$ 100 for the corresponding U_{X} factor. For the crosstalk, formulas given in Eqs. (3.12a) and (3.12b) are used. The estimation error for the concentration change of chromophore X in the muscle layer using MBLL is given by

$$E_{\mathrm{MBLL}} = 100 \times (\Delta[\mathrm{X}]_{\mathrm{MBLL}} - \Delta[\mathrm{X}]_{\mathrm{m}})/\Delta[\mathrm{X}]_{\mathrm{m}}\% \tag{3.13}$$

In this analysis, small concentration changes are assumed so that partial path length in the muscle layer remains constant such that calculated U_{X} and C_{X} terms along with underestimation and crosstalk errors are constant values for specific wavelength pair and fat thickness.

3.2 Methods

3.2.1 Tissue Model

For the simulations, three homogeneous layered skin-fat-muscle heterogeneous model is used. Skin thickness is taken to be 1.4 mm and muscle thickness is infinite. Reduced scattering coefficients of the three tissues and absorption coefficients of skin and adipose tissues are taken from Simpson et al. [95]. For the muscle tissue, the absorption coefficient is calculated with the equation

$$\mu_{a,\mathrm{m}}^{\lambda} = \mu_{a,\mathrm{w}}^{\lambda} V_{\mathrm{w}} + [t\mathrm{Hb}] \left[\epsilon_{\mathrm{HbO_2}}^{\lambda} StO_2 + \epsilon_{\mathrm{Hb}}^{\lambda}(1 - StO_2)\right] + \mu_{a,\mathrm{b}} \tag{3.14}$$

Table 3.1
Optical properties of the skin, fat and muscle tissue layers used in the simulations (for log base e).

	μ_a (cm^{-1})			μ_s' (cm^{-1})		
λ (nm)	Skin	Fat	Muscle	Skin	Fat	Muscle
675	0.232	0.097	0.321	24.81	12.24	8.53
700	0.191	0.089	0.254	23.17	12.03	8.08
725	0.172	0.089	0.243	21.99	11.87	7.89
750	0.165	0.092	0.288	20.97	11.67	7.69
760	0.159	0.093	0.306	20.53	11.61	7.50
775	0.146	0.087	0.291	19.91	11.50	7.21
800	0.127	0.083	0.284	19.07	11.36	6.99
825	0.121	0.085	0.309	18.24	11.12	6.78
850	0.122	0.086	0.343	17.57	11.09	6.60
875	0.122	0.091	0.368	16.98	10.97	6.43
900	0.134	0.125	0.393	16.30	10.88	6.32

where $\mu_{a,\mathrm{w}}^{\lambda}$ is the water absorption coefficient, V_{w} is water fraction of muscle tissue, [tHb] is total hemoglobin concentration, $\mathrm{StO_2}$ is oxygen saturation, and $\mu_{a,\mathrm{b}}$ is background absorption. In the calculation V_{w}, $\mathrm{StO_2}$ and [tHb] are taken as 70%, 70%, and 100 μM respectively, as typical values [96, 97]. The $\mu_{a,\mathrm{w}}^{\lambda}$ values are taken from the study of Hollis [8]. The background absorption coefficient of muscle tissue $\mu_{a,\mathrm{b}}$ is taken as 0.072 cm^{-1} so that the calculated $\mu_{a,\mathrm{m}}^{798\mathrm{nm}}$ equals the experimentally found in vitro value of Simpson et al. [95] since absorption at this isobestic point is unaffected by the oxygen saturation of the hemoglobin. Table 3.1 lists the absorption and reduced scattering coefficients of the three layers used in the simulations.

3.2.2 Monte Carlo Simulations

In Monte Carlo simulation of photon propagation in biological tissues, a stochastic model is constructed in which rules of photon propagation are modeled in the form

of probability distributions [24]. In the simulation, photons were launched with initial direction along z-axis (the axis perpendicular to tissue layers) from a point source. For a photon traveling in layer i which has absorption coefficient $\mu_{a,i}$, scattering coefficient $\mu_{s,i}$, and reduced scattering coefficient $\mu'_{s,i}$ (which is equal to $(1-g)\mu_{s,i}$, where g is the mean cosine of the single scattering phase function and is called anisotropy factor), successive scattering distances are selected using a random variable $l = -ln(R)/\mu'_{s,i}$, with R having uniform distribution over $(0, 1]$. The remaining scattering length Δl_i for photons crossing tissue boundary from medium i to medium j is recalculated by $\Delta l_j = \Delta l_i \mu'_{s,i}/\mu'_{s,j}$. Isotropic scattering is utilized using principle of similarity [7]. Scatter azimuthal angle was uniformly distributed over the interval $[0, 2\pi)$. Fresnel formulas are used for reflection or transmission at the boundaries [24].

Total distance traveled in layer i by a photon (L_i) was found by summing scattering lengths taken in this layer. Photon propagation was continued until it escapes the medium or travels 220 cm in length (10 ns). For those reaching the surface, exit (survival) weight (w) is calculated using Lambert-Beer law as $w = w_0 exp[-\sum_i (L_i \mu_{a,i})]$, with w_0 accounting for reflections and refractions at the boundaries encountered by the particular photon when there are refractive index mismatches [18]. Because of the symmetry of the medium considered, photons reaching a ring (thickness is dr, distance from center of ring to the light source is r) were taken as the photons reaching the detector. The mean partial path length in medium i ($<L_i>$) for the detected photons was found using the formula $<L_i> = \sum_{j=1}^{N} L_{i,j} w_j / (\sum_{j=1}^{N} w_j)$, where $L_{i,j}$ is the total path length taken in medium i by detected photon j with weight w_j, and N is total number of detected photons. Refractive indices of air and tissue layers were taken to be 1 and 1.4, respectively [3]. Each simulation was performed using 5×10^7 photons and the dr thickness is taken to be 0.5 cm.

3.3 Results

3.3.1 Path Lengths and Detected Light Intensity

We performed Monte Carlo simulations to calculate the mean partial path lengths for the 11 distinct wavelengths given in Table 3.1. $<L^{\lambda}_{\mathrm{i},r,h_\mathrm{f}}>$ represents the mean partial path length in layer i (s, f, or m for skin, fat, and muscle, respectively as used in section 3.1.2), for a source-detector distance r (cm), at fat thickness h_f (mm) and wavelength λ. $<L_{\mathrm{i},r,h_\mathrm{f}}>$ denotes the mean $\pm$ standard deviation of the mean partial path length in layer i computed over all wavelengths.

The term $<L^{\lambda}_{\mathrm{m}}>$ is the most important variable affecting the underestimation error and crosstalk, shown in Figure 3.1. The value of $<L^{\lambda}_{\mathrm{m},3.0,h_\mathrm{f}}>$ decreased linearly with a higher slope for $0 \leq h_\mathrm{f} \leq 7$ mm, while the slope decreased for $h_\mathrm{f} > 7$ mm. The value of $<L_{\mathrm{m},3.0,0}>$ is 11.15$\pm$1.20 cm and that of $<L_{\mathrm{m},3.0,7}>$ is 2.35$\pm$0.43 cm. Above 10 mm of fat thickness, $<L^{\lambda}_{\mathrm{m},3.0,h_\mathrm{f}}>$ decreased much more slowly but eventually approached null, where $<L_{\mathrm{m},3.0,15}> = 0.20 \pm 0.04$ cm. It was possible to infer a considerable wavelength dependent variability in $<L^{\lambda}_{\mathrm{m},3.0,h_\mathrm{f}}>$. The value of $<L^{\lambda}_{\mathrm{m},3.0,h_\mathrm{f}}>$ was found to increase from 675 to 725 nm, while it had a decreasing trend from the 725- to 900-nm range. This finding can be explained by the wavelength dependence of the optical properties of muscle and fat tissues given in Table 3.1. The coefficient of variation (CV = standard deviation/mean) of $<L^{\lambda}_{\mathrm{m},3.0,h_\mathrm{f}}>$ values over 11 wavelengths increased from 11% at $h_\mathrm{f} = 0$ mm to 23% at $h_\mathrm{f} = 15$ mm.

The value of $<L^{\lambda}_{\mathrm{s},3.0,h_\mathrm{f}}>$ was found to be the least varying mean partial path length with respect to h_f variation with values ranging from 1.78 to 2.39 cm having a maximum at around $h_\mathrm{f} = 6$ to 7 mm for all considered wavelengths. In contrast to $<L^{\lambda}_{\mathrm{m},r,h_\mathrm{f}}>$, $<L^{\lambda}_{\mathrm{f},r,h_\mathrm{f}}>$ and mean path length increased with increasing h_f, as expected. The value of $<L_{\mathrm{f},3.0,h_\mathrm{f}}>$ ranged from 1.84$\pm$0.13 cm at 1 mm fat thickness to 21.77$\pm$1.24 cm at $h_\mathrm{f} = 15$ mm, while the mean path length ranged from 13.03 ± 1.26 cm at $h_\mathrm{f} = 0$ mm to 24.17 ± 1.30 cm at $h_\mathrm{f} = 15$ mm. The mean path length had a decreasing trend with local peaks at either 700 or 725 nm and either 775 or 800 nm.

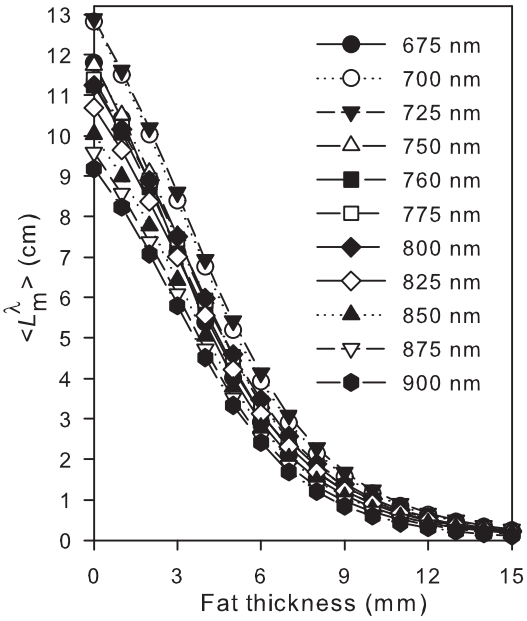

Figure 3.1 Mean partial path length in the muscle layer for various wavelengths in the range 675 - 900 nm and fat thicknesses up to 15 mm estimated by Monte Carlo simulations ($r = 3.0$ cm).

An increase in the fat layer thickness caused an increase in the detected light intensity. These increases in the detected light intensities for the 11 wavelengths expressed as mean±standard deviation were 74±28, 272±97, and 537±184% at $h_{\mathrm{f}} = 4$, 8, and 15 mm, respectively, with respect to detected intensities at $h_{\mathrm{f}} = 0$ mm ($r = 3.0$ cm).

With increase in source-detector distance, $<L_{\mathrm{m}}^{\lambda}>$ and mean path length increased while detected light intensity decreased. In particular, $<L_{\mathrm{m},4.0,0}>= 15.31 \pm 1.65$ cm, and $<L_{\mathrm{m},4.0,7}>= 4.31 \pm 0.75$ cm.

3.3.2 Underestimation Error

Underestimation errors were calculated for a two wavelength cw-NIRS system under varying fat thicknesses. The two wavelengths were chosen to fall before and after the isobestic point at around 800 nm. Hence, there were 24 wavelength pairs λ_1/λ_2, where λ_1 is between 675 and 775 nm and λ_2 is between 825 and 900 nm. DPF was taken to be wavelength independent with a value of 4.37 found for $\mathrm{h}_f = 0$ and $\lambda = 800$ nm. Underestimation error the for pair λ_1/λ_2 is denoted by $E_{\mathrm{X},r,h_{\mathrm{f}}}^{\lambda_1,\lambda_2}$ where the

first subscript refers to the chromophore, the second and (if present) third subscripts refer to source-detector distance (cm), and the h_{f} value (mm), respectively. For the all considered λ_1/λ_2 pairs, $E_{\mathrm{X},r,h_{\mathrm{f}}}$ shows mean $\pm$ standard deviation of the absolute values of the underestimation errors $E^{\lambda_1,\lambda_2}_{\mathrm{X},r,h_{\mathrm{f}}}$.

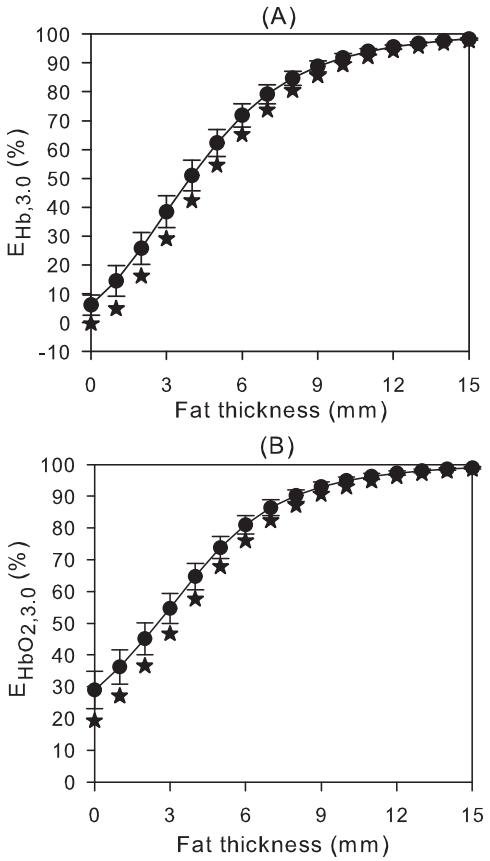

Figure 3.2 (A) $E_{\mathrm{Hb},3.0}$ (%) (B) $E_{\mathrm{HbO_2},3.0}$ (%) which are mean$\pm$standard deviation of absolute respective underestimation errors computed over all considered λ_1/λ_2 pairs for fat thicknesses up to 15 mm. Minimum individual errors for $E^{\lambda_1,\lambda_2}_{\mathrm{Hb},3.0,h_{\mathrm{f}}}$ and $E^{\lambda_1,\lambda_2}_{\mathrm{HbO_2},3.0,h_{\mathrm{f}}}$ are shown as stars.

Figure 3.2 A and B show $E_{\mathrm{Hb},3.0,h_{\mathrm{f}}}$ and $E_{\mathrm{HbO_2},3.0,h_{\mathrm{f}}}$ along with minimum errors for $E^{\lambda_1,\lambda_2}_{\mathrm{Hb},3.0,h_{\mathrm{f}}}$ and $E^{\lambda_1,\lambda_2}_{\mathrm{HbO_2},r,h_{\mathrm{f}}}$. The 725/900-nm pair gives the minimum values for $E^{\lambda_1,\lambda_2}_{\mathrm{Hb},3.0,h_{\mathrm{f}}}$ except at $h_{\mathrm{f}} = 0$ mm, for which the 700/825-nm gives the minimum error. The 675/825-nm pair gives the minimum error for $E^{\lambda_1,\lambda_2}_{\mathrm{HbO_2},r,h_{\mathrm{f}}}$ from $h_{\mathrm{f}} = 0$ mm up to and including 10 mm, and at higher h_{f} values the 760/825-nm pair is the minimum error producing pair. Both the errors $E_{\mathrm{Hb},3.0,h_{\mathrm{f}}}$ and $E_{\mathrm{HbO_2},3.0,h_{\mathrm{f}}}$ exhibited a steep increase in the fat thickness range $<$5 mm and a decreasing slope beyond this value. Interestingly, $E_{\mathrm{Hb},3.0,h_{\mathrm{f}}}$ began at a lower value compared to $E_{\mathrm{HbO_2},3.0,h_{\mathrm{f}}}$ but had a larger slope in this range. As expected, $E_{\mathrm{Hb},3.0,h_{\mathrm{f}}}$ and $E_{\mathrm{HbO_2},3.0,h_{\mathrm{f}}}$ approached complete underestimation error (100%)

Table 3.2
Underestimation errors $E^{\lambda_1,\lambda_2}_{\mathrm{Hb},3.0,2}$ (%) and $E^{\lambda_1,\lambda_2}_{\mathrm{HbO_2},3.0,2}$ (%) for the considered λ_1/λ_2 pairs.

	λ_1 (nm)	675	700	725	750	760	775
	λ_2 (nm)						
$E^{\lambda_1,\lambda_2}_{\mathrm{Hb},3.0,2}$ (%)	825	32.4	21.6	18.0	28.7	32.4	29.2
	850	32.0	21.2	17.4	27.6	31.1	26.9
	875	31.8	20.9	16.8	26.8	30.2	25.4
	900	31.6	20.5	16.1	26.0	29.4	23.9
$E^{\lambda_1,\lambda_2}_{\mathrm{HbO_2},3.0,2}$ (%)	825	36.5	38.1	40.4	38.2	37.2	39.2
	850	41.4	43.0	45.6	43.9	43.1	46.0
	875	44.7	46.4	49.2	47.7	47.0	50.5
	900	47.1	49.0	52.1	50.8	50.1	54.3

at $h_\mathrm{f} = 15$ mm. For the no fat thickness case, $E_{\mathrm{Hb},3.0,0}$ was 6.1±3.5% and $E_{\mathrm{HbO_2},3.0,0}$ was 28.9±5.8%. The slopes of the least squares fits to the absolute values of underestimation errors in $h_\mathrm{f} = 0$ to 5 mm range were 11.5%/mm ($R^2 = 0.94$) for $|E^{\lambda_1,\lambda_2}_{\mathrm{Hb},3.0}|$ and 9.1%/mm ($R^2 = 0.91$) for $|E^{\lambda_1,\lambda_2}_{\mathrm{HbO_2},3.0}|$.

There is wavelength pair dependency in the underestimation errors. The value of $E^{\lambda_1,\lambda_2}_{\mathrm{Hb},3.0}$ decreased in magnitude for an increase in λ_2 while that of $E^{\lambda_1,\lambda_2}_{\mathrm{HbO_2},3.0}$ increased, for fixed λ_1 at a given h_f. This change of variation over λ_2 was higher for $E^{\lambda_1,\lambda_2}_{\mathrm{HbO_2},3.0}$. The variation of λ_1 -for fixed λ_2 at a given h_f- led to a high range of change for $E^{\lambda_1,\lambda_2}_{\mathrm{Hb},3.0}$, where 700 and 725 nm lead to lower errors. Underestimation errors for $h_\mathrm{f} =$ 2 mm are given in Table 3.2 to show wavelength pair effect. The wavelength pair dependency of underestimation errors decreased with h_f increase. CV values of absolute underestimation errors were 56.5% (20.0%) at $h_\mathrm{f} = 0$ mm and 0.3% (0.4%) at $h_\mathrm{f} = 15$ mm for $|E^{\lambda_1,\lambda_2}_{\mathrm{Hb},3.0}|$ ($|E^{\lambda_1,\lambda_2}_{\mathrm{HbO_2},3.0}|$) over the considered λ_1/λ_2 pairs.

For longer source-detector distance of 4.0 cm, errors are lower. Here, $E_{\mathrm{Hb},4.0,0}$ and $E_{\mathrm{HbO_2},4.0,0}$ were 5.7±2.3 and 26.7±5.7%, respectively. The slopes of the least squares fits in 0 to 5-mm fat thickness range are 9.9%/mm ($R^2 = 0.89$) for $|E^{\lambda_1,\lambda_2}_{\mathrm{Hb},4.0}|$

and 8.0%/mm ($R^2 = 0.88$) for $|E^{\lambda_1,\lambda_2}_{\mathrm{HbO_2},4.0}|$. Again above h_f=10 mm, $E_{\mathrm{Hb},4.0}$ ($E_{\mathrm{HbO_2},4.0}$) became very high, with values above 87.3±2.3% (92.1±1.5%).

3.3.3 Crosstalk Analysis

Crosstalks was calculated using Eqs. (3.12a) and (3.12b) for the two wavelength system represented by $C^{\lambda_1,\lambda_2}_{\mathrm{O}\to\mathrm{X},r,(h_\mathrm{f})}$, where the superscripts refer to particular wavelength pair and first, second, and (if present) third subscripts represent crosstalk type, source-detector distance (cm) and h_f value (mm), respectively. Crosstalks was computed for the same λ_1/λ_2 pairs in underestimation error computations. DPF was assumed to be taken as wavelength independent, for which case crosstalks defined by Eq. (3.12) result in DPF-independence. $C_{\mathrm{O}\to\mathrm{X},r,(h_\mathrm{f})}$ represents mean±standard deviation of absolute values of crosstalks $|C^{\lambda_1,\lambda_2}_{\mathrm{O}\to\mathrm{X},r,(h_\mathrm{f})}|$ for the all λ_1/λ_2 pairs.

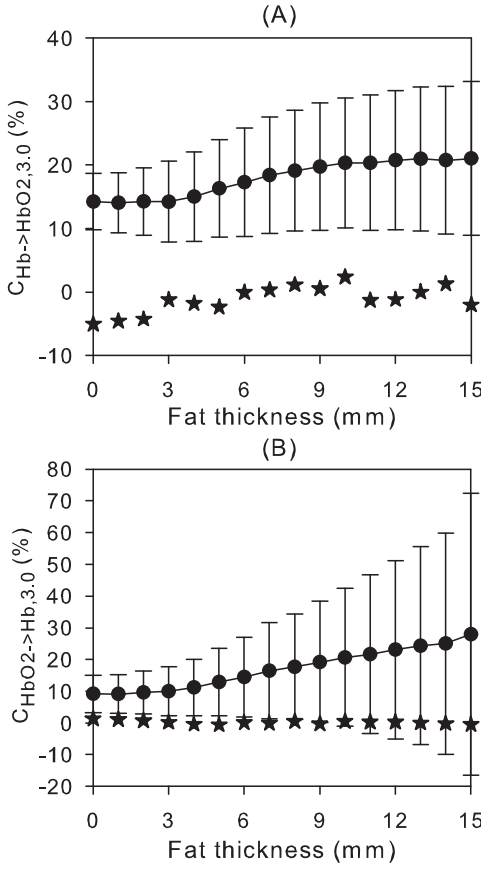

Figure 3.3 (A) $C_{\mathrm{Hb}\to\mathrm{HbO_2},3.0,h_\mathrm{f}}$ (%) and (B) $C_{\mathrm{HbO_2}\to\mathrm{Hb},3.0,h_\mathrm{f}}$ (%) which are mean±standard deviation of absolute respective crosstalks computed over all considered λ_1/λ_2 pairs for fat thicknesses up to 15 mm. Stars show the minimum individual errors for $C^{\lambda_1,\lambda_2}_{\mathrm{Hb}\to\mathrm{HbO_2},3.0,h_\mathrm{f}}$ and $C^{\lambda_1,\lambda_2}_{\mathrm{HbO_2}\to\mathrm{Hb},3.0,h_\mathrm{f}}$

In general $C^{\lambda_1,\lambda_2}_{\mathrm{HbO_2}\rightarrow\mathrm{Hb},3.0}$ had positive values while $C^{\lambda_1,\lambda_2}_{\mathrm{Hb}\rightarrow\mathrm{HbO_2},3.0}$ had negative values. The minimum error producing pairs for $C^{\lambda_1,\lambda_2}_{\mathrm{HbO_2}\rightarrow\mathrm{Hb},3.0}$ were the 675/825-nm pair at $h_\mathrm{f} = 0$ mm up to and including 5 mm, the 760/825-nm at $h_\mathrm{f} = 6, 7$, and 9 mm; and the 675/850-nm pair at other h_f values. Also $C^{\lambda_1,\lambda_2}_{\mathrm{HbO_2}\rightarrow\mathrm{Hb},3.0}$ had the minimum errors for the 760/825-nm pair at $h_\mathrm{f} = 0, 1, 2, 4, 5, 6, 7, 8, 9$, and 10 mm, for the 675/825-nm pair at $h_\mathrm{f} = 3$ mm; for the 675/850-nm pair at $h_\mathrm{f} = 11, 12, 13$, and 14 mm; and for the 750/825-nm at $h_\mathrm{f} = 15$ mm. The values of $C_{\mathrm{HbO_2}\rightarrow\mathrm{Hb},3.0}$ (about 9.5%) and $C_{\mathrm{Hb}\rightarrow\mathrm{HbO_2},3.0}$ (about 14.2%) were nearly constant in the $h_\mathrm{f} = 0$ to 3-mm range, as shown in Figure 3.3. While in the $h_\mathrm{f} = 3-$ to 14-mm range $C_{\mathrm{HbO_2}\rightarrow\mathrm{Hb},3.0}$ increased up to 25.0±34.9%, $C_{\mathrm{Hb}\rightarrow\mathrm{HbO_2},3.0}$ showed an increasing trend in the $h_\mathrm{f} = 3-$ to 10-mm range, with $C_{\mathrm{Hb}\rightarrow\mathrm{HbO_2},3.0,10} = 20.3 \pm 10.2\%$. The slopes of the least squares fits in these respective h_f ranges to the absolute crosstalk values were 1.4%/mm (R^2=0.1) for $|C^{\lambda_1,\lambda_2}_{\mathrm{HbO_2}\rightarrow\mathrm{Hb},3.0}|$ and 0.9%/mm (R^2=0.1) for $|C^{\lambda_1,\lambda_2}_{\mathrm{Hb}\rightarrow\mathrm{HbO_2},3.0}|$.

In Table 3.3, crosstalk values are given for $h_\mathrm{f} = 0, 5, 10$, and 15-mm values for all wavelength pairs. Similar to the increase seen in the mean values, the standard deviations of absolute crosstalks over considered wavelength pairs showed dramatic increases as the fat thickened. The $C^{\lambda_1,\lambda_2}_{\mathrm{HbO_2}\rightarrow\mathrm{Hb},3.0}$ had The CV values of 64.9, 82.3, and 159.2% at h_f values of 0, 5, and 15 mm, respectively. The $C^{\lambda_1,\lambda_2}_{\mathrm{Hb}\rightarrow\mathrm{HbO_2},3.0}$ had lower CV values of 31.0, 47.0, and 57.6% at $h_\mathrm{f} = 0$, 5, and 15 mm. However, $C^{\lambda_1,\lambda_2}_{\mathrm{Hb}\rightarrow\mathrm{HbO_2},3.0}$ had higher magnitudes in general. Examining the results from Table 3.3, we can observe that both absolute values of crosstalks are less than 11% for pairs 675/825, 675/850, 675/875, 750/825, 760/825, 760/850, and 775/825 nm for $h_\mathrm{f} < 10$ mm. In addition to these pairs, $C^{\lambda_1,\lambda_2}_{\mathrm{HbO_2}\rightarrow\mathrm{Hb},3.0,h_\mathrm{f}}$ had low crosstalk values also for pairs 675/900 and 700/825 nm. Higher crosstalk magnitudes were computed for the choice of higher a λ_2 for a fixed λ_1 at a given h_f.

Crosstalk values for a source-detector distance of $r = 4.0$ cm results in slightly smaller values. At $h_\mathrm{f} = 0$, 5, 10, and 15 mm, $C_{\mathrm{HbO_2}\rightarrow\mathrm{Hb},4.0,h_\mathrm{f}}$ was 9.0±5.6, 11.5±9.2, 19.3±17.6, and 22.6±27.4%, and $C_{\mathrm{Hb}\rightarrow\mathrm{HbO_2},4.0,h_\mathrm{f}}$ was 14.1±4.4, 15.3±7.5, 20.1±10.0, and 20.6±11.0%, respectively.

Table 3.3
Crosstalk values $C^{\lambda_1,\lambda_2}_{\mathrm{Hb}\to\mathrm{HbO_2},3.0,h_\mathrm{f}}$ (%) and $C^{\lambda_1,\lambda_2}_{\mathrm{HbO_2}\to\mathrm{Hb},3.0,h_\mathrm{f}}$ (%) for different λ_1/λ_2 pairs and $h_\mathrm{f} = 0, 5, 10, 15$ mm.

		$C^{\lambda_1,\lambda_2}_{\mathrm{Hb}\to\mathrm{HbO_2},3.0,h_\mathrm{f}}$ (%)						$C^{\lambda_1,\lambda_2}_{\mathrm{HbO_2}\to\mathrm{Hb},3.0,h_\mathrm{f}}$ (%)					
Fat thickness	λ_2 (nm) ↓, λ_1 (nm) →	675	700	725	750	760	775	675	700	725	750	760	775
	825	-7.8	-14.3	-16.2	-9.1	-5.1	-7.9	1.3	4.2	8.8	5.0	2.6	6.8
0	850	-10.8	-16.2	-17.9	-12.3	-9.2	-12.1	2.2	5.7	11.9	8.4	6.0	13.3
mm	875	-13.1	-18.0	-19.7	-14.8	-12.1	-15.0	2.9	7.0	14.5	11.2	8.7	18.9
	900	-15.7	-20.6	-22.4	-17.8	-15.1	-18.5	3.6	8.3	17.4	14.2	11.6	25.3
	825	4.1	-16.3	-20.9	-7.6	-2.4	-9.1	-0.6	4.9	12.7	4.1	1.2	8.1
5	850	-4.0	-20.0	-23.8	-14.1	-10.3	-16.3	0.7	7.7	18.8	9.9	6.8	20.3
mm	875	-8.7	-22.9	-26.4	-18.1	-14.9	-20.5	1.8	10.1	24.1	14.9	11.5	31.1
	900	-12.0	-25.7	-29.3	-21.4	-18.4	-24.3	2.6	11.9	28.8	19.1	15.4	41.3
	825	10.3	-18.2	-24.5	-5.9	2.4	-9.6	-1.3	5.7	16.2	3.0	-1.1	8.7
10	850	-3.0	-24.1	-29.0	-16.3	-10.9	-20.4	0.5	10.4	27.1	12.2	7.3	29.0
mm	875	-9.6	-27.8	-32.1	-21.6	-17.2	-25.6	2.0	14.1	36.6	19.9	14.2	47.8
	900	-18.3	-34.0	-38.0	-29.4	-25.9	-33.6	4.5	20.9	56.3	34.8	27.4	93.6
	825	17.7	-15.1	-21.8	-2.0	8.6	-6.5	-2.1	4.5	13.5	1.0	-3.6	5.5
15	850	2.8	-21.6	-26.8	-13.4	-6.4	-18.1	-0.5	8.6	23.2	9.3	3.9	23.9
mm	875	-6.9	-27.0	-31.6	-21.1	-15.7	-25.7	1.4	13.4	35.4	19.0	12.5	48.2
	900	-24.8	-39.2	-42.8	-36.1	-32.7	-40.4	7.1	30.2	88.3	58.8	46.1	209.4

3.4 Discussion

We showed that the presence of fat tissue layer causes underestimation error and crosstalk problems in cw-NIRS muscle measurements and that these problems are fat thickness dependent. The main cause of these problems is the homogeneous medium assumption in the MBLL calculations with the use of a constant path length instead of fat thickness and wavelength dependent mean partial path length in the muscle layer. The fat layer has a lower absorption coefficient than the underlying muscle layer and it has been shown that as the fat layer thickens probed volume by NIRS system also increases (the "banana" gets fatter) [82, 84, 85, 98]. However as the banana gets fatter, probed muscle volume decreases ($<L_{\mathrm{m}}^{\lambda}>$ decreases). Thicker fat layer leads to an increase in $<L^{\lambda}>$, $<L_{\mathrm{f}}^{\lambda}>$ and detected light intensity for the considered wavelengths in the 675- to 900-nm range, as shown in section 3.3.1. Similar findings were reported in the literature such as the inverse relation between $<L_{\mathrm{m}}>$ and h_{f} found by simulation studies [86, 99, 82, 83, 98, 100, 23, 87] and by theoretical investigations [99]. Higher detected light intensities have been also reported for thicker fat layer [84, 85, 98, 22].

There is also a strong wavelength dependency of $<L_{\mathrm{m}}^{\lambda}>$. The concentration of HbO_2 (taken as 70%) is higher than [Hb], and for longer wavelengths $\epsilon_{\mathrm{HbO_2}}^{\lambda}$ is higher which result in $\mu_{a,\mathrm{m}}^{\lambda}$ increase, leading to a decrease in $<L_{\mathrm{m}}^{\lambda}>$ and $<L^{\lambda}>$ for longer wavelengths. In experimental studies, wavelength dependency has been reported [101, 102, 103] only for the DPF factor, since it is impossible to measure and isolate $<L_{\mathrm{m}}^{\lambda}>$ from a layered structure. Duncan et al. [102] reports DPF values of 4.43±0.86 (5.78±1.05) at 690 nm, and 3.94±0.78 (5.33±0.95) at 832 nm in the forearm (calf) for $r = 4.5$ cm. In the same study, a significant female/male difference in the DPF values was shown, with values of 4.34±0.78 for females and 3.53±0.55 for males in the forearm at 832 nm. For $r > 2.5$ cm, DPF has been shown to be almost constant by van der Zee et al. [103] where it was also stated that a female/male difference was present with mean DPF values of 5.14±0.43 for females versus 3.98±0.46 for males at 761 nm in the adult calf but no difference was observed in the adult forearm (both DPF are 3.59±0.32). A general trend of DPF decrease in 740- to 840-nm range was also found by Essenpreis et al. [101], although no significant female/male difference

was observed. In these studies, a female/male difference was attributed to fat/muscle ratio differences, although statistics concerning fat thicknesses were not present about the subjects in the studies.

In this study, we investigated the error in the estimation of the concentration changes using MBLL with homogeneous medium assumption under two headings: an underestimation error and crosstalk. We showed that fat thickness has a strong effect on both. The means of both absolute underestimation errors and absolute crosstalk over the considered wavelength pairs were calculated to be high for thick fat layer, as stated in sections 3.3.2 and 3.3.3. As stated, a decrease of $<L_{\mathrm{m}}^{\lambda}>$ with increased h_{f} and the use of a fixed DPF value in MBLL calculations because of the homogeneous medium assumption leads to rise in underestimation error. Crosstalk depends on $<L_{\mathrm{m}}^{\lambda}>$ but not the used DPF value when a wavelength independent DPF is used. The wavelength dependency of $\epsilon_{\mathrm{HbO_2}}^{\lambda}$ and $\epsilon_{\mathrm{Hb}}^{\lambda}$ as well as the difference between them also affect crosstalk.

The choice of wavelength pair had a significant impact on the errors. The variability in the absolute underestimation errors for different wavelength pairs is higher for low fat thickness values while the variability in the absolute crosstalk for different wavelength pairs increases with increasing fat thickness. The means of absolute underestimation errors and absolute crosstalk were found to be higher for $E_{\mathrm{HbO_2},3.0,h_{\mathrm{f}}}$ and $C_{\mathrm{Hb}\rightarrow\mathrm{HbO_2},3.0,h_{\mathrm{f}}}$. These findings are related to wavelength dependency of $<L_{\mathrm{m}}^{\lambda}>$ and specific absorption coefficients. Note $<L_{\mathrm{m}}^{\lambda}>$ has a decreasing trend at longer wavelengths and $\epsilon_{\mathrm{Hb}}^{\lambda}$ ($\epsilon_{\mathrm{HbO_2}}^{\lambda}$) is higher (lower) for wavelengths less than 798 nm, the isobestic point. In more detail, the reason for a higher underestimation error of $E_{\mathrm{HbO_2},3.0,h_{\mathrm{f}}}$ with respect to $E_{\mathrm{Hb},3.0,h_{\mathrm{f}}}$ can be explained by $\triangle\mathrm{OD}^{\lambda_2}$ ($\propto<L_{\mathrm{m}}^{\lambda_2}>$) being more heavily weighted by the real concentration change of $\triangle[\mathrm{HbO_2}]_{\mathrm{m}}$ in the muscle layer than $\triangle[\mathrm{Hb}]_{\mathrm{m}}$. In the MBLL equations, measured $\triangle\mathrm{OD}^{\lambda}$'s are assumed to be proportional to DPF $\times\, r$ instead of unavailable $<L_{\mathrm{m}}^{\lambda}>$. Wrongly used DPF $\times\, r$ overestimates the $<L_{\mathrm{m}}^{\lambda}>$ (leading to underestimation error for concentration change), however, the degree of path length overestimation is higher for longer wavelength since $<L_{\mathrm{m}}^{\lambda}>$ decreases with wavelength. Hence, the path length overestimation because of homogeneous medium assumption is higher for measured optical density change $\triangle\mathrm{OD}^{\lambda_2}$, leading to more underestimation

error for $\Delta[\mathrm{HbO_2}]_{\mathrm{MBLL}}$.

There is one previous study on crosstalk for muscle cw-NIRS measurements by Iwasaki and Okada [93]. This analysis was done for a fixed fat thickness of 4 mm, a two-wavelength system was assumed, λ_2 was fixed at 830 nm and r was taken as 2.0 or 4.0 cm. The 720/830-nm and 780/830-nm pairs were found to be the favorable pair selections resulting in minimal crosstalk. In our study, the 775/825-nm pair also gave low crosstalk values along with 750/825-nm and 760/825-nm pairs, for both $C^{\lambda_1,\lambda_2}_{\mathrm{HbO_2}\rightarrow\mathrm{Hb}}$ and $C^{\lambda_1,\lambda_2}_{\mathrm{Hb}\rightarrow\mathrm{HbO_2}}$. Iwasaki and Okada [93] found negative $C^{\lambda_1,\lambda_2}_{\mathrm{HbO_2}\rightarrow\mathrm{Hb}}$ values and positive $C^{\lambda_1,\lambda_2}_{\mathrm{Hb}\rightarrow\mathrm{HbO_2}}$ values; however, we calculated not only opposite signs but also different magnitudes. These could be due to choice of muscle absorption coefficients, the values in this study range between 2.1 to 3.7 times higher than the values used in our study. We also looked at the effect of fat thickness variation on crosstalk and found a rise in the mean of absolute crosstalk values over the considered wavelength pairs for an increase in fat thickness. Moreover, other λ_2 values were studied, up to 900 nm. There was an increase in crosstalk amplitudes for an increase in λ_2 for values higher than 825 nm for a fixed λ_1 at a given h_{f} value. The absolute values of $C^{\lambda_1,\lambda_2}_{\mathrm{HbO_2}\rightarrow\mathrm{Hb},3.0}$ and $C^{\lambda_1,\lambda_2}_{\mathrm{Hb}\rightarrow\mathrm{HbO_2},3.0}$ were calculated to be less than 11% for the 675/825-, 675/850-, 675/875-, 750/825-, 760/825-, 760/850-, 775/825-nm pairs for $h_{\mathrm{f}} < 10$ mm.

Arterial occlusion is employed in cw-NIRS measurements to estimate muscle oxygen consumption. In this case, ideally blood volume remains constant while $\Delta[\mathrm{HbO_2}]_{\mathrm{m}}$ decreases and $\Delta[\mathrm{Hb}]_{\mathrm{m}}$ increases in equal magnitudes in the probed volume. Using Eq. (3.13), the estimation errors were found to be 10.6±5.2, 30.7±4.6 and 54.6±4.1% for $\Delta[\mathrm{Hb}]_{\mathrm{MBLL}}$ and 15.1±4.3, 34.3±3.7 and 57.1±3.2% for $\Delta[\mathrm{HbO_2}]_{\mathrm{MBLL}}$ at $\mathrm{h}_f = 0, 2, 4$ mm respectively, computed over twenty four wavelength pairs ($r = 3.0$ cm, DPF = 4.37). These estimation errors for the two chromophores are closer compared to the differences between underestimation errors (section 3.3.2) due to the crosstalk. The estimation error for $\Delta[\mathrm{Hb}]_{\mathrm{MBLL}}$ is higher than the underestimation error $E_{\mathrm{Hb},3.0,h_{\mathrm{f}}}$ while the estimation error of $\Delta[\mathrm{HbO_2}]_{\mathrm{MBLL}}$ is lower than the underestimation error $E_{\mathrm{HbO_2},3.0,h_{\mathrm{f}}}$. For this protocol, the minimum estimation errors were found for the 700/825- and 725/825-nm pairs. For a fixed λ_2, the estimation errors for the occlusion

protocol were found to be low for choice of 700 or 725 nm as λ_1, while for fixed λ_1, errors rise for an increase in λ_2, for both $\Delta[\mathrm{HbO_2}]_{\mathrm{MBLL}}$ and $\Delta[\mathrm{Hb}]_{\mathrm{MBLL}}$.

The error analysis in this study showed the clear failure of the homogenous medium assumption and the requirement to correct cw-NIRS measurements even for low fat thickness values, although it was stated that correction may be no required for less than 5 mm fat thickness by Yang et al. [22]. There are already several proposed approaches for cw-NIRS measurement corrections, in particular for $\mathrm{m}\dot{V}\mathrm{O_2}$. Several investigators [84, 99, 23] have proposed correction algorithms using theoretically determined $<L_{\mathrm{m}}>$. Niwayama et al. [100, 104, 105] combined the results of simulations and experiments (for $<L_{\mathrm{m}}>$, detected light intensities, and experimental sensitivities) to obtain correction curves for $\mathrm{m}\dot{V}\mathrm{O_2}$. Utilizing these corrections, the variance of the experimental $\mathrm{m}\dot{V}\mathrm{O_2}$ results were reduced [100, 105], moreover, a higher correlation was found between $\mathrm{m}\dot{V}\mathrm{O_2}$ values measured by ^{31}P-NMR and corrected $\mathrm{m}\dot{V}\mathrm{O_2}$ values measured [104] by cw-NIRS. Yet another correction algorithm was proposed by the same group in which a relationship between detected light intensity and measurement sensitivity was utilized as an empirical technique to reduce the variance in $\mathrm{m}\dot{V}\mathrm{O_2}$ findings due to fat thickness [84, 85, 106]. Yang et al. [22] proposed a correction for intensity of cw-NIRS measurements using a polynomial fit to detected intensity change with fat thickness. Lin et al. [107] used a neural network based algorithm for spatially resolved reflectance, first to find the optical coefficients of the top layer and then that of the layer below, assuming the top layer thickness is known. There are also broadband cw-NIRS techniques. One method orthogonalizes the spectra collected at a long source-detector distance (r) to the spectra collected at a short r and maps to the long r space [108, 109]. Another one uses multiple detectors and the derivative of attenuation with respect to distance, utilizing a particular wavelength sensitive to fat thickness [110, 111].

Figure 3.4 shows four cw-NIRS measurement sensitivity curves. The first curve from our study is the calculated $\Delta[\mathrm{HbO_2}]_{\mathrm{MBLL}}$ computed for the ischemia protocol (for unit magnitude and opposite $\Delta[\mathrm{Hb}]_{\mathrm{m}}$ and $\Delta[\mathrm{HbO_2}]_{\mathrm{m}}$) using DPF = 4.37, at 750/850-nm pair ($r = 3.0$ cm). The computed $\Delta[\mathrm{Hb}]_{\mathrm{MBLL}}$ for the same conditions (not shown) has a slightly higher sensitivity. The sensitivity curve of Niwayama et al. [105] is

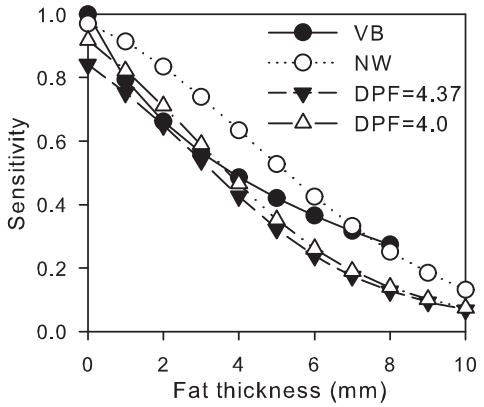

Figure 3.4 Normalized oxygen consumption curve of van Beekvelt et al. [2] (denoted by VB), measurement correction curve of Niwayama et al. [102] (denoted by NW), computed $\Delta[\mathrm{HbO_2}]_{\mathrm{MBLL}}$ for ischemia protocol (for unit magnitude and opposite $\Delta[\mathrm{Hb}]_{\mathrm{m}}$ and $\Delta[\mathrm{HbO_2}]_{\mathrm{m}}$ changes, obtained for 750/850 nm pair) with the use of DPF value of 4.37 (denoted by DPF=4.37) and 4.0 (denoted by DPF=4.0).

proposed for muscle measurement correction by dividing the calculated concentration changes by itself, given by $\exp(-(\frac{h_{\mathrm{f}}+h_{\mathrm{s}}}{8.0})^2)$ (using 760/840-nm pair, we take h_{s} to be 1.4 mm). The curve of Niwayama et al. [105] indicates higher sensitivity than the one our curve predicts. For the computed $\Delta[\mathrm{HbO_2}]_{\mathrm{MBLL}}$, taking a lower DPF value of 4.0 (the value used in the Niwayama et al. [105]) leads to a higher sensitivity. Yet another curve is derived from the experimental resting state oxygen consumption curve of van Beekvelt et al. [21] ($\mathrm{m}\dot{V}\mathrm{O_2}$=0.18-0.14$\times\log_{10}(h_{\mathrm{f}}+h_{\mathrm{s}})$ ml of $\mathrm{O_2.min^{-1}.100g^{-1}}$, used DPF = 4.0 cm, r = 3.5 cm, three wavelengths of 770/850/905 nm system, we take h_{s} as 1.4 mm) by normalizing it to its value at 0 mm fat thickness. The study had 78 volunteers with highest fat (plus skin) thickness of 8.9 mm (approximating a7.5 mm fat thickness), hence shown up to h_{f} = 8 mm. It is closer to our curve for low fat thickness values (<4 mm) but presents higher sensitivity for higher fat thickness values and becomes closer to the curve of Niwayama et al. [105]. van Beekvelt et al. [21] reports a 50% decrease in experimentally found oxygen consumption ($\mathrm{m}\dot{V}\mathrm{O_2}$) for fat thickness (including skin) in a range from 5 to 10 mm. Niwayama et al. [105, 100], report of a roughly 50% decrease in cw-NIRS measurement sensitivity for a two-fold increase in fat (including skin) thickness, but the range for fat thickness is not given. In our study, we calculated a nearly 55% decrease in the $\Delta[\mathrm{HbO_2}]_{\mathrm{MBLL}}$ and $\Delta[\mathrm{Hb}]_{\mathrm{MBLL}}$ for the ischemia protocol at 750/850- and 775/850-nm (the closest pairs to the wavelengths used in the mentioned studies) for h_{f} increase from 3 to 6 mm, while the decrease becomes nearly

34% for $h_f = 2$ to 4 mm, and 70% for $h_f = 4$ to 8 mm.

MBLL calculations are based on a linear approximation for the relationship of optical density change to absorption coefficient change, which leads to deviations for large concentration changes, as shown by Shao et al. [112]. The presence of the fat layer deteriorates the linearity of measurement characteristics investigated by Lin et al. [23]. In our study, we assumed small concentration changes. In quantitative studies aimed at oxygen consumption calculations, concentration change rates within small time scales during ischemia are typically used. In the experimental study of Ferrari et al. [113], difference of $\Delta[HbO_2]$ - $\Delta[Hb]$ was computed for ischemia alone and for ischemia with maximal voluntary contraction. For these measurements, desaturation rates were computed with constant DPF and with changing DPF values found using time resolved spectroscopy with the same experiment protocols. Similar rate values were calculated within short time scales.

The effect of fat layer thickness on the cw-NIRS measurements is very explicit and dominant; but it has to be stressed that partial path length values, detected intensities, underestimation errors, and crosstalk are all subject to both intrasubject and intersubject variability because of optical coefficients' variability of tissue layers, variability in physiological status, muscle anatomy differences, and anisotropy in the skin [114] and in the muscle [115].

An increase in the source-detector distance leads to lower errors because of increased $<L_m>$, however signal-to-noise ratio (SNR) also decreases since detected intensity decreases leading to a trade-off. It can be possible to find optimal source-detector distance based on optimization of SNR maximization and error minimization [98, 87], by also taking into account the fat thickness of the subject.

3.5 Conclusion

The fat layer influence on muscle cw-NIRS measurements based on MBLL calculations with homogeneous medium assumption was investigated for both underestimation error and crosstalk using Monte Carlo simulations for a two wavelength system. Although the computed values of underestimation errors and crosstalk are dependent on the "true" optical coefficients of the tissue layers, and hence could change for each subject, an explicit finding is that the mean values of the absolute underestimation errors and absolute crosstalk computed over the considered wavelength pairs increase for the thicker fat layer. The means of absolute underestimation errors $E_{\mathrm{HbO_2},3.0,h_\mathrm{f}}$ and absolute crosstalk $C_{\mathrm{Hb}\rightarrow\mathrm{HbO_2},3.0,h_\mathrm{f}}$ over the considered wavelength pairs were found to be higher, while due to the crosstalk the estimation errors for the concentration changes of the two chromophores were calculated to be closer for the ischemia protocol. These errors also depended on the wavelength pair selection for the two wavelength system with greater impact on the crosstalk. This dependency of wavelength leads to the fact that correction algorithms should be dependent on the choice of wavelengths, although different wavelength combinations can have very similar sensitivities. The measurement of the fat thickness values and providing information about it should become a standard routine as suggested by van Beekvelt et al. [116] for the cw-NIRS measurements.

4. CORRECTION ALGORITHMS for SINGLE DETECTOR cw-NIRS

Fat layer has an explicit effect on the accuracy of cw-NIRS measurements which is investigated in detail in chapter 3. Hence correction algorithms are needed for the cw-NIRS measurements. In the literature, most of the researches which have utilized cw-NIRS technique need correction because of the use of constant DPF. Some studies tried to minimize fat thickness effect problem by selecting the subjects having fat thicknesses within narrow range.

4.1 Use of $< L_{\mathrm{m}}^{\lambda} >$ Instead of Constant Mean Path Length

In the homogeneous medium assumption based MBLL calculations, light is assumed to pass through a homogeneous medium which in fact consists of skin, fat and muscle tissue structures. A more realistic case would be assuming that the tissue is heterogenous made of these three tissue structures and these structures are homogeneously layered on top of each other, and muscle thickness can be taken infinite. Partial path length in the muscle layer then can be found by Monte Carlo simulations for the measured superficial skin and fat thicknesses. $< L_{\mathrm{m}}^{\lambda} >$ would be used in the MBLL calculations instead of constant path length computed as $r \times \mathrm{DPF}$ with constant DPF. Formulas for computations of $\Delta[\mathrm{Hb}]$ and $\Delta[\mathrm{HbO_2}]$ then would be

$$\Delta[\mathrm{Hb}] = \frac{< L_{\mathrm{m}}^{\lambda_2} > \epsilon_{\mathrm{HbO_2}}^{\lambda_2} \Delta \mathrm{OD}^{\lambda_1} - < L_{\mathrm{m}}^{\lambda_1} > \epsilon_{\mathrm{HbO_2}}^{\lambda_1} \Delta \mathrm{OD}^{\lambda_2}}{< L_{\mathrm{m}}^{\lambda_2} >< L_{\mathrm{m}}^{\lambda_1} > \left(\epsilon_{\mathrm{HbO_2}}^{\lambda_2} \epsilon_{\mathrm{Hb}}^{\lambda_1} - \epsilon_{\mathrm{HbO_2}}^{\lambda_1} \epsilon_{\mathrm{Hb}}^{\lambda_2} \right)} \tag{4.1}$$

$$\Delta[\mathrm{HbO_2}] = \frac{< L_{\mathrm{m}}^{\lambda_1} > \epsilon_{\mathrm{Hb}}^{\lambda_1} \Delta \mathrm{OD}^{\lambda_2} - < L_{\mathrm{m}}^{\lambda_2} > \epsilon_{\mathrm{Hb}}^{\lambda_2} \Delta \mathrm{OD}^{\lambda_1}}{< L_{\mathrm{m}}^{\lambda_2} >< L_{\mathrm{m}}^{\lambda_1} > \left(\epsilon_{\mathrm{HbO_2}}^{\lambda_2} \epsilon_{\mathrm{Hb}}^{\lambda_1} - \epsilon_{\mathrm{HbO_2}}^{\lambda_1} \epsilon_{\mathrm{Hb}}^{\lambda_2} \right)} \tag{4.2}$$

The basic difference between these formulas and formulas of MBLL with homogeneous medium assumption given in the chapter 3.1.1 is that partial path length in the muscle layer $< L_{\mathrm{m}}^{\lambda} >$ is used instead of wrongly used mean path length in the tissue (taken as $\mathrm{DPF}^{\lambda} r$). Eq. 4.1 and 4.2 can be also used for previously taken cw-NIRS measurements

if $\triangle \mathrm{OD}^{\lambda}$ signals are stored and available as well as fat thickness information.

Tabulated values of $< L_{\mathrm{m}}^{\lambda} >$ for 1.4 mm skin thickness are given in Table C.3 for $r = 3.0$ cm in the appendix C. These values are found using Monte Carlo simulations for the optical coefficients given in the Table 3.1. Computed values of $< L_{\mathrm{m}}^{\lambda} >$ for source detector distances of 2.0, 2.5, 3.5, 4.0 and 4.5 cm are given also in appendix C.

This fat layer affect correction methodology suffers from the variability of optical coefficients of tissue layers between the subjects, variability in physiological status, muscle anatomy differences, anisotropy in the skin [114] and in the muscle [115]. The accuracy of correction is dependent on the how much close the assumed optical coefficients are to the real unknown values for each subject.

4.2 Correction Curves for Concentration Changes

Reported parameters in previously published articles and research reports are concentration changes or oxygen consumptions without fat layer effect correction. These are derived parameters from OD^{λ} signals using MBLL mostly derived with constant mean path length. Calculation formulas are needed for these parameters. A correction formula is described in chapter 3 for the ischemia protocol which is used to estimate muscle oxygen consumption for which it can be assumed that (ideally) blood volume stays constant while $\Delta[\mathrm{HbO_2}]_{\mathrm{m}}$ decreases and $\Delta[\mathrm{Hb}]_{\mathrm{m}}$ increases in equal magnitudes in the probed volume. $\Delta[\mathrm{Hb}]_{\mathrm{MBLL}}$ and $\Delta[\mathrm{HbO_2}]_{\mathrm{MBLL}}$ with these assumptions are calculated (using Eq. (3.13)) for unit magnitude $\Delta[\mathrm{HbO_2}]_{\mathrm{m}}$ and $\Delta[\mathrm{Hb}]_{\mathrm{m}}$ and be used to correct measured concentration changes. These calculated $\Delta[\mathrm{Hb}]_{\mathrm{MBLL}}$ and $\Delta[\mathrm{HbO_2}]_{\mathrm{MBLL}}$ then can be used correction curves. Remembering formulas for MBLL;

$$\Delta[\mathrm{Hb}]_{\mathrm{MBLL}} = \frac{\frac{\epsilon_{\mathrm{HbO_2}}^{\lambda_2}\Delta\mathrm{OD}^{\lambda_1}}{\mathrm{DPF}^{\lambda_1}} - \frac{\epsilon_{\mathrm{HbO_2}}^{\lambda_1}\Delta\mathrm{OD}^{\lambda_2}}{\mathrm{DPF}^{\lambda_2}}}{r\left(\epsilon_{\mathrm{HbO_2}}^{\lambda_2}\epsilon_{\mathrm{Hb}}^{\lambda_1} - \epsilon_{\mathrm{HbO_2}}^{\lambda_1}\epsilon_{\mathrm{Hb}}^{\lambda_2}\right)} \tag{4.3}$$

$$\Delta[\mathrm{HbO_2}]_{\mathrm{MBLL}} = \frac{\frac{\epsilon_{\mathrm{Hb}}^{\lambda_1}\Delta\mathrm{OD}^{\lambda_2}}{\mathrm{DPF}^{\lambda_2}} - \frac{\epsilon_{\mathrm{Hb}}^{\lambda_2}\Delta\mathrm{OD}^{\lambda_1}}{\mathrm{DPF}^{\lambda_1}}}{r\left(\epsilon_{\mathrm{HbO_2}}^{\lambda_2}\epsilon_{\mathrm{Hb}}^{\lambda_1} - \epsilon_{\mathrm{HbO_2}}^{\lambda_1}\epsilon_{\mathrm{Hb}}^{\lambda_2}\right)} \tag{4.4}$$

In this case, $\Delta[\mathrm{Hb}]_{\mathrm{m}}$ can be taken to be equal to 1 and in the same way $\Delta[\mathrm{HbO_2}]_{\mathrm{m}}$ is accepted as -1 for unit magnitude and opposite concentration changes of Hb and $\mathrm{HbO_2}$ in the muscle layer. Measured optical density changes can be modeled with the use of Eq. 3.6 as;

$$\Delta \mathrm{OD}^{\lambda} \cong \left(\epsilon^{\lambda}_{\mathrm{Hb}} \times 1 + \epsilon^{\lambda}_{\mathrm{HbO_2}} \times (-1)\right) <L^{\lambda}_{\mathrm{m}}> \tag{4.5}$$

MBLL equations end up with the following formulas when this $\Delta \mathrm{OD}^{\lambda}$ is used;

$$\Delta[\mathrm{Hb}]_{\mathrm{MBLL\_U\_ISC}} = \frac{\frac{\epsilon^{\lambda_2}_{\mathrm{HbO_2}}\left(\epsilon^{\lambda_1}_{\mathrm{Hb}}-\epsilon^{\lambda_1}_{\mathrm{HbO_2}}\right)<L^{\lambda_1}_{\mathrm{m},r,h_{\mathrm{f}}}>}{\mathrm{DPF}^{\lambda_1}} - \frac{\epsilon^{\lambda_1}_{\mathrm{HbO_2}}\left(\epsilon^{\lambda_2}_{\mathrm{Hb}}-\epsilon^{\lambda_2}_{\mathrm{HbO_2}}\right)<L^{\lambda_2}_{\mathrm{m},r,h_{\mathrm{f}}}>}{\mathrm{DPF}^{\lambda_2}}}{r\left(\epsilon^{\lambda_2}_{\mathrm{HbO_2}}\epsilon^{\lambda_1}_{\mathrm{Hb}} - \epsilon^{\lambda_1}_{\mathrm{HbO_2}}\epsilon^{\lambda_2}_{\mathrm{Hb}}\right)} \tag{4.6}$$

$$\Delta[\mathrm{HbO_2}]_{\mathrm{MBLL\_U\_ISC}} = \frac{\frac{\epsilon^{\lambda_1}_{\mathrm{Hb}}\left(\epsilon^{\lambda_2}_{\mathrm{Hb}}-\epsilon^{\lambda_2}_{\mathrm{HbO_2}}\right)<L^{\lambda_2}_{\mathrm{m},r,h_{\mathrm{f}}}>}{\mathrm{DPF}^{\lambda_2}} - \frac{\epsilon^{\lambda_2}_{\mathrm{Hb}}\left(\epsilon^{\lambda_1}_{\mathrm{Hb}}-\epsilon^{\lambda_1}_{\mathrm{HbO_2}}\right)<L^{\lambda_1}_{\mathrm{m},r,h_{\mathrm{f}}}>}{\mathrm{DPF}^{\lambda_1}}}{r\left(\epsilon^{\lambda_2}_{\mathrm{HbO_2}}\epsilon^{\lambda_1}_{\mathrm{Hb}} - \epsilon^{\lambda_1}_{\mathrm{HbO_2}}\epsilon^{\lambda_2}_{\mathrm{Hb}}\right)} \tag{4.7}$$

Denominator MBLL_U_ISC (U for unit magnitude concentration changes and ISC for ischemia) means that these are the computed concentration changes with homogeneous medium assumption based MBLL formulation for ischemia protocol with the unit and opposite concentration changes of $\Delta[\mathrm{Hb}]_{\mathrm{m}}$ and $\Delta[\mathrm{HbO_2}]_{\mathrm{m}}$. $<L^{\lambda}_{\mathrm{i},r,h_{\mathrm{f}}}>$ is found using Monte Carlo simulations for specific fat thickness h_{f}, source detector distance r and optical coefficients of the tissue layers, as described in the chapters 2 and 3.

Obtained values of $\Delta[\mathrm{Hb}]_{\mathrm{MBLL\_U\_ISC}}$ and $\Delta[\mathrm{HbO_2}]_{\mathrm{MBLL\_U\_ISC}}$ can be used for correction by diving the measured variable calculated with MBLL formulation by itself as follows;

$$\text{Corrected Value for } \Delta[\mathrm{Hb}] = \frac{\Delta[\mathrm{Hb}]_{\mathrm{MBLL}}}{\Delta[\mathrm{Hb}]_{\mathrm{MBLL\_U\_ISC}}} \tag{4.8}$$

$$\text{Corrected Value for } \Delta[\mathrm{HbO_2}] = \frac{\Delta[\mathrm{HbO_2}]_{\mathrm{MBLL}}}{\Delta[\mathrm{HbO_2}]_{\mathrm{MBLL\_U\_ISC}}} \tag{4.9}$$

Another variable is $\mathrm{Hb_{diff}}$ also called oxygenation index (OI or *oxy*). It is defined as;

$$\mathrm{Hb_{diff}} = \Delta[\mathrm{HbO_2}]_{\mathrm{MBLL}} - \Delta[\mathrm{Hb}]_{\mathrm{MBLL}} \tag{4.10}$$

Decrease rate of this variable is commonly used to derive oxygen consumption in the muscle instead of $\triangle$[Hb] increase rate or $\triangle$[HbO_2] decrease rate [51]. As discussed in the study of Van Beekvelt et al. [51], total hemoglobin increases are found in this study and in other studies with arterial occlusion protocols which could be due to blood redistribution or incomplete occlusion. Since selection of wrong variable will increase error, use of the variable Hb_{diff} is advised.

Using this variable, $m\dot{V}O_2$ is found from half of decrease rate of Hb_{diff}. Correction function can be again found for ischemia protocol as follows;

$$\text{Corrected Value for } m\dot{V}O_2 \quad = \quad \frac{m\dot{V}O_{2\text{MBLL}}}{m\dot{V}O_{2\text{MBLL\_U\_ISC}}} \tag{4.11}$$

where $m\dot{V}O_{2\text{MBLL\_U\_ISC}}$ is found from the formula below;

$$m\dot{V}O_{2\text{MBLL\_U\_ISC}} = -0.5 \times \frac{d(\Delta[\text{HbO}_2]_{\text{MBLL\_U\_ISC}} - \Delta[\text{Hb}]_{\text{MBLL\_U\_ISC}})}{dt} \tag{4.12}$$

4.2.1 Correction of Data in the Literature

For the comparison of the correction formulas, the most comprehensive reported data in the literature is used. That is the data of van Beekvelt et al. [21], where 78 people (34 female, 44 male) participated in the study. Oxygen consumption values of 77 people (33 female, 44 male) were given in the study along with forearm blood flow values for resting state and isometric hand grip exercise at levels of 10%, 20% and 30% MVC. In this study, Oxymon cw-NIRS device (Biomedical Engineering Department, University of Nijmegen, NL) was used which generates light at 905, 850 and 770 nm (used DPF = 4.0 cm, r = 3.5 cm). In this study, a correction curve is proposed using the fitted function to the resting state oxygen consumptions of the subjects, given as $m\dot{V}O_2$=0.18-0.14$\times\log_{10}(h_f + h_s)$ ml of O_2.min^{-1}.100g^{-1}. We utilized this function as a correction curve by normalizing it to its value at 0 mm fat thickness (h_s is taken as 1.4 mm).

This study of van Beekvelt et al. [21] used three wavelength cw-NIRS system.

Hence a correction curve is derived like the previous formulations but for a three wavelength system. The MBLL formulation for homogeneous medium assumption is ;

$$\begin{bmatrix} \Delta\mathrm{OD}^{\lambda_1} \\ \Delta\mathrm{OD}^{\lambda_2} \\ \Delta\mathrm{OD}^{\lambda_3} \end{bmatrix} = \begin{bmatrix} \epsilon^{\lambda_1}_{\mathrm{Hb}} < L^{\lambda_1} > & \epsilon^{\lambda_1}_{\mathrm{HbO_2}} < L^{\lambda_1} > \\ \epsilon^{\lambda_2}_{\mathrm{Hb}} < L^{\lambda_2} > & \epsilon^{\lambda_2}_{\mathrm{HbO_2}} < L^{\lambda_2} > \\ \epsilon^{\lambda_3}_{\mathrm{Hb}} < L^{\lambda_3} > & \epsilon^{\lambda_3}_{\mathrm{HbO_2}} < L^{\lambda_3} > \end{bmatrix} \times \begin{bmatrix} \Delta[\mathrm{Hb}] \\ \Delta[\mathrm{HbO_2}] \end{bmatrix} \tag{4.13}$$

Hence formula for finding concentration changes' for 3 wavelength cw-NIRS system is;

$$\Delta\mathbf{C} = (\mathbf{B}^{\mathrm{T}}\mathbf{B})^{-1}\mathbf{B}^{\mathrm{T}} \times \Delta\mathbf{OD}_{\mathrm{measured}} \tag{4.14}$$

where $\Delta\mathbf{C} = \begin{bmatrix} \Delta[\mathrm{Hb}]_{\mathrm{MBLL}} \\ \Delta[\mathrm{HbO_2}]_{\mathrm{MBLL}} \end{bmatrix}$, $\mathbf{B} = \begin{bmatrix} \epsilon^{\lambda_1}_{\mathrm{Hb}} < L^{\lambda_1} > & \epsilon^{\lambda_1}_{\mathrm{HbO_2}} < L^{\lambda_1} > \\ \epsilon^{\lambda_2}_{\mathrm{Hb}} < L^{\lambda_2} > & \epsilon^{\lambda_2}_{\mathrm{HbO_2}} < L^{\lambda_2} > \\ \epsilon^{\lambda_3}_{\mathrm{Hb}} < L^{\lambda_3} > & \epsilon^{\lambda_3}_{\mathrm{HbO_2}} < L^{\lambda_3} > \end{bmatrix}$. In this formulation, generally wavelength independent constant value is used for $< L^{\lambda_1} >$ (i.e. it is equal to 4.0 × 3.5 cm in the study of van Beekvelt et al. [21]).

Correction for this MBLL formulation is found by finding concentration changes for ideal ischemia protocol. Assuming homogeneously layered skin-fat-muscle heterogenous tissue model, $\Delta\mathbf{OD}_{\mathrm{measured}}$ is equal to $\mathbf{B}_m \times \begin{bmatrix} 1 \\ -1 \end{bmatrix}$ for unit magnitude concentration changes, where $\mathbf{B}_m = \begin{bmatrix} \epsilon^{\lambda_1}_{\mathrm{Hb}} < L^{\lambda_1}_{\mathrm{m},r,h_{\mathrm{f}}} > & \epsilon^{\lambda_1}_{\mathrm{HbO_2}} < L^{\lambda_1}_{\mathrm{m},r,h_{\mathrm{f}}} > \\ \epsilon^{\lambda_2}_{\mathrm{Hb}} < L^{\lambda_2}_{\mathrm{m},r,h_{\mathrm{f}}} > & \epsilon^{\lambda_2}_{\mathrm{HbO_2}} < L^{\lambda_2}_{\mathrm{m},r,h_{\mathrm{f}}} > \\ \epsilon^{\lambda_3}_{\mathrm{Hb}} < L^{\lambda_3}_{\mathrm{m},r,h_{\mathrm{f}}} > & \epsilon^{\lambda_3}_{\mathrm{HbO_2}} < L^{\lambda_3}_{\mathrm{m},r,h_{\mathrm{f}}} > \end{bmatrix}$ and $< L^{\lambda_1}_{\mathrm{m},r,h_{\mathrm{f}}} >$ are the values found with Monte Carlo simulations. Then concentration changes are found as;

$$\begin{bmatrix} \Delta[\mathrm{Hb}]_{\mathrm{MBLL\_U\_ISC}} \\ \Delta[\mathrm{HbO_2}]_{\mathrm{MBLL\_U\_ISC}} \end{bmatrix} = (\mathbf{B}^{\mathrm{T}}\mathbf{B})^{-1}\mathbf{B}^{\mathrm{T}} \times \mathbf{B}_m \times \mathbf{U} \tag{4.15}$$

where $\mathbf{U} = \begin{bmatrix} 1 \\ -1 \end{bmatrix}$. These calculated concentration changes are for unit magnitude and opposite concentration changes of Hb and $\mathrm{HbO_2}$ and they can be used for correction using the Eq. 4.8, 4.9 and 4.11. A correction curve is derived for the data presented in van Beekvelt et al. [21] using $< L^{\lambda_1}_{\mathrm{m},r,h_{\mathrm{f}}} >$ values found with Monte Carlo simulations (given in appendix C) for $r = 3.5$ cm, and at 775/850/900 nm, the closest ones to the

used wavelengths 905, 850 and 770 in van Beekvelt et al. [21].

One of the used correction curve is from the study of Niwayama et al. [105] who employed NIRO-500 continuous-wave photometer (Hamamatsu Photonics, Hamamatsu City, Japan). Two wavelength cw-NIRS is used in the study with the wavelengths of 760 and 840 nm. Using Monte Carlo simulation and experiments, they have come up with the correction formula;

$$S_{muscle} = exp\left[-\left(\frac{h_s + h_f}{A}\right)^2\right] \tag{4.16}$$

where S_{muscle} is used by dividing the measured concentration changes by itself. The value of A is given as 6.9, 8.0 and 8.9 for skin plus fat thickness values of 2, 3 and 4 cm. This curve is referenced as Niwayama-1 in this section (used value of A is 8.45 average of 8.0 and 8.9 for $r = 3.5$ cm).

Another curve is again from a study of Niwayama et al. [104] where correction function is given as

$$S_{muscle} = exp\left[-\left(\frac{h_s + h_f}{A_1}\right)^2\right] - A_2 G(\alpha, \beta) \tag{4.17}$$

where $G(\alpha, \beta)$ is gamma function ($= \frac{1}{\beta^\alpha \Gamma(\alpha)}(h_f + h_s)^{\alpha-1} e^{-(h_f+h_s)/\beta}$) and S_{muscle} is used as above. The constants A_1, A_2, α, and β are given as 9.9, 1.49, 8.9 and 1.09, respectively for source-detector distance of 3 cm. This curve is referenced as Niwayama-2 in this section.

The results of applying corrections to the resting state oxygen consumption values are given in the study of van Beekvelt et al. [21] are given in the Figure 4.1 and Table 4.1. In the original data, an explicit decline in the oxygen consumption values of the subjects is evident. Moreover there is a wide variability in the values even for small fat thickness ranges which indicates physiological variability besides fat thickness effect. The four correction curves all resulted in smaller variabilities compared to the raw data. The decline in the values with h_f increase is smaller after corrections.

Table 4.1
Results of the correction curves for the oxygen consumption values given in the study of van Beekvelt et al. [2]

		Correction with the function of			
	Original	Beekvelt	Niwayama-1	Niwayama-2	Our
Mean Value (ml of O_2.min^{-1}.100g^{-1})	0.11	0.16	0.13	0.13	0.16
Standard Deviation	0.04	0.04	0.04	0.04	0.04
CV (%)	38.4	28.8	29.0	28.2	27.9

However, difference between them shows itself in the Figure 4.1. The all curves is in similar ranges below $h_f = 1.5$ mm. Our curve leads to higher values for thicker fat thicknesses than ~ 5 mm. Sensitivity curves are also shown in the Figure 4.2. As it has been stated in section 3.4, our sensitivity curve is close to the derived correction function from van Beekvelt et al. [21] for $h_f < 6$ mm. Our curve seems to indicate lower sensitivity compared to other correction curves for thicker fat than 6 mm.

The difference between curves results from the assumed optical properties of the tissue layers. The experimentally derived ones depend on subject pool also. An important point is that there is a physiological variability which can not be reduced. Hence the aim is just removing the effect of fat layer. A solution could be getting tissue layer optical properties for each subject once with the help of complex NIRS methods (i.e. frequency domain or time domain NIRS). Found optical parameters can then be used in the Monte Carlo simulations to find partial path lengths in the skin, fat and muscle tissues which can then be utilized in the cw-NIRS measurements instead of the erroneously used constant $r\times$DPF value. This method will also suffer from subject physiological variability, change of blood volume during exercise and change of optical properties (both $\mu_{a,m}$ and $\mu'_{s,m}$) during exercise and ischemia. Assumption and use of constant optical scattering on measurements of muscle oxygenation by near infrared spectroscopy during exercise is studied in the work of Ferreira et al. [117]. They found that this assumption leads to an overestimation of the changes in NIRS variables during exercise as well as distortion of the recovery kinetics. Ferrari et al. reports 5% decrease

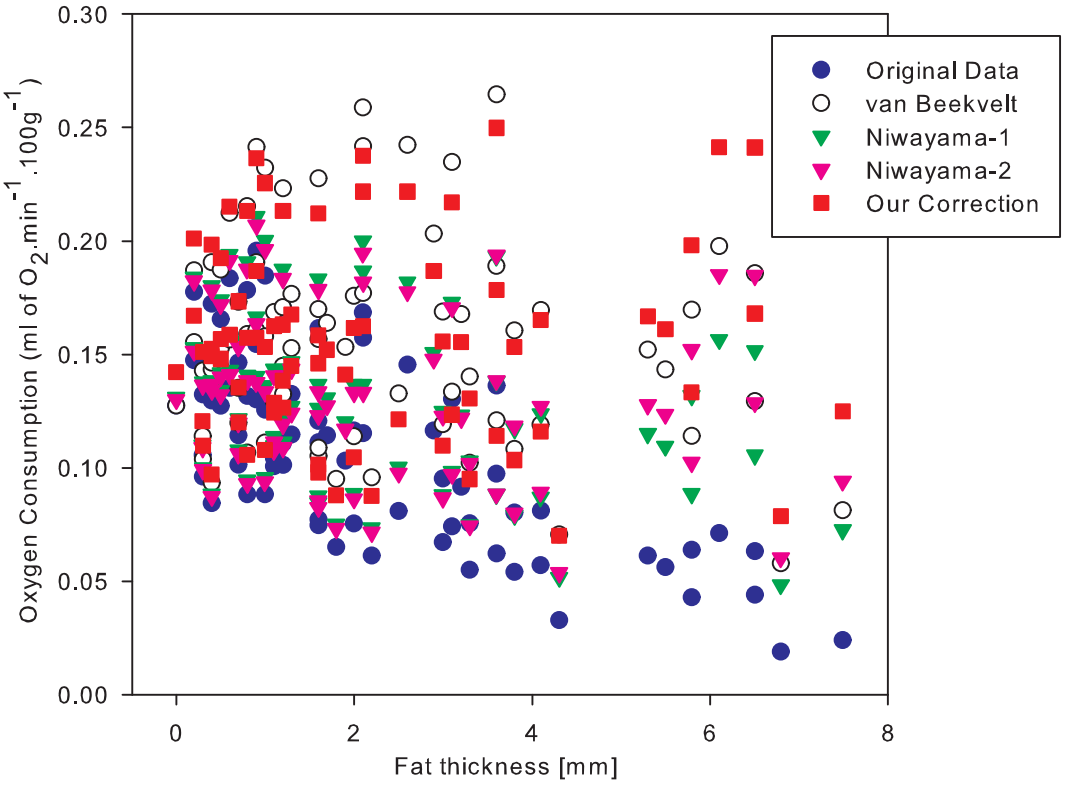

Figure 4.1 The oxygen consumption values of van Beekvelt et al. [2] and corrected values using two different curves of Niwayama et al. [101,102] and our correction curve explained in the text

during 10 minutes forearm venous outflow restriction [118] and 5-10% decrease during forearm ischemia with and without maximal voluntary contraction and during brain hypoxic hypoxia [113]. DPF is also found to be varied by 4-10% during the occlusion through arm [20]. Large changes in DPF also needs attention since small concentration change assumption does not hold, which is investigated by Shao et al. [112].

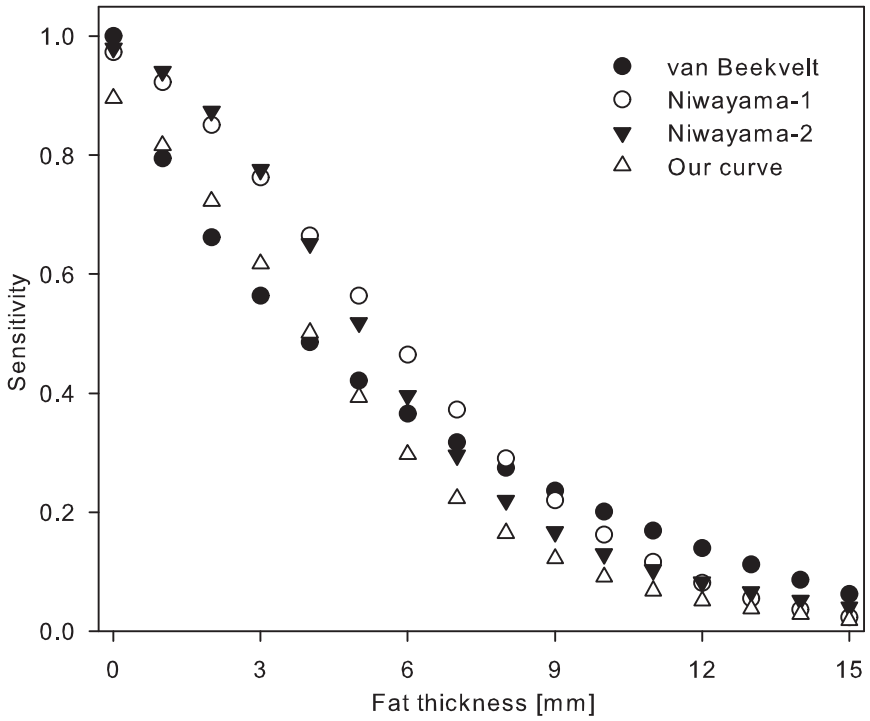

Figure 4.2 Sensitivity curves of van Beekvelt et al. [2] , Niwayama et al. [101,102] and the curve derived in this study (for 775/850/900 nm wavelength triple, $r = 3.5$ cm, DPF = 4.0)

5. TWO-DISTANCE PARTIAL PATHLENGTH METHOD FOR ACCURATE MEASUREMENT OF MUSCLE OXIDATIVE METABOLISM USING FNIRS

In cw-NIRS a dc-intensity light is sent through the tissue and changes in the intensities of reflected light at multiple wavelengths are used to calculate changes in concentrations of Hb and HbO_2. Two different methods, diffusion theory analysis and modified Beer-Lambert law are used in cw-NIRS to calculate concentration changes. Assumption of homogenous single medium in the calculations with these two methods lead to error in the calculation of focal changes in the tissues [79, 77, 76]. Tissues are multilayered and each layer has different optical properties. In the case of muscle measurements, measured volume does not contain muscle layer alone but also skin and fat layers above [119]. Even these layers, i.e. skin, may not be homogeneous layers. Skin layer is further composed of epidermis and dermis layers. It has been shown that fat layer leads to underestimation of muscle metabolism [21].

In this study, accurate estimation of absorption changes in the muscle layer as well as fat layer is investigated using multi layered geometry. Extension of modified Beer-Lambert Law to heterogeneous medium with homogeneous layered regions [18, 69] is used and compared to single layered assumption based calculation of absorption changes. Monte-Carlo simulations were used to generate detected light intensity (reflectance) change for two layered media composed of fat and muscle layers. It has been found that for 2-detector partial pathlength based method, estimates are better than the 1-detector based modified Beer-Lambert law estimates in all cases. Estimates are better for muscle layer and also for fat layer absorption coefficient change estimates.

5.1 THEORY

5.1.1 Modified Beer-Lambert Law

For a medium with homogeneous absorption change assumption, modified Beer-Lambert law can be stated as

$$OD = ln\left(\frac{I_0}{I}\right) = \mu_a \times DP + G \tag{5.1}$$

where OD is called optical density, DP is differential pathlength which equals mean distance $< L >$ travelled by the photons reaching the detector, I_0 is the intensity of sent light and I is the intensity of received light, μ_a is the absorption coefficient of the medium. Differential pathlength depends on all the absorption coefficient μ_a, scattering coefficient μ_s, single-scattering phase function and geometry. Loss of light due to scattering is represented in G which depends on scattering coefficient μ_s and scattering phase function of the medium but not on absorption coefficient. The parameters are wavelength dependent. This formulation is valid for small changes of μ_a where DP is approximately constant [18, 9, 64].

In cw-NIRS, change in the received light intensity is observed and recorded. Using modified Beer-Lambert Law, change in OD is proportional to change in absorption coefficient of the medium.

$$\triangle OD = \triangle \mu_a \times < L > \tag{5.2}$$

where it is assumed that G does not change during the measurement (i.e. μ_s and scattering characteristics do not change). Hence change in absorption coefficient is found using the formula;

$$\triangle \mu_a = \frac{\triangle OD}{< L >} \tag{5.3}$$

5.1.2 Two-distance Partial Pathlength Method

It is possible to extend modified Beer-Lambert law to heterogeneous medium with homogeneous layered regions [18]. In the study of of Hiraoka et al. [18], it is found that total attenuation change is the sum of attenuation changes in each layer. Then the total attenuation change is;

$$\triangle OD = \sum_{i=1}^{n} < L_i > \triangle \mu_{a,i} \tag{5.4}$$

where $< L_i >$ is the mean pathlength taken in the layer i by the photons reaching the detector and $\mu_{a,i}$ is the change in absorption coefficient of layer i and n is the number of layers in the medium.

For the case of muscle measurements, the medium can be modelled using homogeneous fat layer and muscle layer below. Following the formulation in Eq. 5.4, $\triangle OD$ at distances r_1 and r_2 from the light source can be modelled as;

$$\triangle OD^{r1} = \triangle \mu_{a,fat} \times < L^{r1}_{fat} > + \triangle \mu_{a,muscle} \times < L^{r1}_{muscle} > \tag{5.5}$$

$$\triangle OD^{r2} = \triangle \mu_{a,fat} \times < L^{r2}_{fat} > + \triangle \mu_{a,muscle} \times < L^{r2}_{muscle} > \tag{5.6}$$

Changes in the absorption coefficients of fat and in particular muscle tissue layers can be found by detecting the intensity changes at two distinct detector locations using Eq. 5.5 and 5.6. Solving these equations for $\mu_{a,fat}$ and $\mu_{a,muscle}$;

$$\triangle \mu_{a,fat} = \left(< L^{r2}_{muscle} > \triangle OD^{r1} - < L^{r1}_{muscle} > \triangle OD^{r2} \right) / A \tag{5.7}$$

$$\triangle \mu_{a,muscle} = \left(< L^{r1}_{fat} > \triangle OD^{r2} - < L^{r2}_{fat} > \triangle OD^{r1} \right) / A \tag{5.8}$$

denominator A is $(< L^{r1}_{fat} >< L^{r2}_{muscle} > - < L^{r2}_{fat} >< L^{r1}_{muscle} >)$. Assumption in this derivation is that change in absorption coefficients are small compared to initial values. This method requires initial optical properties of the layers to estimate partial pathlengths.

5.2 Monte Carlo Simulations

In Monte Carlo simulation of photon propagation in biological tissue, a stochastic model is constructed in which rules of photon propagation are modelled as probability distributions [24, 18]. In the simulation, photons were launched with initial weight (w) of 1. In layer i which has absorption coefficient $\mu_{a,i}$, scattering coefficient $\mu_{s,i}$ and reduced scattering coefficient $\mu_{s,i}{}'$ $(= (1-g)\mu_{s,i})$ (g is the mean cosine of the single scattering phase function and it is called anisotropy factor), successive scattering distances were selected using random variable $s = -ln(R)/\mu_{s,i}{}'$, R having uniform distribution over $(0, 1)$. Scatter deflection angles were found from Henyey-Greenstein function [120] with anisotropy factor of 0 using principle of similarity [7]. Scatter azimuthal angle was uniformly distributed over the interval $[0, 2\pi)$. Total distance traveled in layer i by each photon (L_i) was found by summing scattering lengths taken in this layer. Photon propagation was continued until photon escapes the medium or photon travels 220 cm in length (10 [ns]). For the photons reaching surface, photon exit weight is calculated using Lambert-Beer law as $w = exp(\sum -(L_i \mu_{a,i}))$, i.e. $w = exp(\sum -(L_{fat}\mu_{a,fat} + L_{muscle}\mu_{a,muscle}))$ for the two layered fat-muscle medium. Because of the symmetry of the mediums considered, photons reaching a ring (thickness dr, distance to light source r) were taken as the photons reaching the detector. Mean partial pathlength in medium i ($< L_i >$) for the detected photons was found using the formula $< L_i >= \sum_j^N L_{i,j} \cdot w_j / (\sum_k^N w_k)$, where $L_{i,j}$ is the path taken in medium i by detected photon j, w is the detected photon weight, N is total number of detected photons. Refractive indices of air and tissues were taken to be 1 and 1.4, respectively.

Medium geometry of the simulations is shown in Figure 5.1. It consists of fat layer and below muscle layer. Thickness of fat layer is taken to be 0.3 [cm] and muscle layer is practically infinite. Optical properties of the fat and muscle layers are taken from the in vitro measurements of Lin et al. [86] and 10^8 photon packets were injected into the medium for statistical accuracy. Simulations were made to generate detected light intensity (reflectance) changes at different detector locations for the two layered fat-muscle mediums. Thickness of the ring 'dr' was taken to be 0.1 [cm].

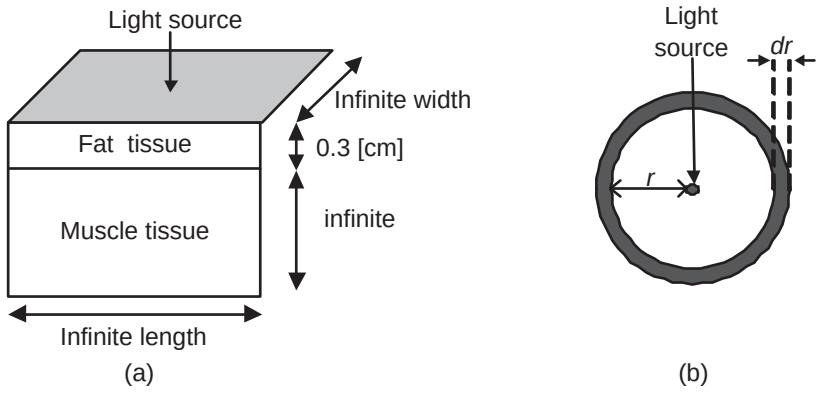

Figure 5.1 a) Two layered fat-muscle heterogeneous tissue model used in the Monte Carlo simulations b) Top view of light source and the ring of interest

In the simulations, absorption coefficients of both fat and muscle layers were made to change simultaneously. However change of absorption coefficient in muscle layer was made much bigger than in fat layer. Because it has been shown that fat layer has less oxygen consumption (0.01-0.03 in Coppack et al. [121], 0.04 ± 0.01 ml.min^{-1}.100g^{-1} in Simonsen et al. [122]) compared to muscle tissue (0.12-0.19 ml.min^{-1}.100g^{-1} in Coppack et al. [121]) at rest. In the presence of enough oxygen, substrates and at moderate level exercises, oxygen consumption for muscle increases [123].

For single layer assumption and 1-detector based calculations of absorption changes, Eq. 5.3 is used. For two-detector based calculations, Eq. 5.7 and 5.8 are used.

5.3 Results and Discussion

In the simulations, resting level absorption coefficients are 0.02 [cm^{-1}] and 0.2 [cm^{-1}] for fat and muscle layers, respectively. Reduced scattering coefficients are 12 [cm^{-1}] for fat layer and 6 [cm^{-1}] for muscle layer. In the first simulation change of absorption coefficient in fat layer is 4 times less than change in muscle layer. In the second simulation case, change of absorption coefficient muscle layer is made 16 times greater than change in fat layer. Results are shown in Tables 5.1, 5.2 and Figures 5.2,

Table 5.1
Found changes of absorption coefficients using 1-detector and 2-detectors for simulated absorption changes in fat and muscle layers. Change of absorption coefficient in muscle layer is 4 times bigger than change in fat layer.

Real		Error of			
$\triangle\mu_{a,fat}$ [cm^{-1}]	$\triangle\mu_{a,muscle}$ [cm^{-1}]	$\triangle\mu_{a,1-d}$ ($r = 1$ [cm]) %	$\triangle\mu_{a,1-d}$ ($r = 4$ [cm]) %	$\triangle\mu_{a,2-d}$, 1^{st} layer ($r = 1$ & 4 [cm]) %	$\triangle\mu_{a,2-d}$, 2^{nd} layer ($r = 1$ & 4 [cm]) %
-0.020	-0.08	145.9	-9.5	12.3	11.7
-0.015	-0.06	138.3	-12.3	8.8	8.2
-0.010	-0.04	131.5	-14.8	5.7	5.2
-0.005	-0.02	125.4	-17.0	2.7	2.4
0.005	0.02	114.7	-20.8	-2.6	-2.2
0.010	0.04	110.0	-22.5	-5.0	-4.3
0.015	0.06	105.7	-24.1	-7.2	-6.1
0.020	0.08	101.6	-25.5	-9.3	-7.9

5.3. In the tables, first and second columns give the actual absorption changes in fat and muscle layers. Third and fourth columns give percentage errors for the absorption changes found using the modified Beer-Lambert law with 1-detector (called $\triangle\mu_{a,1-d}$). Detector at 1 [cm] is used for fat layer and at 4 [cm] is used for muscle layer absorption coefficient change estimations. Errors are calculated relative to real absorption changes (i.e. error for fat calculation is equal to $100 \times (\triangle\mu_{a,1-d@r=1} - \triangle\mu_{a,fat})/\triangle\mu_{a,fat}$. Error results of two-detector based calculations using Eq. 5.7 and 5.8 are given in fifth and sixth columns, denoted as $\triangle\mu_{a,2-d}$. Detectors at 1 and 4 [cm] are used for two-detector based calculations. First layer and second layer estimations are used for fat and muscle layer absorption changes.

For $\triangle\mu_{a,1-d}$, results are close to that of fat layer's change for r = 1 [cm] and to muscle layer's change for r = 4 [cm]. For fat layer, estimates are bigger than 100% in the first simulation set and higher than 500% in the second simulation set. For muscle

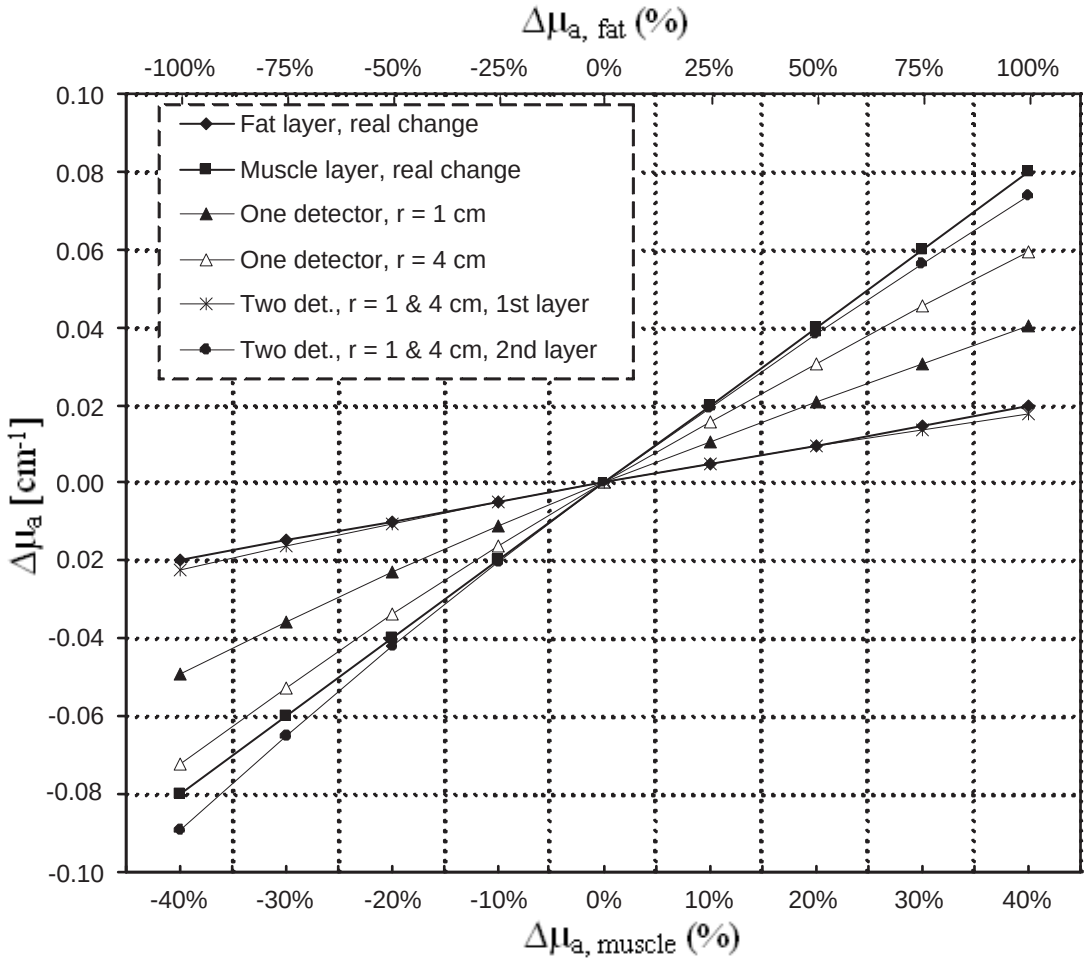

Figure 5.2 a) Found absorption changes with 1-detector (r = 1 [cm] or r = 4 [cm]) and 2-detectors (r = 1 [cm] and r = 4 [cm]) for simulated absorption changes in fat and muscle layers. Change of absorption coefficient in muscle layer is 4 times bigger than change in fat layer.

layer, estimates are better, error is between 9.5-25.5% for the first simulation set and between 14.2-30.3% the for the second simulation set. It is noted that errors are lower for absorption coefficients' decrement but higher for their increment for 1-detector based calculations.

For 2-detector partial pathlength based method, estimates are better than the 1-detector based modified Beer-Lambert law estimates in all cases simulated. Especially fat layer estimates are better; absolute errors are between 2.7-12.3% for the first simulation set and between 8.4-30.5% for the second simulation set. Muscle absorption estimates are very good especially for small changes in absorption coefficients. Absolute errors are between 2.2-11.7% and between 2.3-11.9% for the first simulation set and second simulation set, respectively. For up to 30% and 75% absorption coefficient

Table 5.2
Found changes of absorption coefficients using 1-detector and 2-detectors for simulated absorption changes in fat and muscle layers. Change of absorption coefficient in muscle layer is 16 times bigger than change in fat layer.

Real		Error of			
$\triangle\mu_{a,fat}$ [cm^{-1}]	$\triangle\mu_{a,muscle}$ [cm^{-1}]	$\triangle\mu_{a,1-d}$ ($r = 1$ [cm]) %	$\triangle\mu_{a,1-d}$ ($r = 4$ [cm]) %	$\triangle\mu_{a,2-d}$, 1^{st} layer ($r = 1$ & 4 [cm]) %	$\triangle\mu_{a,2-d}$, 2^{nd} layer ($r = 1$ & 4 [cm]) %
-0.00500	-0.08	699.2	-14.2	39.9	11.9
-0.00375	-0.06	670.0	-17.1	28.9	8.4
-0.00250	-0.04	643.9	-19.5	18.6	5.3
-0.00125	-0.02	620.4	-21.8	9.0	2.5
0.00125	0.02	579.4	-25.6	-8.4	-2.3
0.00250	0.04	561.3	-27.3	-16.2	-4.4
0.00375	0.06	544.6	-28.9	-23.6	-6.3
0.00500	0.08	528.9	-30.3	-30.5	-8.1

changes in muscle and fat layers, error is less than 8.2% for muscle absorption coefficient change estimate in the first simulation set. In the second simulation set, absolute error is less than 8.4% for up to 30% and 18.75% absorption coefficient changes in muscle and fat layers.

Results for the methods with erroneous assumption from true mean and partial path lengths are given in the Tables 5.3 and 5.4 for ±15% deviations from real path-lengths and in the Figures 5.4, 5.5, 5.6 and 5.7 for ±5%, 10% and 15% deviations. The erroneous use is assumed with same percentages for all $< L^r_{fat} >$, $< L^r_{muscle} >$ for the 2-detector system and mean path length for the 1-detector system. 1-detector system is directly affected by this such that overestimation of mean path length reduces error of $\triangle\mu_{a,fat}$ while it increases underestimation error of $\triangle\mu_{a,muscle}$. This is because of the fact that we take both real absorption changes in fat and muscle layer simultaneously with $\triangle\mu_{a,fat}$ much less than $\triangle\mu_{a,muscle}$. Error increase for $\triangle\mu_{a,muscle}$ is evident

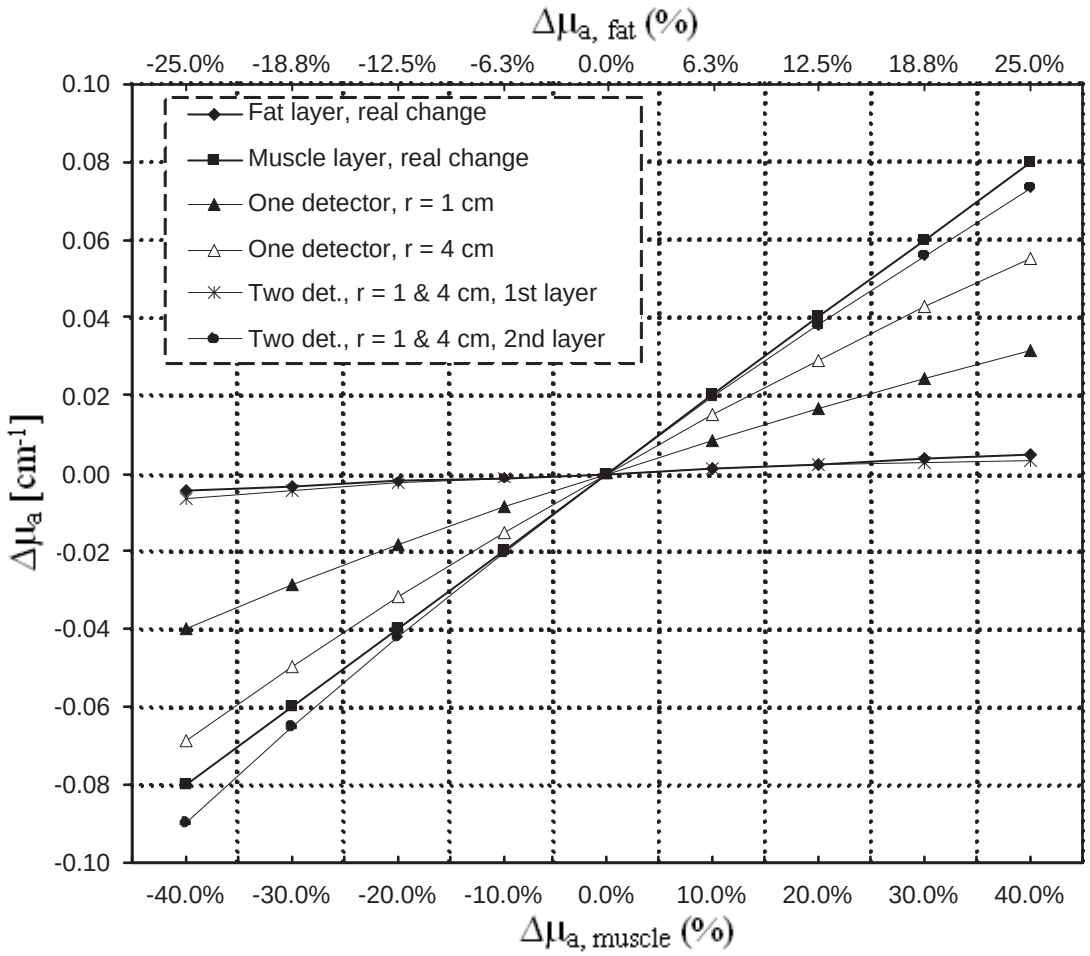

Figure 5.3 a) Found absorption changes with 1-detector (r = 1 [cm] or r = 4 [cm]) and 2-detectors (r = 1 [cm] and r = 4 [cm]) for simulated absorption changes in fat and muscle layers. Change of absorption coefficient in muscle layer is 16 times bigger than change in fat layer.

since pathlength overestimation increases the underestimation error. 1-detector system with detector at 1-cm distance is affected by $\triangle\mu_{a,muscle}$ and path length overestimation reduces estimation of absorption change, which makes it closer to the absorption change of fat layer. The underestimation error of muscle layer increases with deviation from real partial path lengths (both increase and decrease of the used values from real partial path lengths increase the error). Taking -15% higher partial path lengths is so low that it result in overestimation for $\triangle\mu_{a,muscle}$ while +15% higher partial path lengths give usual underestimation errors. The estimation error of $\triangle\mu_{a,fat}$ is a complex function of the direction of real $\triangle\mu_{a,fat}$ and used partial path lengths. Moreover there is nonlinearity in the estimation which is evident in Figure 5.6.

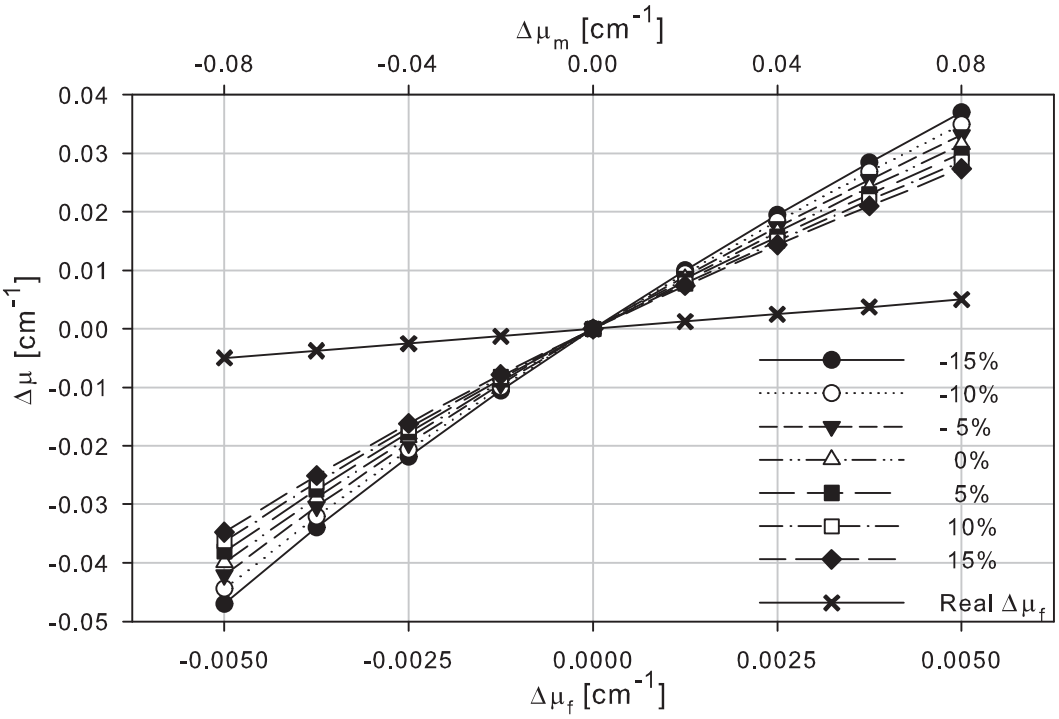

Figure 5.4 Results for 1-detector (r = 1 [cm]) with erroneous assumption of mean path lengths. Simulated change of absorption coefficient in muscle layer is 16 times bigger than change in fat layer.

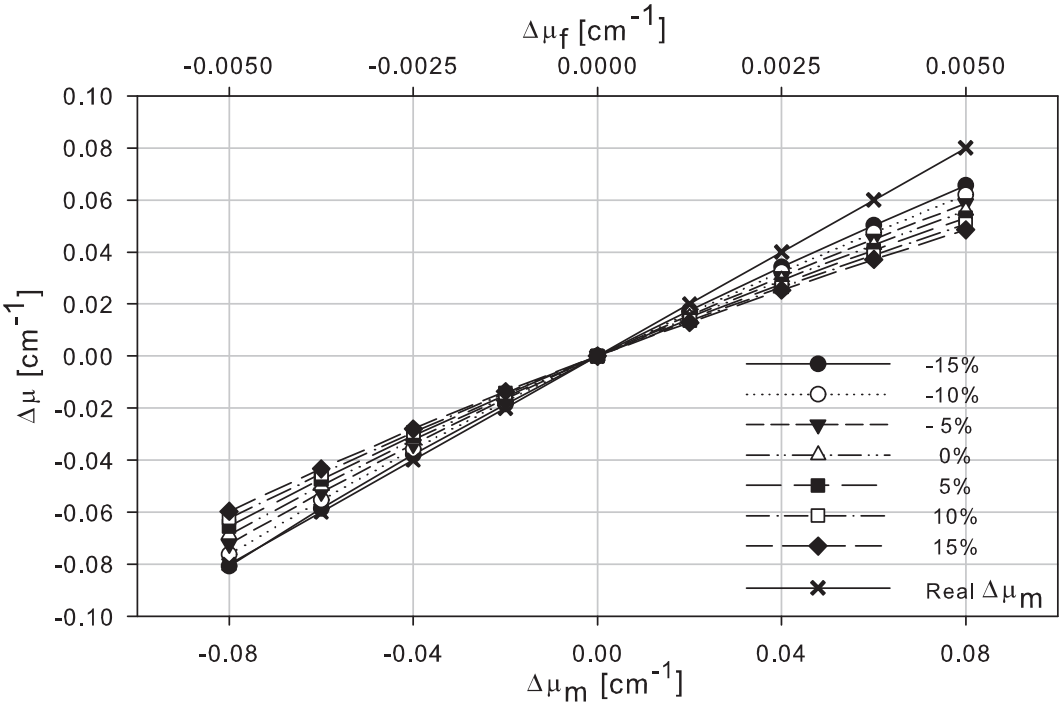

Figure 5.5 Results for 1-detector (r = 4 [cm]) with erroneous assumption of mean path lengths. Simulated change of absorption coefficient in muscle layer is 16 times bigger than change in fat layer.

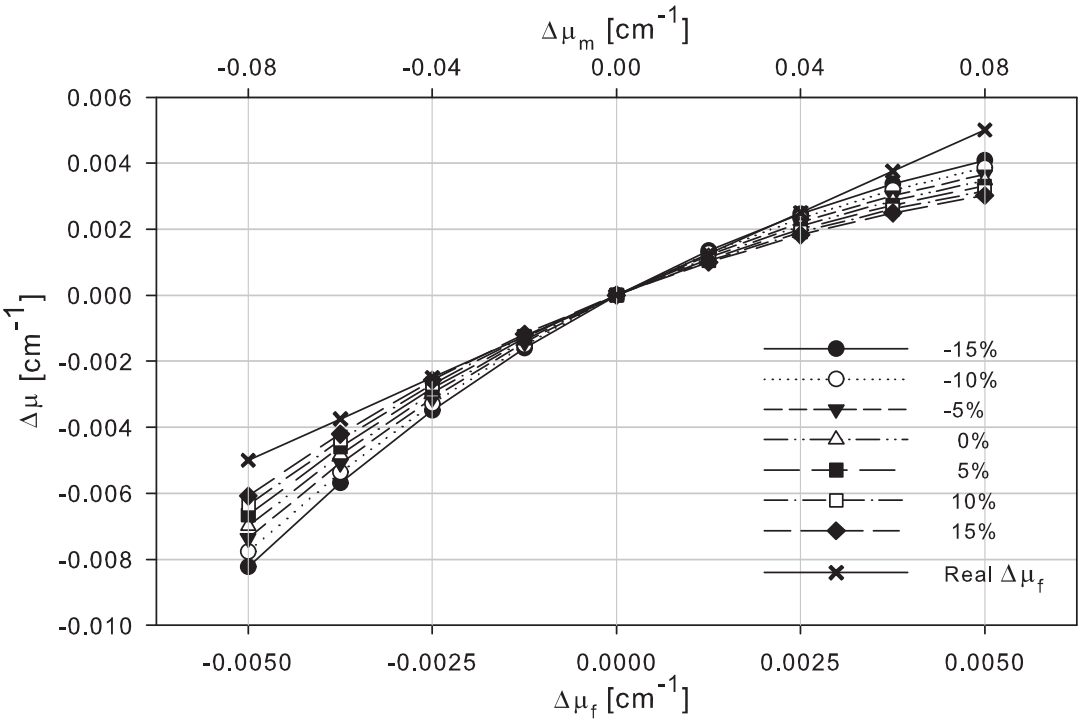

Figure 5.6 Results for 2-detector of $\triangle\mu_{a,fat}$ with erroneous assumption of mean partial path lengths. Simulated change of absorption coefficient in muscle layer is 16 times bigger than change in fat layer.

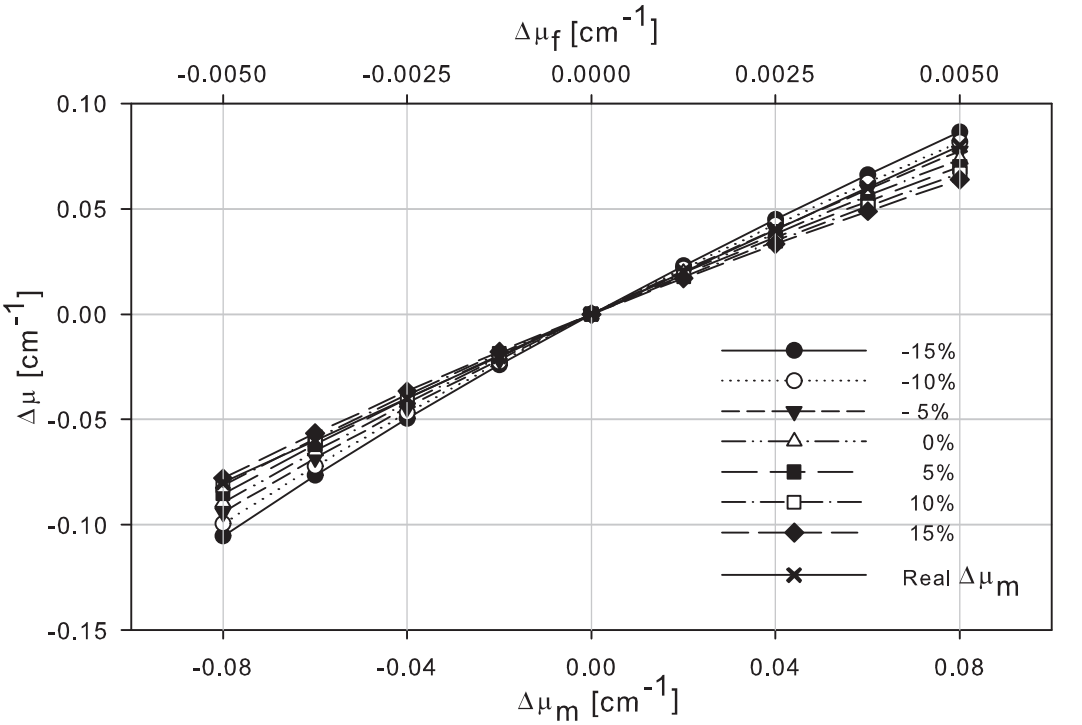

Figure 5.7 Results for 2-detector of $\triangle\mu_{a,muscle}$ with erroneous assumption of mean partial path lengths. Simulated change of absorption coefficient in muscle layer is 16 times bigger than change in fat layer.

Table 5.3
Found changes of absorption coefficients using 1-detector with -15% erroneous assumption of mean and partial path lengths. Change of absorption coefficient in muscle layer is 16 times bigger than change in fat layer.

Real		Error of			
$\triangle\mu_{a,fat}$ [cm^{-1}]	$\triangle\mu_{a,muscle}$ [cm^{-1}]	$\triangle\mu_{a,1-d}$ ($r = 1$ [cm]) %	$\triangle\mu_{a,1-d}$ ($r = 4$ [cm]) %	$\triangle\mu_{a,2-d}$, 1^{st} layer ($r = 1$ & 4 [cm]) %	$\triangle\mu_{a,2-d}$, 2^{nd} layer ($r = 1$ & 4 [cm]) %
-0.00500	-0.08	840.3	0.9	64.6	31.7
-0.00375	-0.06	805.9	-2.4	51.6	27.5
-0.00250	-0.04	775.2	-5.3	39.5	23.9
-0.00125	-0.02	747.6	-8.0	28.2	20.6
0.00125	0.02	699.3	-12.5	7.8	15.0
0.00250	0.04	678.0	-14.5	-1.5	12.5
0.00375	0.06	658.3	-16.3	-10.1	10.2
0.00500	0.08	639.9	-18.0	-18.3	8.1

5.4 Conclusion

It has been found that for 2-detector partial pathlength based method, estimates are better than the 1-detector based modified Beer-Lambert law estimates in all cases simulated. It should be noted that partial pathlengths are used in 2-detector partial pathlength based method while mean pathlength is used for 1-detector based modified Beer-Lambert law estimates. Assumption of homogeneous single-layered medium leads to higher error [79, 77, 76, 100, 100, 105]. It is also interesting that proposed method leads to accurate results for fat layer absorption coefficient change estimates even using distant detectors 1 cm and 4 cm. In practice, getting accurate initial (resting level) optical properties of the medium and obtaining accurate partial pathlengths poses a problem for the proposed technique.

Table 5.4
Found changes of absorption coefficients using 1-detector with +15% erroneous assumpion of mean and partial path lengths. Change of absorption coefficient in muscle layer is 16 times bigger than change in fat layer.

Real		Error of			
$\triangle\mu_{a,fat}$ [cm^{-1}]	$\triangle\mu_{a,muscle}$ [cm^{-1}]	$\triangle\mu_{a,1-d}$ ($r = 1$ [cm]) %	$\triangle\mu_{a,1-d}$ ($r = 4$ [cm]) %	$\triangle\mu_{a,2-d}$, 1^{st} layer ($r = 1$ & 4 [cm]) %	$\triangle\mu_{a,2-d}$, 2^{nd} layer ($r = 1$ & 4 [cm]) %
-0.00500	-0.08	595.0	-25.4	21.6	-2.7
-0.00375	-0.06	569.6	-27.9	12.1	-5.7
-0.00250	-0.04	546.9	-30.0	3.1	-8.5
-0.00125	-0.02	526.5	-32.0	-5.2	-10.9
0.00125	0.02	490.8	-35.3	-20.3	-15.0
0.00250	0.04	475.1	-36.8	-27.2	-16.8
0.00375	0.06	460.5	-38.1	-33.6	-18.5
0.00500	0.08	446.9	-39.4	-39.6	-20.1

6. MUSCLE MEASUREMENTS FOR ENDURANCE AND FATIGUE INVESTIGATION

6.1 Basic Skeletal Muscle Physiology

Muscles are perfect 'machines' which convert chemical energy into mechanical energy. Skeletal muscle, cardiac muscle and smooth muscle are the three types of muscle tissue in the human body. Skeletal muscles are attached mostly to the bones, giving us the ability to control the body movement *voluntarily*. Cardiac muscle is found in only our heart which functions as a pump in the circulatory system. The main muscles of internal organs and tubes (i.e. urinary bladder, stomach, blood vessels) is smooth muscle which has the role of material movement. Although we have voluntary control over on skeletal muscles, conscious control over smooth and cardiac muscles can be learned to some extent. Skeletal muscles and cardiac muscles have light and dark bands under light microscope, which caused them to be called *striated muscles*. Smooth muscles lack such appearance [123].

Skeletal muscle comprises the largest single organ of the body. Up to 40% of our body's mass is composed of skeletal muscles. Skeletal muscles are highly compartmentalized, and each compartment is considered as a separate entity (i.e. biceps muscle). Single cells or fibers are the building elements -constituent cells- of muscles embedded in a matrix of collagen. Muscles are connected to the bones by tendons -formed by collagen matrix- at the both ends. Like other cells, each muscle cell has cell membrane (called sarcolemma). They contain mitochondria for the oxidative metabolism and organelles necessary for protein synthesis. Skeletal muscle fibers can be as long as two centimeters long. Actin and myosin molecules in the muscle fiber generate contraction hence force production. These molecules can slide across each other. Myosin (*thick*) filaments associate with the actin (*thin*) filaments by crossbridges. According to sliding filament theory of contraction, overlapping filaments slide past each other leading to muscle contraction and tension generated is proportional to the interaction between

these filaments. A single contraction-relaxation cycle is called a twitch. Three types of skeletal muscle fibers exist in the muscles which differ in their contraction speed and fatigue resistance. These are fast-twitch glycolytic fibers, fast-twitch oxidative fibers and slow-twitch oxidative fibers. Fast-twitch fibers have quicker twitch times allowing fast and precise movements whereas slow-twitch fibers are suited for prolonged and powerful movements (i.e. maintaining posture) [123, 124].

Each fiber in muscle is innervated by a single axon, and multiple muscle fibers are controlled by the axons of one somatic motor neuron. This motor neuron and muscle fibers it controls are called motor unit, which is the elementary unit of contraction. As the force muscle produces increases, more motor units are recruited (and their firing frequency is increased) which is controlled by nervous system [123, 124].

6.1.1 Energy Metabolism in the Muscles

Muscles require continuous supply of energy because of the mechanical force they generate. At the initial phase of work, muscles may use ATP within the muscle which is sufficient for just 8 twitches (initially stored ATP and PCr can support only 15 seconds of intense exercise). Afterwards they must use metabolism to generate ATP.

As a source of energy, carbohydrates, especially glucose, are the fastest and efficient sources. Glucose is broken down to pyruvate by glycolysis process (anaerobic respiration). If there is adequate supply of oxygen, pyruvate goes into citric acid cycle, producing about 30 ATP per molecule of glucose (called aerobic respiration & oxidative phosphorylation). Muscles obtain energy also from fatty acids. Fatty acid breakdown happens always in the presence of oxygen because fatty acid utilization is through aerobic energy mechanism. Because of this fatty acids are used mostly in resting and light exercise. During heavy exercise, generation of ATP using fatty acids is not used heavily since conversion of fatty acids to acetyl CoA (beta-oxidation) is a slow process. At 70% of maximum exercise intensity, glucose is the dominant energy source [123]. Energy conversion efficiency of aerobic respiration is 40% (30-32 ATP

are produced per glucose molecule), much higher than that for anaerobic metabolism which metabolizes glucose down to lactic acid. However, ATP generation speed of anaerobic metabolism is 2.5 times faster with the price of much lower efficiency (about 2 ATP generation compared to 30-32 ATP per glucose) and higher acidosis because of CO_2 and lactic acid accumulation. Oxidative phosphorylation can be sustained for hours in the presence of enough metabolites which depends on exercise intensity [125] and fitness of the person. When there is problem with the supply of oxygen, energy production mechanism switches to glycolysis for ATP synthesis, and this can not be maintained too long (about 1 minute at maximal exercise). Proteins are not utilized for energy production in the muscle cells.

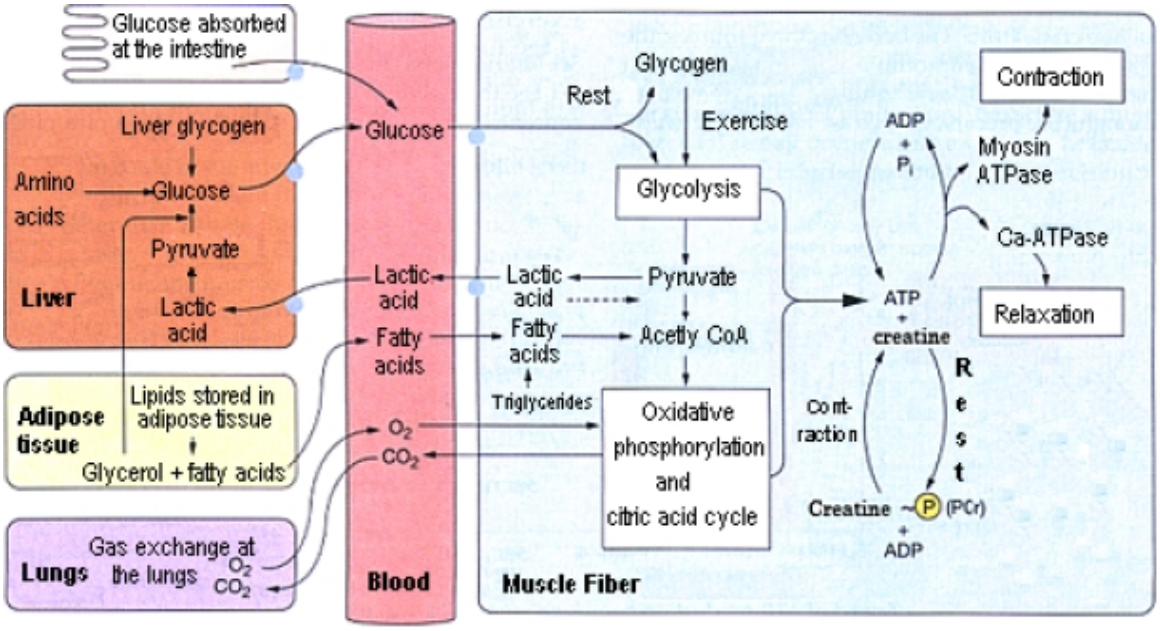

Figure 6.1 Energy metabolism in skeletal muscle from Silverthon [120]

Differences in the energy metabolism of different skeletal muscle fibers exist. The fiber types are fast-twitch (type I) and slow-twitch (type II) fibers. Fast-twitch fibers are divided into fast-oxidative, fast-glycolytic fibers. Fast-twitch glycolytic fibers are the largest in diameter and their primary mechanism for ATP generation is anaerobic metabolism and they have the fastest fatigue development. Slow-twitch fibers use mainly oxidative metabolism for ATP generation. Slow-twitch oxidative fibers have more vessels and capillaries, have high myoglobin content and a smaller diameter all of which allows oxygen to be passed easily from interstitial fluid to the mitochondria. These make it easy for slow-twitch fibers to maintain oxidative phosphorylation and

they are more resistant to fatigue. Fast-twitch oxidative fibers are smaller than fast-twitch glycolytic fibers, contain some myoglobin and use both glycolytic and oxidative phosphorylation to generate ATP which makes them more resistant to fatigue than fast-twitch glycolytic fibers [125].

6.1.2 Effects of Exercise on Human Physiology

Exercise is a demanding process for the body. It disrupts homeostasis while generating force, movement and heat. During exercise demands for ATP, O_2 and nutrients such as fatty acids and glucose (which are required as energy sources) should be supplied while waste products such as CO_2 and lactic acid should be cleared away.

During exercise, ventilation increases in response to higher O_2 demand and to clear increased CO_2 in the blood. The most (70-80%) of the CO_2 is in the form of bicarbonate and 5-10% is dissolved in the plasma and the rest is bound to hemoglobin. Hyperventilation increases with the onset of exercise (i.e. prior to blood concentration increase of $[CO_2]$ or pH level decrease), it is hypothesized that this initial increase in the ventilation is caused by the sensory input from the muscle mechano-receptors combined with parallel descending pathways from the motor cortex [125]. In fact, the arterial O_2 and CO_2 partial pressures as well as pH level do not change significantly during mild to moderate exercise.

Cardiac output, defined as the product of cardiac rate and stroke volume, is also increased during exercise. SA (sinoatrial) node rate is increased by the decreased parasympathetic activity at the start of the exercise and increased sympathetic stimulation. Sympathetic stimulation also increase contractility of the heart muscles which leads to increased stroke volume. Increased heart rate prevents heart muscle fiber damage from overfilling of the ventricles by reducing the fill time of the heart. Venous return of the blood is increased by muscle contractions along with inspiratory movements. Cardiac system performance is the limiting major factor in exercise since ventilation reaches about 65% of its highest capacity while cardiac output goes up to

90% of its highest [125].

As exercise begins, cardiac output which equals 5-6 l/min at rest can increase up to about 40 l/min in trained athletes during maximal exercise [126]. In the resting state 21% of cardiac output goes to skeletal muscles while at the exercise it increases up to 88%. Peripheral resistance to blood flow decreases during exercise. Despite this, Mean Arterial Blood Pressure (MABP) increases because of proportionally higher increase in cardiac output. Baroreceptor reflex is offset which would normally try to compensate this increase (i.e. by decreasing it). One theory is that arterial baroreceptor threshold is increased to a higher threshold, other one is that baroreceptor afferent neurons blocked in the spinal cord by the presynaptic inhibition. Another one is that chemoreceptors sensitive to pH levels or metabolites signal to the central nervous system that blood flow is not adequate and this signal overrides baroreceptor reflex [125].

Glucagon, cortisol, catecholamines (epinephrine & norepinephrine) and growth hormone levels in the plasma increase throughout exercise. Growth hormone, cortisol and the catecholamines increase the glycerol and fatty acids by breakdown triglycerides while glucagon, catecholamines and cortisol increase lead to plasma glucose increase by invoking the liver to breakdown the glycogen. Although plasma glucose level increases, insulin secretion decrease which leaves more glucose available to muscle cells which do not need insulin for taking glucose into the cells [125]. Fat and glycogen stores as well as activity of β-oxidation enzymes (which breakdowns fatty acids) are increased in the muscle fibers induced by exercise training [127, 125].

6.2 Muscle Fatigue and Endurance

Muscle fatigue is still a poorly understood phenomena albeit our familiarity with itself in our daily life, sports and clinical settings [128]. In broad terms, decrease in performance can be called fatigue [129]. One of the definitions of fatigue is decline in the maximal force generating capacity or maximal power. Another definition is for submaximal contractions where the aim is to produce a desired target force level and

fatigue occurs at the failure of this goal. Time duration until fatigue in this second definition is used for muscle endurance measurements.

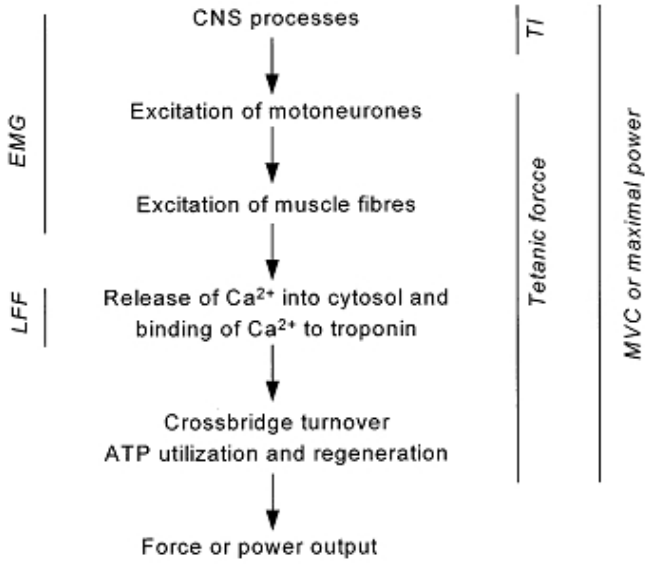

Figure 6.2 Used methods in fatigue investigations from Voellestad [125]. LFF is low frequency fatigue, TI is twitch interpolation

In the Figure 6.2 from Voellestad [128], processes leading to force production is given. CNS includes motivation and related psychological drive as well as sensory information. Different types of motor units have different thresholds for contraction and have different conduction velocities. Besides energetic characteristics are not the same. During contraction, different/increasing number of motor units can be in action depending on the recruitment pattern with these mentioned different properties. As the force production continues, ions' balances around the sarcolemma change, metabolic by-products increase, ATP reserves and ATP regeneration rate may decrease, O_2 and energy supply could be hindered by blood flow occlusion because of increased intramuscular pressure, pH levels could decrease, Ca^{2+} release from sarcoplasmic reticulum could decrease, affinity of troponin to Ca^{2+} could decrease all leading to impairment of propagation of action potential. The problem in understanding fatigue is that any one of these factors in the chain can be a limiting factor in force/power production of the muscle. It is a challenging task to isolate a single step in this process chain, especially on humans [128].

The technical methods available to researchers for studying underlying physiological changes of fatigue range from blood measurements, electrocardiography, inhaled-exhaled gas analyzer, magnetic resonance spectroscopy and imaging, surface and needle electromyography, near-infrared spectroscopy to isometric-isokinetic-dynamic exercise sets which provide force-torque-power measurements.

6.3 Surface EMG

Although surface EMG (SEMG) is still not widely used for clinical analysis purposes, it is a widely known and used analysis in muscle endurance and fatigue research studies. SEMG is basically measurement of the electrical signal when a muscle is active. This signal is the temporal and positional summation of muscle fiber action potentials triggered by the central nervous system. The most known parameters are SEMG signal amplitude related parameters (i.e. root mean square signal), mean frequency and median frequency which are all computed for time windows that are typically 0.2-2.0 seconds.

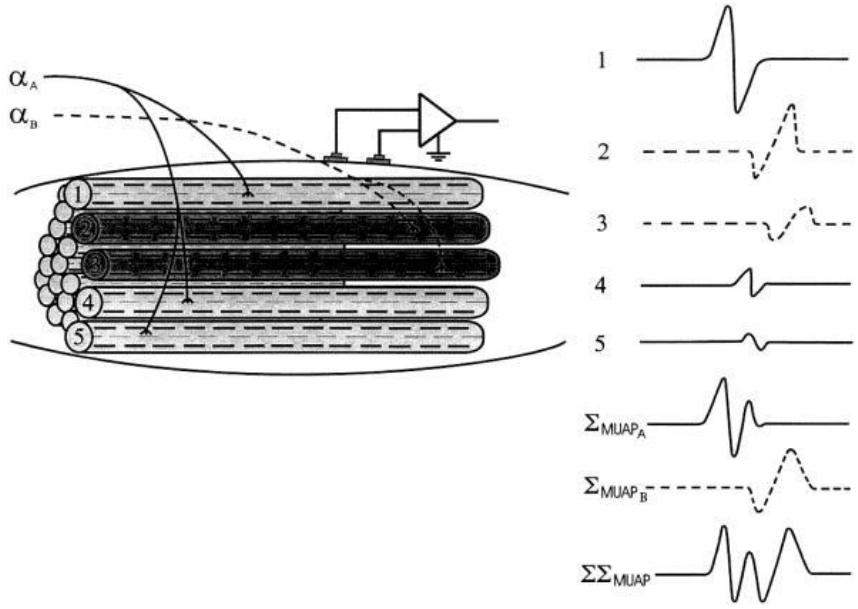

Figure 6.3 Formation of the motor unit action potentials of two motor units and sum of these two at the surface detector, from Kamen and Caldwell [127]

Motor units are the basic units in skeletal muscle organization. They consist of a single motoneuron (alpha motor neuron) and skeletal fibers that it innervates. A single motor unit can have 3 - 2000 muscle fibers. Fine controlled movements are controlled by motor units having small number of motor fibres, i.e. less than 10. Those motor units responsible for gross movements can have 100 - 1000 fibers. When a motoneuron is activated, it triggers all the muscle fibers it innervates. Depolarization are spread on the membranes of the all muscle fibers of the motor unit. For a motor unit, the motor unit potential is defined as the temporal and spatial summation of the muscle action potentials for all the fibers of the particular motor unit. Figures 6.3 and 6.4 illustrate sEMG formation from Kamen and Caldwell [130] and Basmajian and DeLuca [131], respectively.

Single motor unit activity can be measured by a needle electrode but it is very inconvenient for the patient. SEMG is measured with surface electrodes placed on the skin. Hence surface EMG is the summation of the all active motor unit potentials within the measured volume [130, 132, 133].

Although SEMG is thought to give more global MU activity related information, its amplitude and power spectrum properties are affected by the muscle fiber membrane properties along with MU action potentials' timings (impulse trains). Hence this signal contains valuable information about central nervous system, peripheral nerve-muscle system and related physiological processes [134].

A MATLAB [135] program has been developed for ease of SEMG analysis, EMGALY.1.2, given in appendix B. The software has been developed to assist researchers probing this signal for basic variables' investigations. The software has been developed in MATLAB environment for upgrade easiness and for the ease of the user a graphical user interface has been provided for execution of all commands. In its current form software use has been maximized for studies using isometric exercise protocols and enables investigation of the basic variables like root mean square, mean frequency and median frequency. Time range for data investigation can be selected by the user and this selected range can be divided up to 20 segments for analysis.

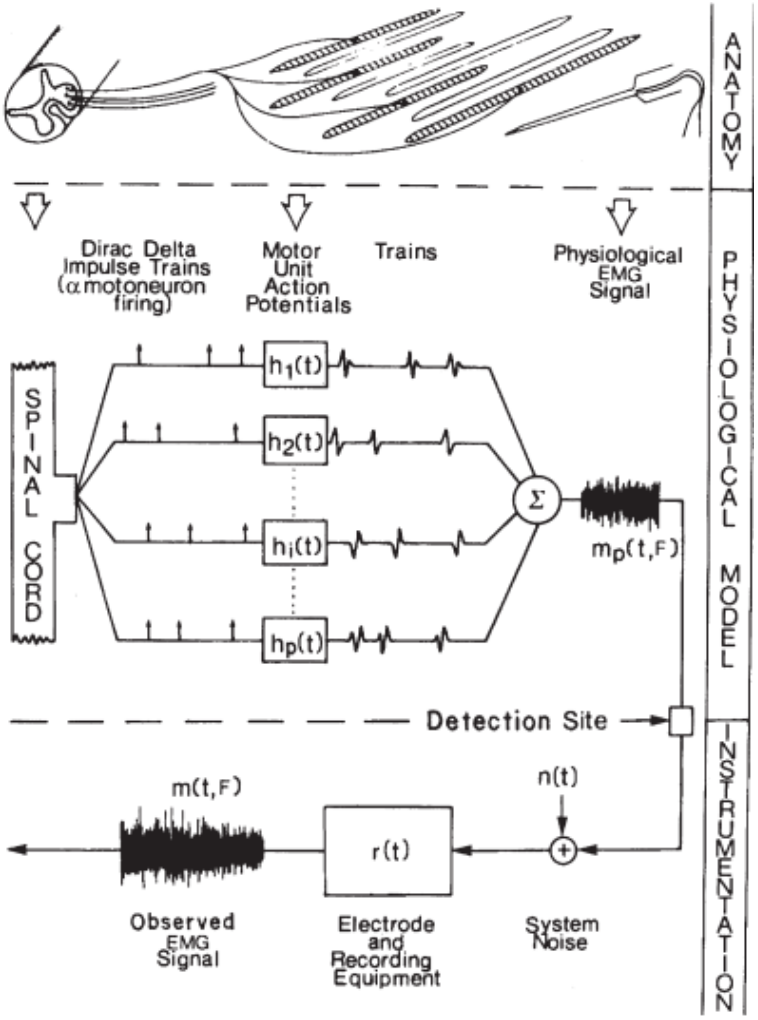

Figure 6.4 Measured SEMG signal composition and formation from Basmajian and DeLuca [128]

6.4 Ischemia Measurements

Ischemia protocols are used to investigate vascular dynamics after ischemia. It was especially used in the early times of NIRS development to show ability of the device to show Hb increase and HbO_2 decline. Since cw-NIRS technique can not give absolute values because of the DPF value information unavailability, 5 to 6 minutes arterial occlusion at the start of an experiment was done in some cw-NIRS studies to get a scaling between subjects and for calibration, i.e. change of HbO_2 during ischemia is taken as 100% range. Hence the experiments done after this scaling can be compared among subjects [27].

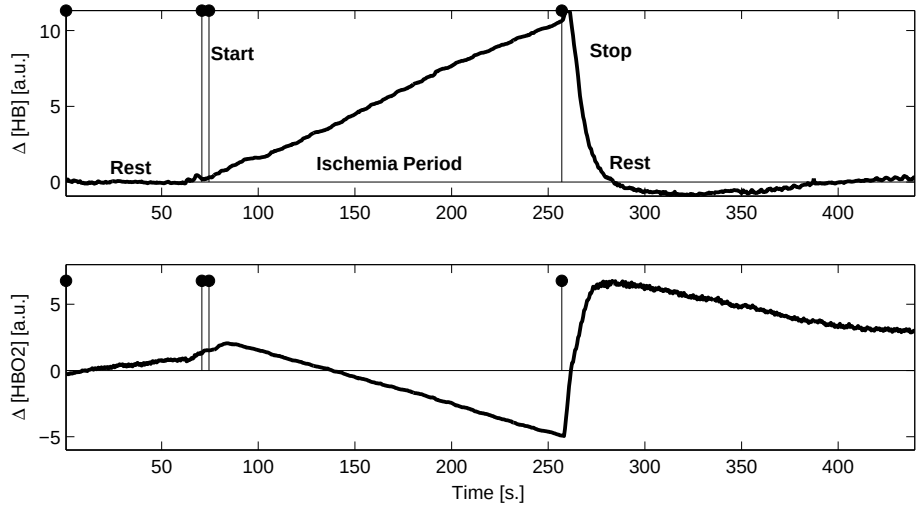

Figure 6.5 Typical trends of Δ[Hb] and Δ[HbO_2] in ischemia protocol

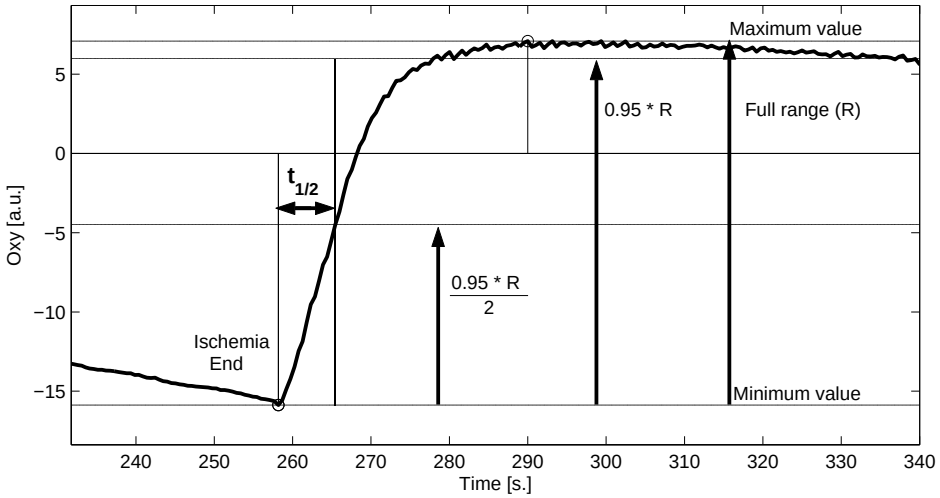

Figure 6.6 Illustration of half time parameter calculation for a typical *oxy* signal for the Δ[Hb] and Δ[HbO_2] given in the Figure 6.5

Ischemia protocol is important in terms of validating the validity of NIRS measurements and deriving useful parameters. In a typical ischemia measurement, during ischemia [Hb] increases (and reaching maximum value) while [HbO_2] and *oxy* signal ($\triangle$[HbO_2] - $\triangle$[Hb]) decrease (reaching minimum values). Immediately after the ischemia (by lowering the cuff pressure to 0 mmHg), [Hb] decreases sharply, [HbO_2] and *oxy* signal increase (Figure 6.5). These rapid responses are followed by trends returning to the baselines. The concentration difference immediately after ischemia is called range (R) and the time to reach half of this range (or half of R$\times$0.95) after ischemia

is called half time ($t_{1/2}$) [44] which gives information about the recovery speed of the probed muscle tissue investigated. The computation of half time parameter is shown in Figure 6.6. This parameter is quite often used in NIRS measurements since it alleviates the problem of quantifying changes in HbO_2 and gives ability to monitor the recovery process.

De Blasi *et al.* (1992) [136] were the one of the first group who did ischemia measurements in the forearm using NIRS. The authors found decreasing ($\triangle[HbO_2]-\triangle[Hb]$) and not changing (within some limits) ($\triangle[HbO_2]+\triangle[Hb]$) signal during ischemia. Cuff relase was accompanied by rapid recovery of ($\triangle[HbO_2] - \triangle[Hb]$) signal. In another protocol, subjects performed 15 seconds isometric MVC contraction during ischemia. Interestingly total deoxygenation was lower in magnitude in this protocol.

The problem with this protocol is that subjects are uncomfortable with this protocol and it is painful. Assuring arterial occlusion could require checking of arterial pulse and very high pressures could cause problems for the subjects.

6.4.1 Usage of Recovery Times

In the first study conducted in coordination with 'Spor Hekimliği Bölümü, İstanbul Üniversitesi', NIRS measurements are taken from sportsmen before and after they participate a major sports event in Kaşıkçıoğlu et al [137]. In this study NIRS device is used to study the hemodynamics of forearm tissue after prolonged exercise along with cardiac dynamics. In the experiment, ischemia protocol is used. In the experiment, the probe is placed on the subjects' lower half of left forearm near the wrist and arterial blood flow is restricted by placing a tourniquet on the upper arm at a pressure of 250 mmHg after a 1 minute baseline measurement. After 5 minutes of ischemia, tourniquet pressure is released and afterwards 4 minutes of measurement is taken. Ischemia measurements are taken first before the marathon/triathlon with this protocol. After the marathon/triathlon, sportsmen took the effort test and after it ischemia measurements are taken again. Change of concentration value range between minimum point and

maximum point is taken as full range and time to reach half of the 95% of the full range from the end of ischemia is calculated as half-time value ($t_{1/2}$). Mean half time values were calculated across the available light detectors' signals for each subject for $\triangle$[Hb], $\triangle$[HbO_2] and *oxy* ($\triangle$[HbO_2]- $\triangle$[Hb]) signals. Increase in the mean of $t_{1/2,oxy}$ and $t_{1/2,HbO2}$ after marathon/triathlon and effort test were dominant findings in the results although statistically not important. This could mean that arterial system is affected much more by the prolonged exercise. Increase of standard deviation of $t_{1/2,oxy}$ and $t_{1/2,HbO_2}$ for the majority of the subjects after prolonged exercise could indicate heterogeneity of the vascular system dynamics after big effort.

A MATLAB program has been developed (some parts in GUI form) to calculate recovery time parameters with and this tool has been used in the studies of Dinler et al. [138, 139] in fibromyalgia patients towards better understanding of this disease. In this study, half time recovery times in ischemia protocol of the patients were used as a parameter to search for the effect of aerobic exercise training often advised to fibromyalgia patients as a treatment. Same methodology was applied as in Kaşıkçıoğlu et al. [137]. Preliminary results which compare cw-NIRS derived half time recovery times of Hb, HbO_2 and *oxy* parameters of ischemia protocol measurements along with pulmonary kinetics determined oxygen consumption, heart rate and rate of perceived exertion parameters of standard Bruce multistage maximal treadmill protocol with metabolic measurements between patients and control group has been investigated in the study of Dinler et al. [138]. Mean $t_{1/2}$ for Hb, $t_{1/2}$ for HbO_2 and $t_{1/2}$ for *oxy* values were longer in fibbromyalgia group than those of the control group (24.3, 9.8 and 25.4%, respectively). Furthermore, there was an inverse correlation between peak oxygen consumption of pulmonary kinetics and $t_{1/2}$ for *oxy* ($r = -0.48$, $P < 0.05$). Final form of this study was also published in the same journal in 2009 [139].

6.5 Hand Grip Exercise

A joint muscle exercise study was conducted with Marmara University, 'Beden Eğitimi ve Spor Yüksek Okulu'. In this study, hand grip protocol was used. Three

different measurement modalities were used, sEMG, cw-NIRS and hand grip force measurement. The study aimed at investigation of physiological processes underlying muscle endurance and fatigue. The motivations and aims behind this study were as follows;

- Obtaining the simultaneous signals of Δ[Hb], Δ[HbO_2], oxy, force and sEMG for isometric and isotonic hand grip exercise at different force levels.
- Calculation of sEMG related parameters (RMS, MNF, MDF) and cw-NIRS parameters (amplitude parameters and duration to inflection point)
- Inspired by the previous studies in the literature, finding the inflection points of cw-NIRS parameters at which point initial fast change phase changes to slow phase. The relationship between inflection durations and other parameters (i.e. exercise duration, sEMG parameters of MNF, MDF etc.) will be examined.
- Investigation of the obtained parameters' changes and relationships between them
- By performing these previous items, investigating underlying physiological changes of fatigue
- Finding biometrics (i.e. from sEMG and cw-NIRS parameters) related to exercise endurance

Isometric exercise was chosen to perform an exercise under normal conditions (i.e. without under ischemia). However, the force levels were deliberately chosen to be high (50% and 75% MVC) so that oxygen source will be restricted by muscle contraction so that oxygen consumption and decline can be observable (i.e. oxygen consumption would not be balanced with oxygen supply).

The protocol was as follows. First maximal hand grip force of the dominant hand was measured. After this measurement, there was a 5 minutes break. Before starting exercise, there was 1 minute of resting. Then subject was asked to maintain isometric hand grip exercise at the target force level as long as he/she can, which will

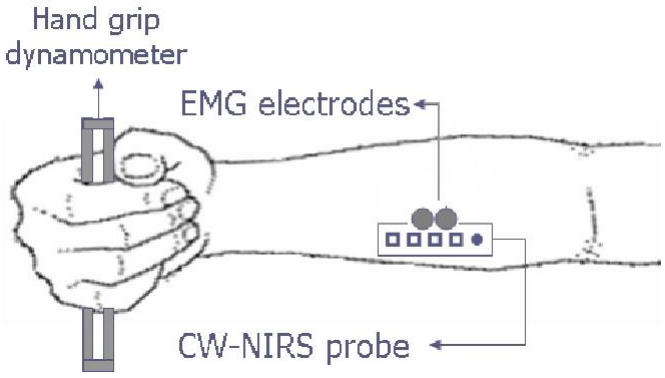

Figure 6.7 Illustration of the hand grip exercise

be one of these, 75% or 50% of maximal value. The subject was presented force level he applied on the computer screen in real time so that he can keep the force level constant. When the subject is no longer able to maintain the target force level (within 5-10% margin), the subject was asked to stop hand grip exercise and then there was a resting period of 15-20 minutes between the two measurements.

In the exercise, hand grip force was measured by the hand grip transducer (BIOPAC, SS25LA hand grip dynamometer). From the flexor digitorum superficialis muscle, both cw-NIRS (with NIROXCOPE 301, Boğaziçi University, Biomedical Eng. Inst.) and EMG measurements were taken. Distance between sEMG electrodes were nearly 2 cm. The muscle is located as outlined in Blackwell et al. [140]. Subjects were asked to resists their forth fingers against external resistance and the contracting muscle was palpated at the same time. There were 4 available detectors at distances of 1.0, 2.0, 3.0 and 4.0 cm from the source for the cw-NIRS. The detector at 3.0 cm was used for the cw-NIRS. PowerLab instruments PowerLab 16/30 ML880/P data acquisition system with ML132 and ML135 amplifiers was used for the sEMG measurements with 2 kHz sampling rate. The amplifiers are suitable for human measurements. The skin surface was shaved, rubbed with sandpaper and cleaned with liquid containing 70 degrees alcohol.

In total 16 subjects participated in the experiment. However, some subjects did not accomplish both two MVC levels of 50% and 75% and some of the data were not valid, i.e. force-time curve was not consistent. Hence, data of 11 subjects were used.

They were all rowers and canoe athletes, with age 22.6± 3.2 years, height 1.8±0.1 [m.] and weight 77.0±9.8 [kg.]. Fat thickness range measured on the FDS muscle is 2.1±0.7 mm. The personal characteristics of the subjects are given in the appendix, in Table D.1.

Acquired sEMG signals are filtered with 10 Hz high pass filter (Butterworth filter, 4th order) and notch filter ([49.5-50.5] Hz stop band, Butterworth filter, 4th order). Measured and found sEMG parameters are root mean square (RMS), mean frequency (MNF) and median frequency (MDF) (found with EMGALY.1.2 program, explained in the appendix section B). The values of these parameters are found for each non-overlapping time windows of duration 0.5 seconds. As explained in section the section B), slopes of least squares fittings for the mentioned parameters are found for the entire selected exercise time portion. Percentage change (% changes) and percentage change in seconds (%/seconds) are computed for the corresponding least squares line fits.

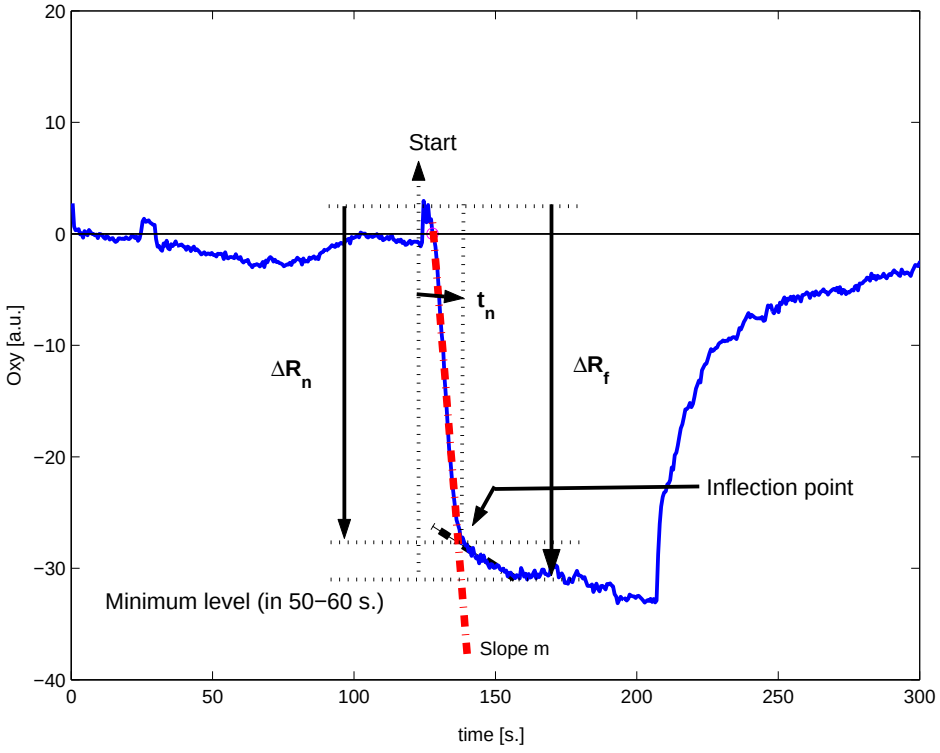

Figure 6.8 Inflection point determination and related parameters

Inflection point parameter is calculated for cw-NIRS besides $\Delta[HbO_2]$, $\Delta[Hb]$ and *oxy* signal(=$\Delta[HbO_2]$ - $\Delta[Hb]$). Inflection duration is the time duration from start of exercise to the point where initial fast decrease rate of *oxy* signal changes considerably, an example shown in Figure 6.8. It is found as as outlined in Yamaji et al. [141]: first a time range of interest is selected. The time range is selected from the start of the exercise with duration up to 50-60 seconds. In this time range, a time point is selected in this range and two time range segments are formed, from start of the exercise to the selected time (first segment) and from selected time instant to the end of range. Least squares of line fittings to these two segments are found. This time point is moved from start of range to the end of it to consider all possible two segments in the selected time range. Inflection point is found from all these available points such that line fits of least squares are significant, first segment's slope is higher than that of second segment's and sum of determination coefficients of least squares fits are maximum.

The change for the concentration from start of the exercise to the inflection point is called ΔR_n and change from start to the maximum change point (i.e. to the peak or minimum) in the first minute of exercise is labeled as ΔR_f, depicted in Figure 6.8. When second subscript is used, it indicates exercise level.

6.5.1 Results

Mean and standard deviations of the sEMG and NIRS parameters for the two exercise levels are given in the Tables 6.1 and 6.2, respectively. The individual values of the sEMG parameters are given in the appendix C, in Tables D.2 and D.3 for 50% and 75% MVC hand grip exercises, respectively. The Tables D.4 (for %50 MVC level) and D.5 (for %50 MVC level) list the NIRS parameters' values. Figures 6.11 to 6.22 depict selected scatter plots between sEMG paramaters, cw-NIRS parameters and time.

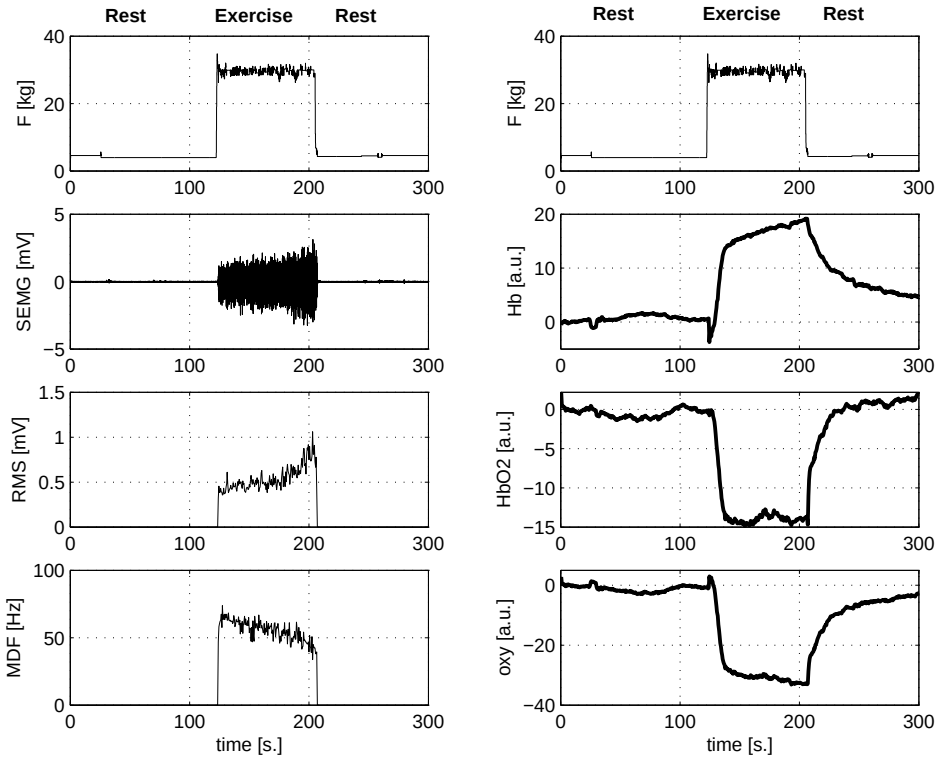

Figure 6.9 Sample simultaneous sEMG and NIRS recording at 50% MVC exercise level

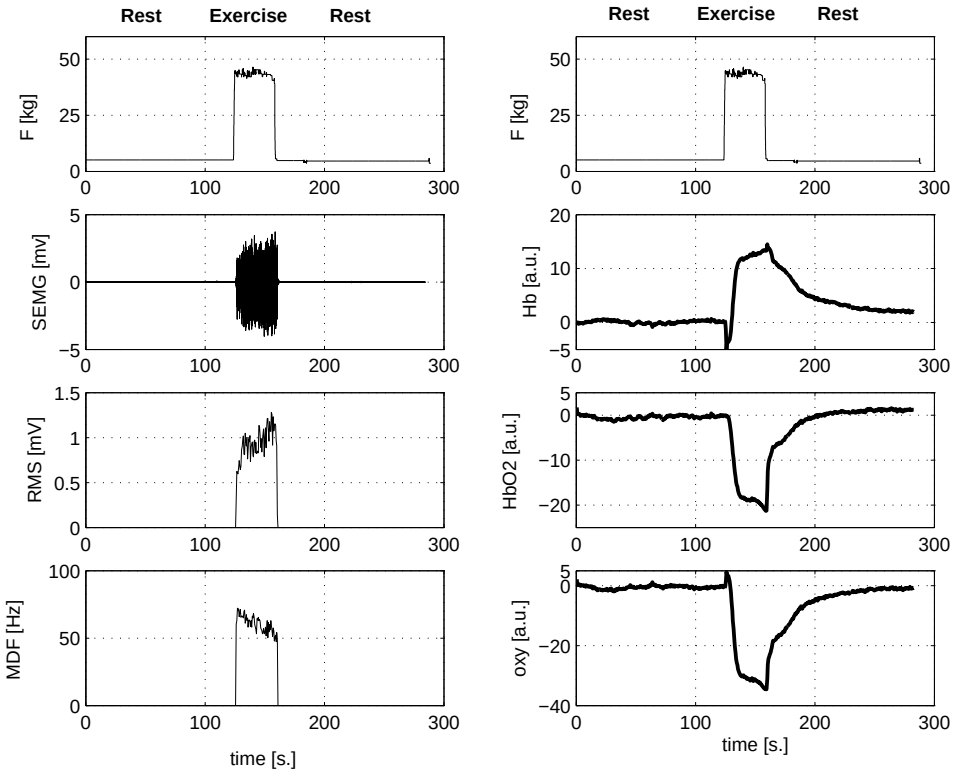

Figure 6.10 Sample simultaneous sEMG and NIRS recording at 75% MVC exercise level (for the same subject whose 50% MVC level data given in Figure 6.9)

Least squares fit of a straight lines to shown data were also drawn in these figures. Equation of the fitted line to the plotted data along with its goodness of fit measure (R^2, also called coefficient of determination [142], is defined as the ratio of the sum of squares of the regression and the total sum of squares) is also given in the figures. R^2 parameter is referred as the amount of the variability in the data accounted by the fitted model [142]. In these plots, shown CC parameter gives the correlation coefficient between the plotted parameters. Statistically significant plots were shown in bold font.

The mean duration are 83.0±20.8 sec. and 37.6±4.8 sec. for 50% and 75% MVC level exercises, respectively (the durations are based on force curve and sEMG segmentation, hence multiple of 0.5 seconds). The difference is statistically significant ($P<0.0001$, paired t-test). Hence the duration in 75% MVC exercise level is significantly shorter.

6.5.1.1 cw-NIRS Parameters. In both exercise levels, $\triangle$[HbO_2] and $\triangle$[Hb] change in opposite directions linearly at high rates following the start of the exercise. This initial pattern is called the fast phase. This same fast phase is also present in *oxy* signal. In a short while, $\triangle$[Hb] and $\triangle$[HbO_2] reach either a plateau or a slow change phase. $\triangle$[Hb] has a rather more plateau like pattern compared to $\triangle$[HbO_2]. In some subjects, increase in $\triangle$[HbO_2] is also observed with a high magnitude. The inflection duration parameter, which is directly related to the first fast phase is significantly different between the two exercise levels, for all $\triangle$[HbO_2] (15.9±10.8 vs. 9.2±2.1 s., $P<0.05$), $\triangle$[Hb] (15.2±8.2 vs. 9.1±2.2 s., $P<0.01$) and *oxy* (16.0±10.5 vs. 9.4±2.5 s., $P<0.05$). The slope derived in this fast phase is also significantly different between the 50% and 75% MVC levels, for all $\triangle$[HbO_2] (-1.0±0.6 vs. -1.6±0.7 [a.u.], $P<0.01$), $\triangle$[Hb] (1.1±0.5 vs. 1.6 ±0.7 [a.u.], $P<0.01$) and *oxy* (-2.0±1.1 vs. -3.2±1.4 [a.u.], $P<0.01$). An interesting point to note is that mean magnitude change parameters ΔR_n and ΔR_f were similar between the two exercise levels for all three NIRS parameters. The individual ratios $\Delta R_{n,50}/\Delta R_{n,75}$ and $\Delta R_{f,50}/\Delta R_{f,75}$ are given in the Table D.4. Numerically, the ratio of $\Delta R_{f,50}/\Delta R_{f,75}$ (where the seconds subscript indicates

exercise level) is in between 0.8-1.0 (except values 0.7, 1.5 and 1.6) for $\triangle$[HbO_2], in between 0.7-1.3 (except 3.2) for $\triangle$[Hb] and in between 0.8-1.1 (except 0.7, 1.3 and 2.7) for the *oxy* parameter. The value of $\Delta R_{n,50}/\Delta R_{n,75}$ is in the range 0.7-1.2 for $\triangle$[HbO_2] (with exception values of 0.3, 1.5 and 1.7), $\triangle$[HbO_2] (along with values 0.5, 0.6, 1.5 and 3.2) and *oxy* (along with values 0.4, 1.5 and 2.7).

The cw-NIRS results changed in numbers, but difference between 50% and 75% MVC remained significant for inflection durations and slopes when the outlier data for subjects 2 and 5 were removed (because of their high valued inflection durations). As given in Table 6.1, the inflection durations changed to $\triangle$[Hb] (11.8$\pm$2.9 vs. 8.4$\pm$1.6 s., $P<0.05$), $\triangle$[HbO_2] (11.2$\pm$2.8 vs. 8.6$\pm$1.7 s., $P<0.01$) and *oxy* (11.6$\pm$2.6 vs. 8.5$\pm$1.6 s., $P<0.05$). The slope values become between (the 50% and 75% MVC levels), 1.2$\pm$0.5 vs. 1.8$\pm$0.6 [a.u.] (P <0.01) for $\triangle$[Hb], -1.2$\pm$0.5 vs. -1.8 $\pm$0.5 [a.u.] (P <0.01) for $\triangle$[HbO_2] and -2.3$\pm$0.9 vs. -3.6$\pm$1.1 [a.u.] (P <0.01) for *oxy*.

An important finding is the relationship between inflection duration and exercise duration. The correlation between inflection durations and exercise duration jumped to 0.53 for $\triangle$[Hb], 0.54 for $\triangle$[HbO_2] and 0.63 for *oxy* (P =0.07) when the two outliers were removed (shown in Figure 6.16 and given in Table D.7). Table D.8 lists correlation values for 75% MVC level. The correlation coefficient values are r=0.60 (P =0.052) and 0.59 (P =0.056) for correlations between exercise duration and $t_{n,\mathrm{Hb}}$, $t_{n,\mathrm{oxy}}$, with P values close to statistical significance level of 0.05.

6.5.1.2 sEMG Parameters. Mean RMS changes are positive with very large variation, 1.0$\pm$1.3 and 1.2$\pm$0.9 [%/s.] for 50% and 75% MVC exercise levels, respectively. The slopes of least squares line fits for mean and median frequencies have significantly higher magnitudes for 75% MVC level exercise. The mean slope values for 75% MVC and 50% MVC levels are -1.0$\pm$0.3 vs. -0.5$\pm$0.3 [Hz/s.] (P <0.0001) and -1.0$\pm$0.2 vs. -0.5$\pm$0.3 [%/s.] (P <0.00001) for mean frequency. The mean fitted line slope values are found to be -0.8$\pm$0.3 vs. -0.4$\pm$0.3 [Hz/s.] (P <0.001) and -0.9$\pm$0.2 vs. -0.4$\pm$0.3 [%/s.] (P <0.0001) for median frequency. Mean percentage changes of the

Table 6.1
Mean NIRS parameter values for 50% and 75% MVC hand grip isometric exercise levels (* $P<0.05$, ** $P\leq 0.01$, paired t-test results for mean difference)

	MVC level		△[Hb]				△[HbO_2]				Oxy			
			ΔR_f	t_n	ΔR_n	m	ΔR_f	t_n	ΔR_n	m	ΔR_f	t_n	ΔR_n	m
			[a.u.]	[s.]	[a.u.]	[a.u.]	[a.u.]	[s.]	[a.u.]	[a.u.]	[a.u.]	[s.]	[a.u.]	[a.u.]
	50%	μ	15.9	15.2	10.4	1.1	-14.4	15.9	-10.5	-1.0	-28.6	16.0	-20.2	-2.0
All data		σ	3.9	8.2	3.9	0.5	3.0	10.8	3.3	0.6	5.7	10.5	6.7	1.1
included	75%	μ	14.9	**9.1****	10.6	**1.6****	-15.8	**9.2***	-11.8	**-1.6****	-28.7	**9.4***	-21.7	**-3.2****
		σ	4.3	2.2	4.5	0.7	4.0	2.1	3.7	0.7	8.3	2.5	8.1	1.4
	50%	μ	16.4	11.8	10.7	1.2	-14.4	11.2	-10.7	-1.2	-28.7	11.6	-20.5	-2.3
Two outliers		σ	4.2	2.9	4.3	0.5	3.1	2.8	3.6	0.5	6.2	2.6	7.5	0.9
excluded	75%	μ	16.2	**8.4****	11.6	**1.8***	-16.6	**8.6****	-12.6	**-1.8***	-30.8	**8.5****	-23.3	**-3.6****
		σ	2.5	1.6	4.0	0.6	3.2	1.7	3.5	0.5	5.9	1.6	7.2	1.1

Table 6.2
Means and standard deviations of the sEMG parameters for the 50% and 75% MVC hand grip isometric exercises (* $P<0.001$, ** $P<0.0001$ and *** $P<0.00001$, paired t-test results for mean difference)

MVC Level		RMS		Mean Frequency			Median Frequency		
		% change	Slope [%/s.]	% change	Slope [Hz/s.]	Slope [%/s.]	% change	Slope [Hz/s.]	Slope [%/s.]
50%	μ	91.1	1.0	-34.8	-0.5	-0.5	-34.2	-0.4	-0.4
	σ	123.7	1.3	17.6	0.3	0.3	18.7	0.3	0.3
75%	μ	47.0	1.2	-36.0	**-1.0****	**-1.0*****	-35.1	**-0.8***	**-0.9****
	σ	36.4	0.9	8.4	0.3	0.2	8.3	0.3	0.2

MNF and MDF parameters are close to each other for the two exercise levels and two frequency parameters of MNF and MDF, while the duration of 75% MVC level exercise is much shorter. The changes are -34.8±17.6% (MNF at 50% MVC), -36.0±8.4% (MNF at 75% MVC), -34.2±18.7% (MDF at 50% MVC), -35.1±8.3% (MDF at 75% MVC).

The correlations between exercise duration and sEMG parameters of MNF and MDF were high at 50% MVC level (0.59 for MNF slope [Hz/s.] and 0.60 for MNF slope [%/s.] (P <0.05, 0.56 for MDF slope [Hz/s.] and 0.55 for MDF slope [%/s.]). The correlation were low at 75% MVC level.

6.5.1.3 Correlations Between sEMG and cw-NIRS Parameters. Correlation between NIRS and sEMG parameters calculated for 50% MVC level are given in Tables D.6 and D.7. For the whole data, the correlations between the duration of the exercise and slopes of least squares line fits for MNF and MDF are above 0.55, among them correlation between duration and MNF slope ([%/s.]) is statistically significant (r=0.60, P<0.05). For the *oxy* variable, significant relationship exists between $\Delta R_n/\Delta R^{75}_{n,oxy}$ and MNF percentage change (r=-0.62, P<0.05). Relationship between $\Delta R_{n,oxy}/\Delta R^{75}_{n,oxy}$ and MDF percentage change also draws atten-

tion, with r =-0.57 (NS). A number of statistically significant relationships are present between NIRS parameters for $\triangle$[HbO_2] and sEMG parameters. Listing from Table D.6, the values of these correlations are r=-0.62 (P<0.05) between $\Delta R_{f,\mathrm{HbO_2}}$ and RMS % change, r=-0.61 (P<0.05) between $\Delta R_{f,\mathrm{HbO_2}}$ and RMS slope ([%/s.]), r=-0.69 (P<0.05) between $\Delta R_{n,\mathrm{HbO_2}}/\Delta R^{75}_{n,\mathrm{HbO_2}}$ and MNF percentage change, r=-0.60 (P<0.05) between $\Delta R_{n,\mathrm{HbO_2}}/\Delta R^{75}_{n,\mathrm{HbO_2}}$ and MNF slope ([%/s.]), r=-0.65 (P<0.05) between $\Delta R_{n,\mathrm{HbO_2}}/\Delta R^{75}_{n,\mathrm{HbO_2}}$ and MDF percentage change, r=-0.62 (P<0.05) between $\Delta R_{n,\mathrm{HbO_2}}/\Delta R^{75}_{n,\mathrm{HbO_2}}$ and MDF slope ([%/s.]). Statistically not significant but important to notice correlations are between MNF percentage change and $\Delta R_{f,\mathrm{HbO_2}}/\Delta R^{75}_{f,\mathrm{HbO_2}}$ (r=-0.59), between $\Delta R_{f,\mathrm{HbO_2}}/\Delta R^{75}_{f,\mathrm{HbO_2}}$ and MDF percentage change (r=-0.55).

When the subjects 2 and 5 were removed for 50% MVC level (because of their high valued inflection durations), the correlation changed to the values given in Table D.7. It was immediately noted that number of significant correlations were increased between cw-NIRS parameters and sEMG parameters. Although the correlation between exercise duration and MNF slope ([%/s.]) is not statistically significant now, it is 0.59 still close to 0.60. And also correlation between exercise duration and slopes of least squares line fits for MNF and MDF are above 0.54.

The $\triangle$[Hb] and *oxy* had statistically significant correlations for between inflection duration and frequency parameters of MNF and MDF, with values higher than 0.68 except not statistically significant correlation for MDF percentage change for the *oxy*. The inflection duration had high correlation between MNF slope [Hz/s.] (0.81) and between MDF slope [Hz/s.] (0.80) for the $\triangle$[HbO_2]. The all $\triangle$[Hb], $\triangle$[HbO_2] and oxy parameters had statistically significant correlations between $R_{n,\mathrm{Hb}}/\Delta R_{n,\mathrm{Hb}^{75}}$ and frequency parameters of MNF and MDF. $\Delta R_{f,\mathrm{oxy}}/l\Delta R^{75}_{f,\mathrm{oxy}}$ had statistically significant correlations of -0.68 and -0.69 between MNF slope [%/s.] and MDF slope [%/s.], respectively. $\Delta R_{f,\mathrm{HbO_2}}/\Delta R^{75}_{f,\mathrm{HbO_2}}$ had statistically significant correlations of -0.67 and -0.71 between MNF % change and MDF % change, respectively. ΔR_f high statistically significant correlations between RMS parameters for $\triangle$[HbO_2] and *oxy*. ΔR_n also had high statistically significant correlations between RMS parameters for $\triangle$[Hb] and *oxy*.

Table D.8 lists correlation values for 75% MVC level. -0.53 (NS), -0.54 (NS) and -0.55 (NS) are the correlation coefficients between $\Delta R_{f,\text{oxy}}$ and MNF slope ([%/s.]), MDF percentage change, MDF slope ([%/s.]), respectively. The correlations values of ΔR_f and sEMG parameters are also high for ΔHbO_2, numerically -0.55 (NS), -0.59 (NS), -0.55 (NS), -0.55 (NS) between $\Delta R_{f,\text{HbO}_2}$ and MNF percentage change, MNF slope ([%/s.]), MDF percentage change, MDF slope ([%/s.]). Statistically significant relationships for 75% MVC level exercise are between $\Delta R_{f,\text{Hb}}$ and MNF percentage change (r=0.71), between $\Delta R_{f,\text{Hb}}$ and MNF slope [%/s.] (r=0.65), between $\Delta R_{f,\text{Hb}}$ and MDF percentage change (r=0.70), between $\Delta R_{f,\text{Hb}}$ and MDF slope [%/s.] (r=0.63), between $\Delta R_{n,\text{Hb}}$ and MNF percentage change (r=0.63), between $\Delta R_{n,\text{Hb}}$ and MNF slope [Hz/s.] (r=0.66), between $\Delta R_{n,\text{Hb}}$ and MNF slope [%/s.] (r=0.67), between $\Delta R_{n,\text{Hb}}$ and MDF percentage change (r=0.61), between $\Delta R_{n,\text{Hb}}$ and MDF slope [%/s.] (r=0.64).

A correlation analysis is also done using data obtained in both 50% and 75% MVC level exercises, given in Table D.9. In this case, correlations between exercise durations and inflection durations are all significant (0.56, 0.50 and 0.50 for $t_{n,Hb}$, t_{n,HbO_2} and $t_{n,oxy}$, respectively). 0.43, 0.69, 0.79, 0.69 and 0.78 are the statistically significant corretalation coefficients between exercise duration and RMS % change, MNF slope [Hz/s.], MNF slope [%/s.], MDF slope [Hz/s.], MDF slope [%/s.], respectively. Statistically significant correlations are found between inflection durations and sEMG parameters. They are between $t_{n,\text{Hb}}$ and RMS percentage change (r=0.44), between $t_{n,\text{Hb}}$ and MNF slope [Hz/s.] (r=0.52), between $t_{n,\text{Hb}}$ and MNF slope [%/s.] (r=0.52), between $t_{n,\text{Hb}}$ and MDF slope [Hz/s.] (r=0.56), between $t_{n,\text{Hb}}$ and MDF slope [%/s.] (r=0.54), between t_{n,HbO_2} and RMS percentage change (r=0.50), between t_{n,HbO_2} and MNF slope [Hz/s.] (r=0.46), between t_{n,HbO_2} and MNF slope [%/s.] (r=0.45), between t_{n,HbO_2} and MDF slope [Hz/s.] (r=0.50), between t_{n,HbO_2} and MDF slope [%/s.] (r=0.48), between $t_{n,oxy}$ and MNF slope [Hz/s.] (r=0.43), between $t_{n,oxy}$ and MNF slope [%/s.] (r=0.43), between $t_{n,oxy}$ and MDF slope [Hz/s.] (r=0.47), between $t_{n,oxy}$ and MDF slope [%/s.] (r=0.45).

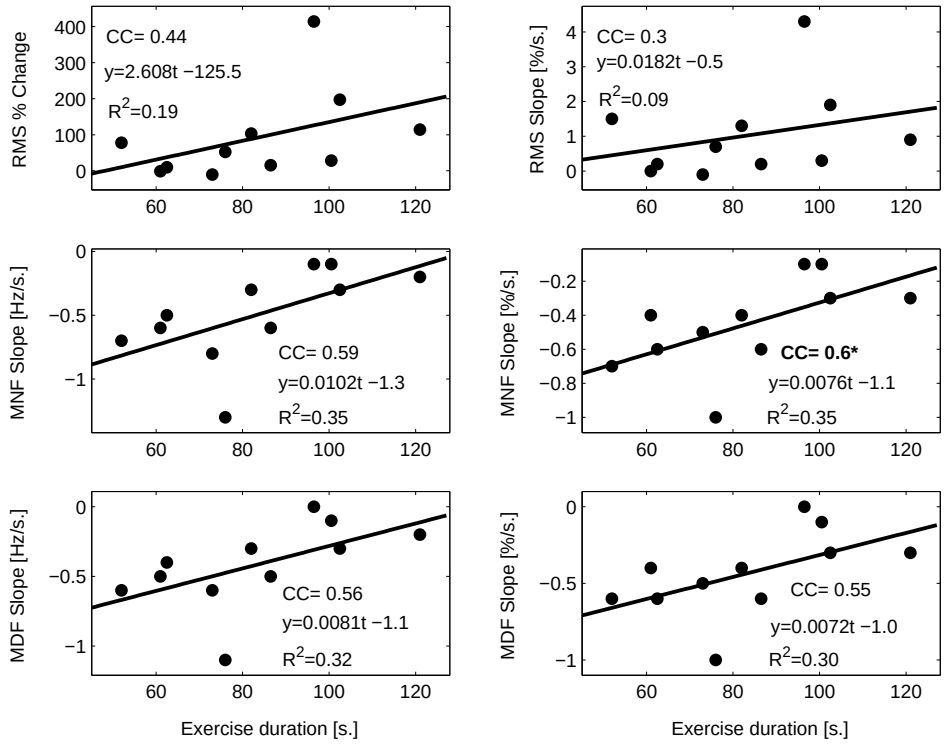

Figure 6.11 Scatter plots between exercise duration and sEMG parameters for 50% MVC level (* and bold font indicates statistically significant correlation for 0.05 P level)

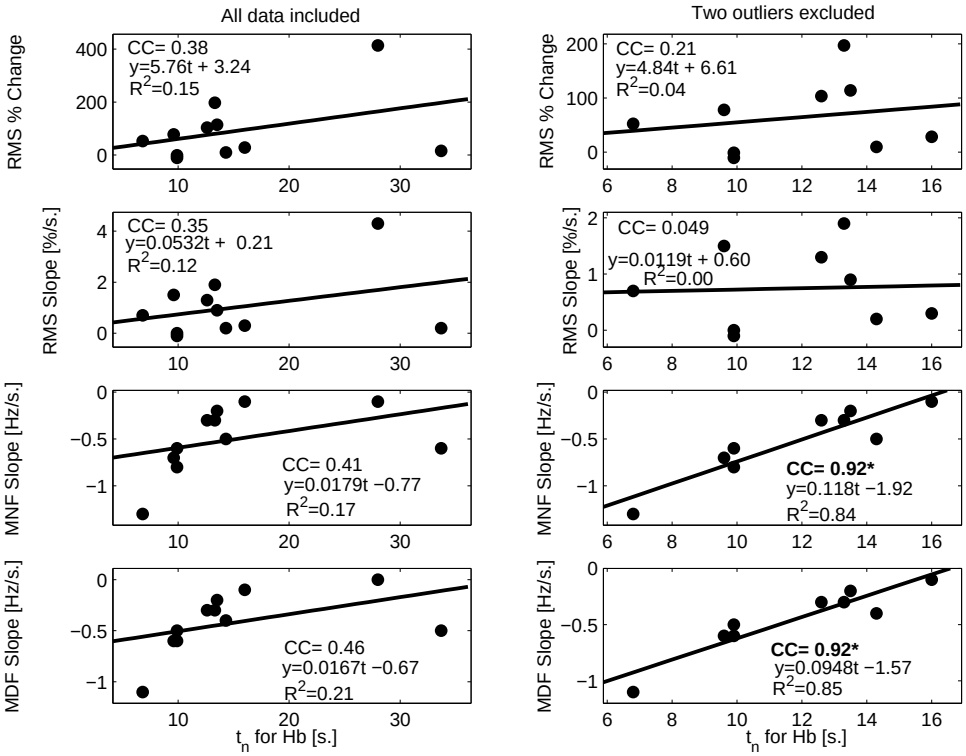

Figure 6.12 Scatter plots between sEMG parameters and $t_{n,Hb}$ for 50% MVC level, right column results are for outliers (subjects 2 and 5) excluded case (* and bold font indicates $P < 0.05$)

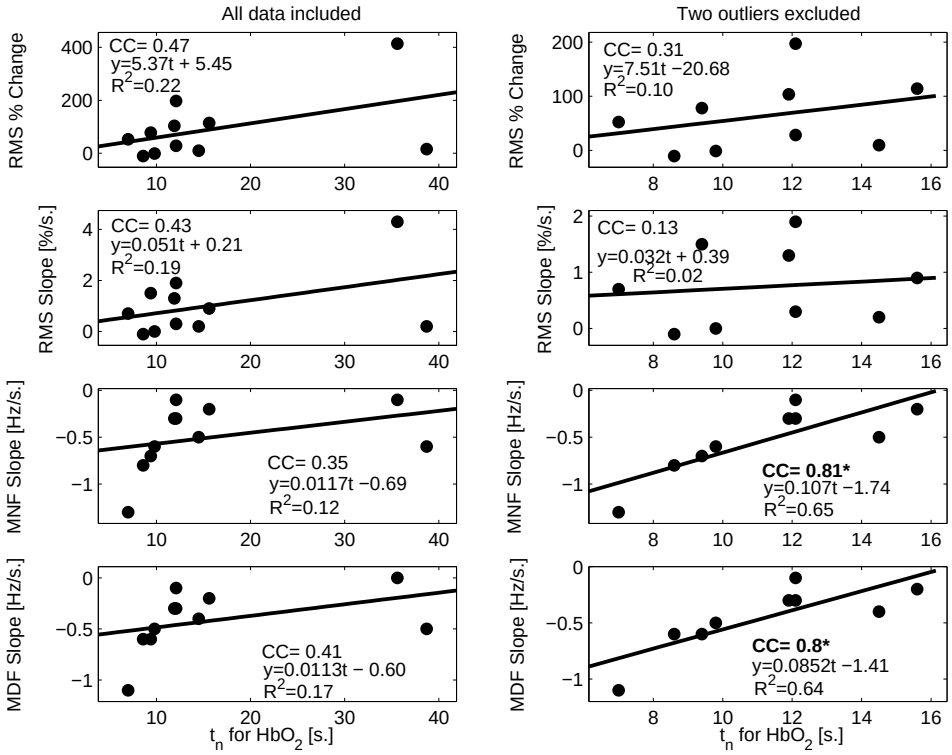

Figure 6.13 Scatter plots between sEMG parameters and t_{n,HbO_2} for 50% MVC level, right column results are for outliers excluded case (* and bold font indicates $P < 0.05$)

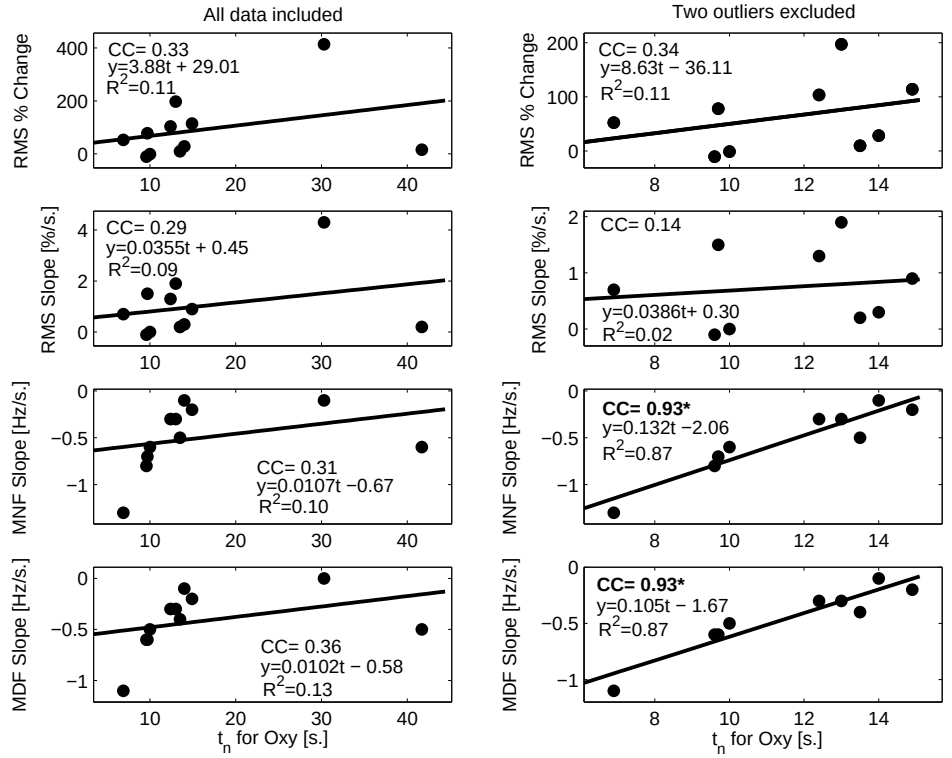

Figure 6.14 Scatter plots between sEMG parameters and $t_{n,oxy}$ for 50% MVC level, right column results are for outliers (subjects 2 and 5) excluded case (* and bold font indicates $P < 0.05$)

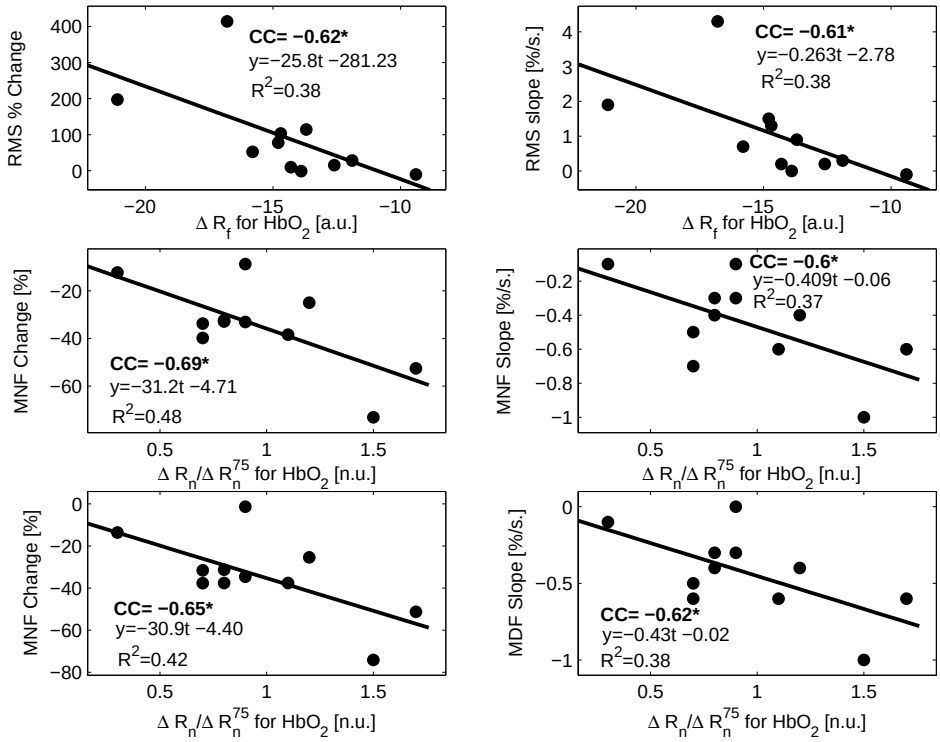

Figure 6.15 Scatter plots between sEMG parameters and cw-NIRS amplitude parameters for HbO_2 at 50% MVC level, (* and bold font indicates $P < 0.05$)

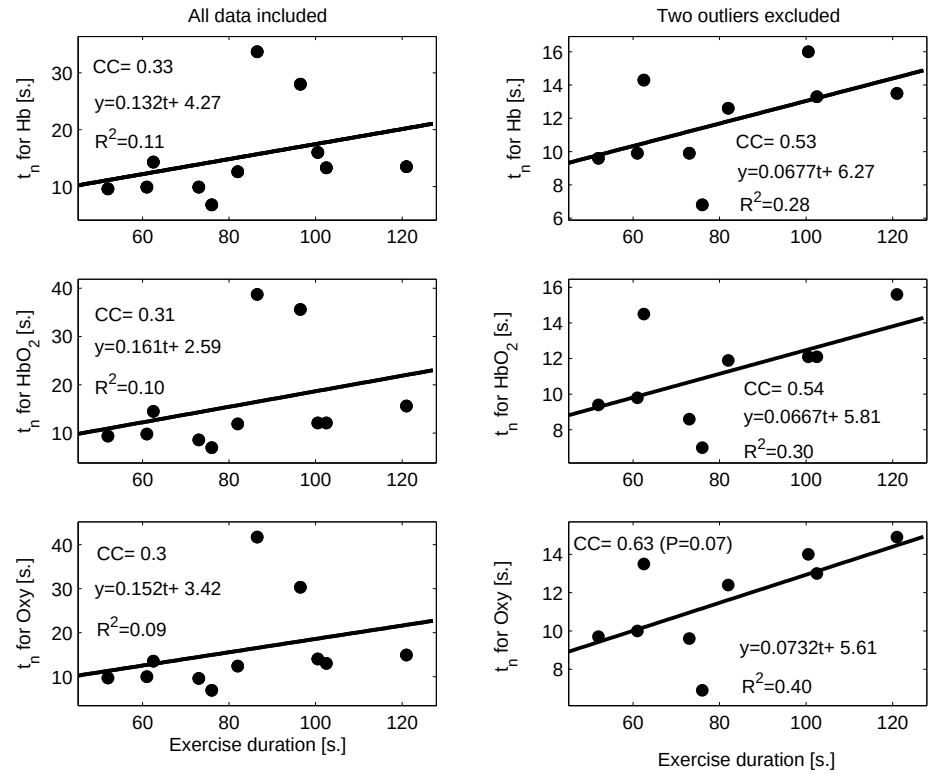

Figure 6.16 Scatter plots between exercise duration and inflection durations for 50% MVC level, right column results are for outliers (subjects 2 and 5) excluded case

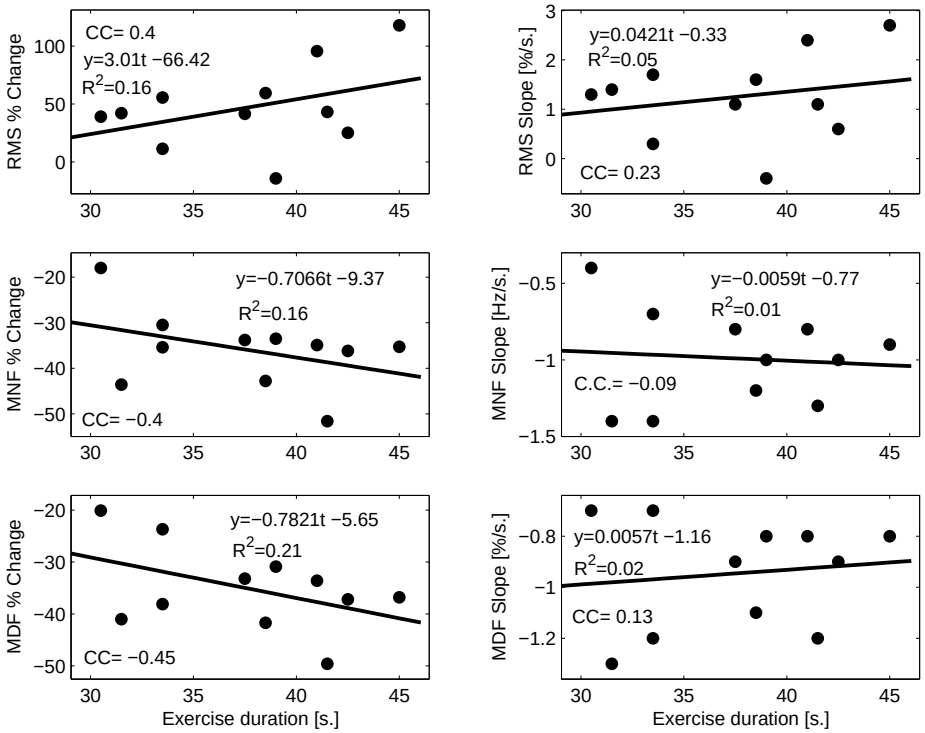

Figure 6.17 Scatter plots between exercise duration and sEMG parameters for 75% MVC level

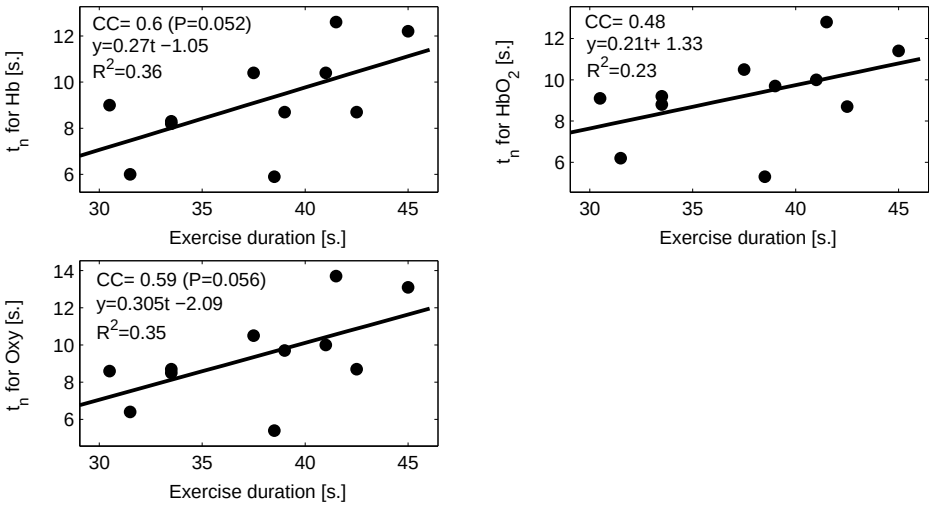

Figure 6.18 Scatter plots between exercise duration and inflection durations for 75% MVC level

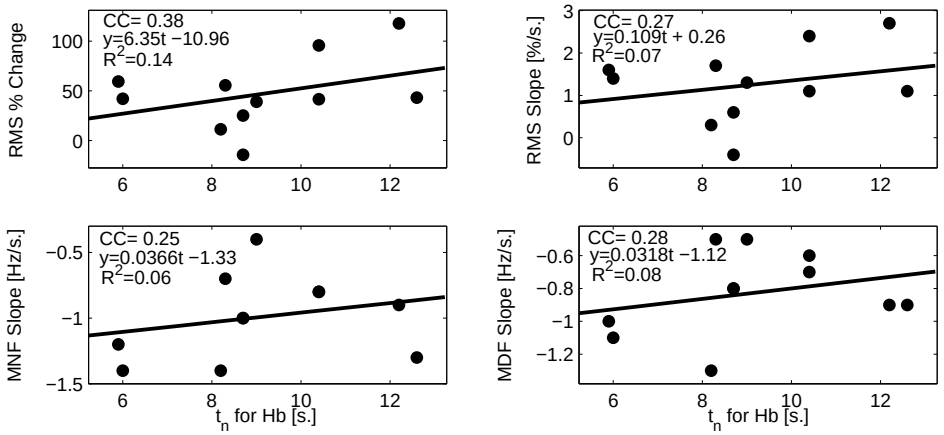

Figure 6.19 Scatter plots between sEMG parameters and $t_{n,Hb}$ for 75% MVC level

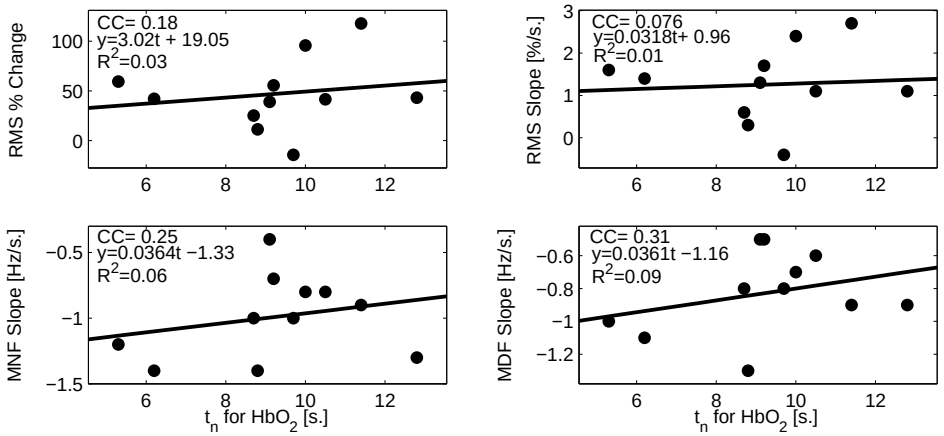

Figure 6.20 Scatter plots between sEMG parameters and t_{n,HbO_2} for 75% MVC level

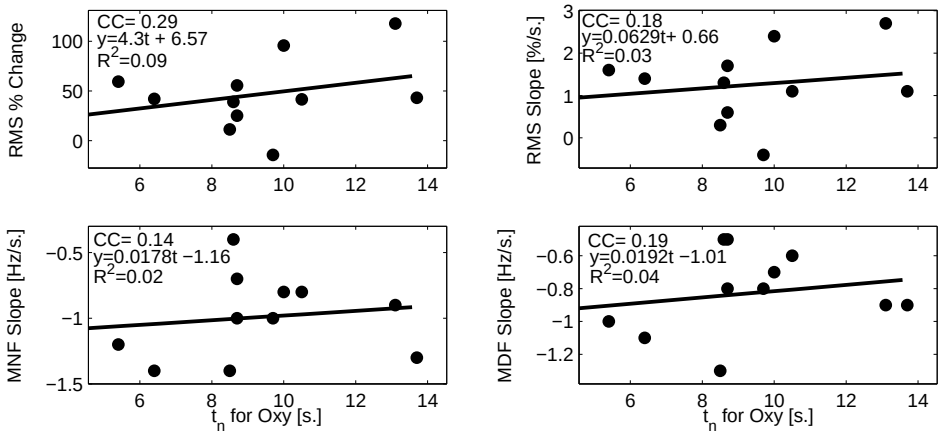

Figure 6.21 Scatter plots between sEMG parameters and $t_{n,oxy}$ for 75% MVC level

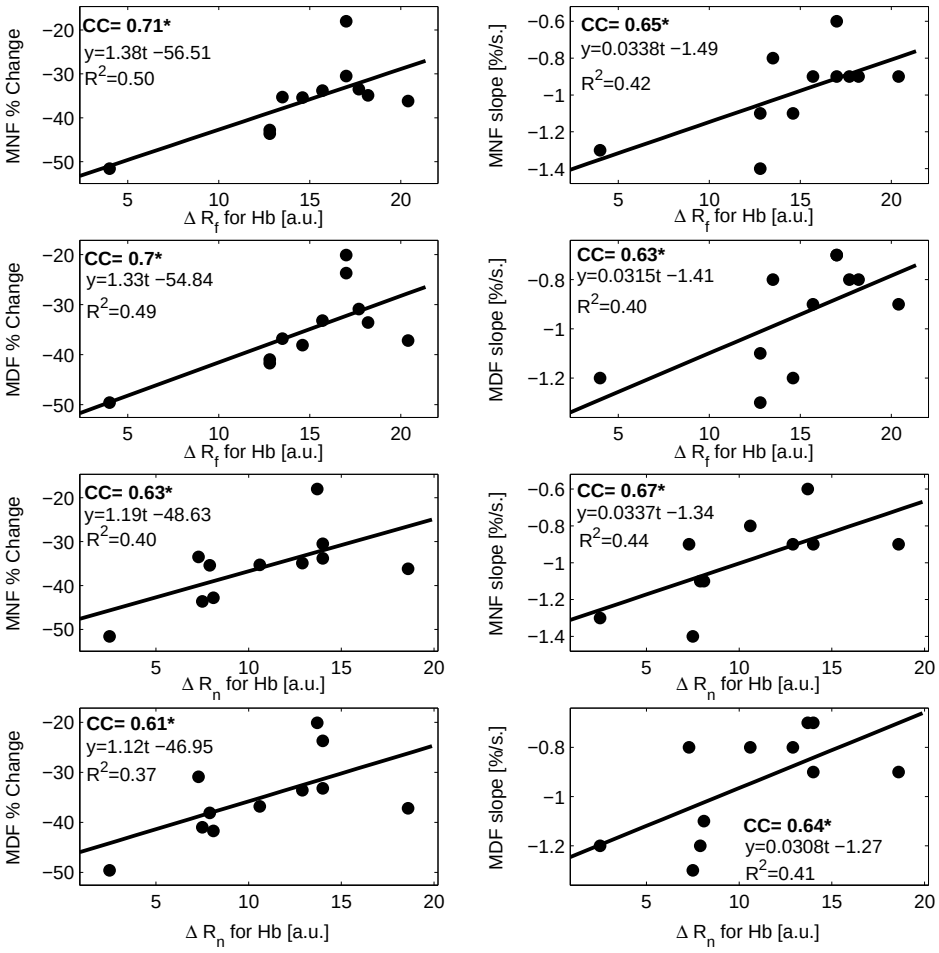

Figure 6.22 Scatter plots between cw-NIRS amplitude parameters for Hb and sEMG parameters which have statistically significant correlations for 75% MVC level, (* and bold font indicates $P < 0.05$)

6.5.2 Discussion

In this study, force measurement, surface electromyography (sEMG) and continuous wave near-infrared spectroscopy (cw-NIRS) measurement techniques were utilized for study of fatigue in isometric and isotonic exercise. The aim of this study was to assess the effects of sport specific endurance and fatigue profile for sustained isometric contractions during grip force with using surface EMG and NIRS parameters in rowers and canoe athletes. The chosen muscle was FDS (flexor digitorum superficialis). The exercise levels were 50% and 75% MVC levels. The subjects tried to keep hand grip force level constant, which was presented to them real time on computer screen.

Here, the findings are discussed under the headings of cw-NIRS findings, sEMG findings correlation between sEMG and cw-NIRS parameters, possible applications and limitations of the study.

6.5.2.1 cw-NIRS Findings. cw-NIRS parameters of $\triangle$[Hb], $\triangle$[HbO_2] and *oxy* initially had fast changes (fast increase for $\triangle$[Hb], decrease for $\triangle$[HbO_2] and oxy). $\triangle$[Hb] and $\triangle$[HbO_2] changed in opposite directions linearly at speedy rates following the immediately start of the exercise. These changes were speedy and at constant linear rates immediately following start of the exercise. In fact at the immediate start of the exercise before the fast change phase, there were some small fluctuations which could be due to motion artifacts, i.e. handling the hand grip dynamometer and muscle shape changes. At the start of the exercise, sudden force development to high levels leads to muscular contraction and pressure increase, as well as blood movement under the probed volume. In fact, DeLorey et al. [143] observed nearly 13 s. of unchanged [Hb] in the start of the experiment which was incremental cycling starting from 20W to 80% of the lactated threshold level. The work transitions were 8 min. and were preceded and followed by 20 W, 8 min. cycling. This unchange in [Hb] was explained by the effects of muscular contraction on Hb volume rather than a "metabolic" inertia. It can be said that observed transition before fast changes in our study was also caused by muscular contractions.

In the fast phase, all patterns of $\triangle$[HbO_2], $\triangle$[HbO_2] and *oxy* initially started with fast changes. The fast phase at the beginning of the exercise is caused by blood flow occlusion and high demand of oxygen by aerobic energy metabolism. *Oxy* signal reflects balance between oxygen supply and oxygen demand. The force levels used in our study is 50 and 75% MVC, which lead to intramuscular pressure and impaired blood flow, which prevents oxygen supply. This observed pattern is also observed in the previous studies in the literature. This initial fast phase change of NIRS derived parameter of tissue oxygenation index followed by slow phase is shown also by Fellici et al. [144] for static isometric exercises each lasting 30 seconds, and in the isometric exercise study of Moalla et al. [145]. In the sustained (maintaining maximal force)

static grip study of Yamaji et al.[141], these fast phase followed by decreased change rate was observed. In the study of Nakada et al. [146], the pattern is observed for repeated rhythmic grip.

The exercise duration of higher force level at 75% MVC was significantly shorter compared to the 50% MVC exercise, as expected. The slopes were steeper and inflection durations were significantly shorter in 75% MVC level, the values given in section 6.5.1.1.

Our study confirms that muscle deoxygenation rate is higher for 75% MVC level than for 50% MVC, supporting the finding of Felici et al. [144] who found that the highest desaturation at 80% MVC level and that deoxygenation rate increased with force level. In the study of Felici et al. [144], the static isometric exercises were at 20, 40, 60 and 80% MVC levels, each lasting 30 seconds for the biceps brachii muscle. Sinusoidal isometric exercises were also performed from 20% MVC to 60% MVC (mid level 40% MVC) and from 40% MVC to 80% MVC (mid level 60% MVC). The sEMG and NIRS measurements were simultaneous. On the contrary, Kahn et al. [147] found that highest muscle deoxygenation occurs at 50% MVC level. The study procedure in Kahn et al. [147] consists of first isotonic isometric part where the aim is to maintain predefined force level (either 25, 40, 50, 60, 70 or 100% MVC) until failure , and then 120 seconds for anisotonic isometric contraction.

As pointed in section 6.5.1.1, an interesting point to note is that mean magnitude change parameters ΔR_n and ΔR_f were similar between the two exercise levels for all three NIRS parameters.

The motivation behind inflection duration was that initial rate of change for the cw-NIRS parameters were much higher than the rest of exercise for the isometric exercise. The important and interesting finding was that inflection point determined from fast phase (the first 15 s. of exercise duration) was mildly correlated with total exercise duration (especially at 75% MVC where the correlations were 0.6 (P =0.052) for $\triangle$[Hb] and 0.59 for *oxy* (P =0.056)) which means it could give information about

total exercise duration, hence endurance. Also when the two outliers were removed, the correlation between inflection durations and exercise duration were to 0.53 for $\triangle$[Hb], 0.54 for $\triangle[HbO_2]$ and 0.63 for *oxy* (P =0.07).

The observation in these measurements was that after the fast phase, the pattern in $\triangle$[Hb] was usually a plateau like trace. However, $\triangle[HbO_2]$ (and *oxy*) had variations in the pattern after the initial fast phase region. Different patterns were slowly decreasing, slowly increasing fluctuations or plateau like traces for the *oxy* and $\triangle[HbO_2]$. *Oxy* signal had different patterns. Afterwards this fast phase, there were different patterns of slowly decreasing, slowly increasing fluctuations or plateau like phases for the *oxy* signal.

Felici et al. [144] also reported that total Hb were not stationary even at 60% and 80% MVC static exercise even at 60% and 80% static exercises (in the graphs, it is increasing after initial decrease at the start), authors propose that this finding could be explained by redistribution of forces between muscle units and of those attributable to viscoelastic tissues leading to reduction in internal muscle pressure letting a blood supply in small amount which does not match metabolic demand. van Beekvelt et al. [51] observed total hemoglobin increase in the phase of arterial occlusion of 45 s. protocol (applied after isometric exercise to find oxygen consumption), which is also observed in some other studies where it is expected to stay constant [148, 149, 150, 58]. van Beekvelt et al. [51] states that this is also seen in the figures of the studies in Tamaki et al. [151] and Ferrari et al. [62]. This is explained not by incomplete arterial occlusion but by redistribution of blood [148, 149, 150, 58, 51]. Fujii et al. [152] observed constant oxygenation level after rapid decrease in oxygenation during regulated clenching for 10 s. (which is a much shorter duration) at 5 kg force placed on the first molar of the mandible on the habitual chewing side, from masseter muscle.

The source of oxygen decrease can not be determined by cw-NIRS only, i.e. it can be because of oxygen utilization or blood flow occlusion [153]. In any case, observed decreases are important and can give idea about oxygen deficiency. In this study, isometric exercise was chosen to perform an exercise under normal conditions

(i.e. without under ischemia). However, the force levels were deliberately chosen to be high (50% and 75% MVC) so that oxygen source will be restricted by muscle contraction so that oxygen consumption and decline can be observable (i.e. oxygen consumption would not be balanced with oxygen supply). Pitcher and Miles [154] states that under MVC exercise, the blood flow becomes restricted until the force level drops below 50% MVC and that fall of force during MVC is a measure of anaerobic fatigue and it is only little and partially related to the performance of aerobic fibres.

After the end of exercise, $\triangle$[Hb], $\triangle$[HbO_2] and *oxy* have fast recoveries with hyperaemic phase. $\triangle$[Hb] decreases while $\triangle$[HbO_2] and *oxy* increases, again at speedy rates like the phase in the start of the exercise.

6.5.2.2 sEMG Findings. In the experiments, typical sEMG findings of MNF and MDF decrease are observed in the subjects. sEMG parameters of MNF and MDF had higher decline rates at 75% MVC level compared to the 50% MVC level. As given in section 6.5.1, the mean±standard deviation values of slope values for 75% MVC and 50% MVC levels are -1.0±0.3 vs. -0.5±0.3 [Hz/s.] (P <0.0001) and -1.0±0.2 vs. -0.5±0.3 [%/s.] (P <0.00001) for mean frequency. The slopes were -0.8±0.3 vs. -0.4±0.3 [Hz/s.] (P <0.001) and -0.9±0.2 vs. -0.4±0.3 [%/s.] (P <0.0001) for median frequency.

Mean percentage changes of the MNF and MDF parameters were close to each other for the two exercise levels and two frequency parameters of MNF (34.8±17.6% at 50% MVC and 36.0±8.4% at 75% MVC) and MDF (34.2±18.7 at 50% MVC and 35.1±8.3% at 75% MVC), while the duration of 75% MVC level exercise is much shorter. Hence it can be deduced that MNF and MDF were reduced to same percentage levels in 75% MVC level in much shorter exercise duration. The changes are -34.8±17.6% (MNF at 50% MVC), -36.0±8.4% (MNF at 75% MVC), -34.2±18.7% (MDF at 50% MVC), -35.1±8.3% (MDF at 75% MVC).

Exercise duration had significantly higher correlations with sEMG parameters

at force level of 50% MVC compared to 75% MVC level. At this force level, the correlations between the duration of the exercise and slopes of least squares line fits for MNF and MDF are above 0.54 (Tables D.6 and D.7), among them correlation between duration and MNF slope ([%/s.]) is statistically significant when all data was included (r=0.60, P<0.05). This correlations between exercise duration and sEMG parameters disappeared at 75% MVC level. The correlation between exercise duration and the slopes of fitted lines of MNF and MDF and were below 0.13 (Tables D.8).

The steeper decline in CV, MNF or MDF for higher force levels has been reported also in various studies [155, 156, 157, 158, 159]. These are mostly explained by conduction velocity decrease in muscle myofibrils and synchronization of different motor units.

Power spectral density is affected by CV, MU firing rate, and also affected by action potential shapes [160]. The power spectrum shift to lower frequency region is a well reported fact for fatiguing exercises which is in general attributed to conduction velocity (CV) [161, 162] decrease and motor unit (MU) synchronization [163, 164]. The increase in low frequency part of the spectrum is more related to MU firing rate increase while action potential conduction velocity decrease is stated to be responsible for the high frequency content loss [165, 160, 166, 167]. MNF or MDF is reported to be linearly related to CV [168, 169, 170]. Accumulation of energy metabolism by-products such as lactate hold responsible for CV decrease by leading to reduction in action potential conduction velocity [171]. Potassium ion concentration ($[K^+]$) increases because of prevention of blood flow during sustained isometric contractions [172, 173, 174] which causes decrement of gradient across muscle fiber membrane, decrease of muscle fiber excitability [175], and also decrease of CV [176]. pH is also reduced by increase in the concentration of lactic acid, since accumulation of it also impairs excitability of muscle membrane [171, 159, 176]. There are studies demonstrating link between MNF and lactate production (Moritani et al. [177] and Horika and Ishiko [178]). A detailed list of factors affecting the EMG signal is given in DeLuca [165].

Impairments in excitation-contraction coupling because of drop in Ca^{2+} release

as well as reduced Ca^{2+} sensitivity of the contractile proteins and T-tubule excitability reductions are all leading to fatigue development [179].

Sadoyama et al. [180] states that spectral modifications are partly due to CV decrement. Masuda et al. [176] found that although MDF decreased during both static and dynamic contraction, CV did not decrease during dynamic contractions but in static contraction. An apparent difference is blood blow which allows intermittent oxygen supply and removal of metabolic by-products during dynamic contractions. *This also shows that CV is not the unique factor determining MNF/MDF change.* Zwarts et al. [181] also points out that CV is not the only factor for MNF/MDF changes. They have observed partial MDF recovery without CV recovery during recovery under ischemia after isometric contractions at 40% maximum voluntary contraction.

Fast fibers of larger motor units are recruited with increasing force [182]. This is according to the Henneman's 'size principle' [183] which states that recruitment order is from low threshold type I motor units to high threshold type II motor units. Type II motor units have higher CV's because of shorter duration action potentials [184]. In terms of MNF decrease, fatigue is more pronounced in type II fiber dominant muscles by Komi and Tesch [185], Moritani et al. [186, 187, 188].

In this experiment results, mean RMS changes were positive with very large variation, 1.0±1.3 and 1.2±0.9 [%/s.] for 50% and 75% MVC exercise levels, respectively. Sustained submaximal constant force isometric exercises have been reported to have the finding of integrated EMG (analogous to RMS) signal increase [189, 190, 49, 168] to compensate for contractility impairment which is explained with MU recruitment and firing rate increase [191, 49]. Fatigue also influences MU recruitment [190]. RMS signal decrease is observed for MVC (100% MVC) exercises [192, 190], different than submaximal isometric exercises.

6.5.2.3 Revealed Fatigue Mechanisms. It is clear that reduced $[HbO_2]$ levels indicated oxygen usage and its limitation by muscular contraction at the employed high

force levels. Sustained contraction limited supply of the oxygen and other metabolites needed for energy production and prevented clearance of metabolic by-products by impaired blood flow.

Studies show that muscle flow constriction is started in sustained contraction over about 20-25% MVC [193, 194, 195, 196]. Sadamoto et al. [197] found increasing mean rectified EMG and IMP when force kept constant. They concluded that muscle tissue compliance decreased during fatigue. It has been shown that intramuscular pressure (IMP) is positively correlated with force during static contractions [198, 199]. This leads to compression of vascular beds and occlusion of blood flow since since muscle arterial pressure is likely to exceed mean arterial pressure [200], hence restriction in blood flow [197, 201, 202, 147]. Since large flow means large oxygen supply, IMP increase causes decrease in oxygen supply. In this case, intramuscular oxygen is utilized. The occlusion of blood flow also prevents the removal of muscle metabolic by-products and maintenance of homeostasis in the muscle [40]. In normal conditions, blood flow increases with exercise intensity for the higher oxygen demand. However, higher force level increases IMP, which are related linearly [198, 201]. Local vasodilation takes place because of released nitric oxide, adenosine and acetylcholine. Blood flow increase by local vasodilation during exercise is counterbalanced by mechanical forces which cause IMP increase. In the hyperemic phase after exercise, these two effects work in the same direction for blood flow increase [203].

Force production increase is possible by increase in muscle fiber firing rate and/or new recruitment of motor units. The important thing for energy metabolism is that the proportions of energy production from aerobic and anaerobic metabolism are determined by exercise intensity [204]. High intensity exercise leads to an increase in the proportion of anaerobic metabolism [204, 205]. The contribution to the energy production of the slow twitch fibres becomes limited in the absence of oxygen although they are highly resistant to fatigue under adequate oxygen supply. Under hypoxic conditions the performance of fibers which use anaerobic pathways dominantly are affected to much less extent [154]. However their performance would be affected by the accumulation of metabolic by-products by the occlusion blood flow. Accumulation of

H^+ (pH drop) and an orthophosphate (usually just called phosphate, released by the hydrolysis of ATP or ADP) leads to fatigue development [206, 207, 208]. Hamaoka et al. [209] also stated that their observations indicated that anaerobic metabolism becomes prominent at intensities from 15-20% MVC compared to 10-15% MVC.

The hypothesis we put forward is that inflection point corresponds to the time when proportion of aerobic energy pathway is decreased significantly and proportion of anaerobic energy production starts to increase because of unavailability of oxygen in isometric contraction at high levels of 50% and 75% MVC. At the fast phase, the available oxygen is consumed by aerobic energy production mechanism until its concentration drops below a certain level. As pointed in CW-NIR findings, mean magnitude change parameters ΔR_n and ΔR_f were similar between the two exercise levels for all three NIRS parameters. Hence this confirms that oxygen was consumed until it drops to same level at 50% and 75% MVC levels exercises, being faster in 75% MVC level. After this level, proportion of anaerobic energy production pathway should increase to compensate for the drop in aerobic energy production loss. The plateau region after fast phase was much shorter in 75% MVC level exercise since the required high energy can not be supplied by anaerobic pathway alone for long time.

The higher exercise duration was correlated with inflection duration (i.e. longer fast phase region). This could reflect difference in the subjects' usage of aerobic and anaerobic energy pathways (i.e. different proportions in the fast phase between subjects) because of differences in fiber types or training effects. Another explanation could be that, although care was taken to ensure that all subjects did the experiment in the same condition, somehow more blood flow occurred in some subjects leading to more oxygen availability, consequently resulting in longer fast phase and plateau regions, hence longer exercise duration.

In fact, tissue oxygen level does not decrease down to 0 level even for long ischemia. Hamaoka et al. [209] found 26.1% oxygen saturation even after 6 min. ischemia, the value confirms their previous study [97]. They discuss that the origin of this remaining oxygen is not known exactly but possibly mitochondrial availability of

oxygen decrease leads to beginning of anaerobic metabolism to take over the aerobic metabolism. Also remaining oxygen in the venous site is not easily exchangeable with the mitochondria. Hence reduced oxygen decline rate can not be only explained by its reduced concentration, but reduced concentration affects its availability to aerobic energy pathways.

An important finding of linearity deviation at high force levels for the relationship between oxygen consumption and force was found by van Beekvelt et al. [51]. They explained it with blood flow restriction causing mismatch with oxygen demand and supply. Another possible cause they put forward was involvement of other muscle groups at high force levels for additional force production.

It is pointed out that although there is evidence that energy deficiency is a determinant factor during high-intensity exercise, the situation is more complex for prolonged exercise. Energy deficiency is not the sole explanation for prolonged exercise. Recovery of force after a 75% VO2max cycling exercise is found to have first rapid and then slow recovery, while PCr reverses above the pre-exercise level after 5 min. recovery, shown by Sahlin et al. [210]. In high intensity exercise, however recovery of force and PCr is parallel.

Kimura et al. [211] employed isometric wrist flexion exercise at 30%, 50% (1 min.) and 70% MVC levels (up to exhaustion). NIRS and ^{31}P-MRS techniques were used for investigation from flexor digitorum superficialis muscle, non-simultaneously for the same exercise. First exercise was done under arterial occlusion, called Intramuscular-O_2-Ex. Confirming results of this study and other studies, initial decline in oxygenation was found with rise in decline rate with exercise intensity increase for Intramuscular-O_2-Ex. This phase was followed by a plateau or slight decline. The initial decrease was interpreted as indication for activation of intramuscular oxygen.

Also another exercise called Anaero-Ex was performed which was preceded by 6 min. arterial occlusion to deplete oxygen before exercise. ATP costs between were found to be similar between Intramuscular-O_2-Ex and Anaero-Ex, sum of ATP pro-

duction rates (sum of oxidation, PCr break down and glycolysis) were not significantly different. Low intensity exercise at 30% MVC reflected difference between two exercises in which PCr breakdown rate was significantly lower for Intramuscular-O_2-Ex which shows contribution of aerobic metabolism. Hence authors commented that aerobic metabolism may contribute to maintaining PCr level until oxygen depletion.

Confirming the finding of Fellici et al. [144], Kimura et al. [211] did not find significant difference between the decline rates of oxygen for 50% and 70% MVC levels. Besides they found that minimum oxygen level for 70% MVC was higher than other levels which drives the authors to conclude that it was not consumed although it exists adequately because of restriction in availability of oxygen. Another explanation they offer was the larger contribution of anaerobic metabolism at higher intensities increasing from start of the exercise at higher intensities which is fast and efficient in terms of energy production speed. Another finding at these high intensities was the high proportion of glycolysis to energy production. An important thing to note is that the authors found these for the fast phase of the exercise. As in Fellici et al. [144], the authors attributed linear increase in linear oxygen consumption increase up to the 50% MVC level to progressive recruitment of type I fibers.

The energy metabolism also influences central nervous system (CNS) by altering plasma metabolite concentrations [204], hypoglycemia, hyperammonaemia. CNS has a significant role in fatigue in terms of motivation and central drive. Hence, this is also another factor besides energy deficiency in fatigue development.

6.5.2.4 Found Biometrics for Endurance Prediction. The sEMG parameters had very high correlation between exercise duration at 50% MVC but this correlation disappeared at 75% MVC level. The correlations were low at 75% MVC level.

The lower loading at 50% MVC may have caused more stable load sharing between fibers and a more controlled experiment compared to 75% MVC. *These may have caused more 'balanced' force production and 'smooth' and delayed fatigue development.*

These could explain the higher correlations between exercise duration and sEMG parameters at 50% MVC level. Motor unit rotation (or substitution) states that fatigued MU's can be switched with more 'ready' motor units [212, 213], which is speculated to be for protection of motor units from excessive fatigue for sustained low-level muscle activity [213]. This mechanism will likely to be better at lower exercise force level of 50% MVC level compared to 75% MVC level at which most of the muscle fibers would be working, i.e. at 75% MVC rotated muscle fibers would not be 'ready' compared to lower exercise levels.

Another thing to note is that exercise duration range was much longer for 75% MVC level compared to 50% MVC level. Exercise durations at 75% level were between 30.5-45.0 [s.] (37.6±4.8 [s.], COV (coefficient of variation = $100 \times \mu/\sigma$)=13%), much shorter than the durations at 50% MVC level which were between 52-121 [s.] (83.0±20.8 [s.], COV=25%). The range was much shorter for 75% MVC level 14.5 [s.] (45 -30.5) compared to 50% MVC level (=121-52= 69 [s.]). Hence at 75% MVC level, the exercise duration was already confined in 30.5-45.0 [s.] band. Although the force levels in this study were high, submaximal exertion studies are comfortable than maximal force studies, where role of voluntary control increase with the interference effect of pain [167, 214]. At 75% MVC level, the pain and related CNS factors could have affected exercise duration more compared to 50% MVC level.

The important and interesting finding was that inflection durations determined from fast phase (the first 15 s. of exercise duration) was mildly correlated with total exercise duration which means it could give information about total exercise duration, hence endurance. The correlation between inflection durations and exercise duration jumped to 0.53 for $\triangle$[Hb], 0.54 for $\triangle[HbO_2]$ and 0.63 for *oxy* (P =0.07) when the two outliers were removed (shown in Figure 6.16 and given in Table D.7). The correlations were 0.6 (P =0.052) for $\triangle$[Hb], 0.48 for $\triangle[HbO_2]$ and 0.59 for *oxy* (P =0.056) at 75% MVC, all data included.

It can be put forward that sEMG parameters of MNF and MDF slopes could be good performance predictors, especially at low force levels (i.e. at 50% MVC level). The

cw-NIRS derived parameter of inflection duration promises to be a good performance indicator at both 50% MVC level and 75% MVC level.

6.5.2.5 Correlation Between sEMG and cw-NIRS Parameters. cw-NIRS is related mostly to energy related processes and factors while sEMG shows impairment of contractibility of muscle myofibrils reflected in surface motor unit action potentials. Oxy signal derived from cw-NIRS reflects balance between oxygen supply -which is affected by increased intramuscular pressure- and oxygen demand. MDF decrease is mostly explained by conduction velocity decrease in muscle myofibrils and synchronization of different motor units. Hence cw-NIRS is related mostly to energy related processes and factors while sEMG shows impairment of contractibility of muscle myofibrils reflected in surface motor unit action potentials. sEMG characteristics (i.e. power spectrum) depends on both muscle fiber membrane properties (which reflects peripheral properties) and timings of MU action potentials (which depend on CNS). Hence sEMG contains information about central and peripheral properties of neuromuscular system [215].

In our study, statistically significant correlations were found between sEMG and cw-NIRS parameters. The particular to note were the correlations between inflection durations and sEMG frequency parameters of MNF and MDF, especially at 50% MVC level. The number of statistically significant correlations were few for 75% MVC level and correlation values were lower. Based on these results, it can be claimed that change in sEMG parameters which contain both peripheral and central properties of neuromuscular system is also reflected to a degree in cw-NIRS parameters, especially at 50% MVC level.

Felici et al. [144] observed the deoxygenation change decreased whereas sEMG parameters of MDF fast phase slope had greatest difference between 60% MVC and 80% MVC and they state this finding shows recruitment of mostly type II B glycolytic fibers after 60% MVC. In contrast, they observed reduced MDF and CV change (especially in 40 to 80 % MVC exercise) in sinusoidal isometric exercise which they explained

by marginal and intermittent recruitment of mostly anaerobic MU's. Oxygen initial utilizations were nearly identical compared to static isometric exercise, however. In accordance with the explanation of Felici et al. [144], the highly valued statistically significant correlations observed in 50% MVC and their disappearance at 75% MVC level can be explained by recruitment of mostly aerobic fibers in 50% MVC level, but increased use of anaerobic fibers at higher force levels.

It can be claimed that (based on the experience with the data) MNF parameter did not change at high levels initially at the start of the experiment (i.e. initial 5-10 sec.) where *oxy* signal had a fast decline. Afterwards, MNF parameter has a decreasing trend whereas *oxy* signal change speed is much slower compared to the initial decline rate.

In the previous studies for sEMG and cw-NIRS relationship, Praagman et al. [54] found linear relationship between sEMG activity and oxygen consumption. In the study of Moalla et al. [145] which used submaximal isometric contraction at 50% MVC, a strong correlation was found between muscle oxygenation and MNF and a negative correlation was found between RMS and muscle oxygenation. These are in agreement with our findings.

6.5.2.6 Possible Applications. Fatigue is a complex phenomenon depending on many factors, besides muscle load, duty cycle and timing [216]. It can lead to injuries both in workplace, sports or daily life. Pain and suffering are indicators for us to avoid such consequences. There is a need for accurate biometrics to provide information about fatigue failure to prevent injuries.

During contraction, different/increasing number of motor units can be in action depending on the recruitment pattern. As the force production continues, ions' balances around the sarcolemma change, metabolic by-products increase, ATP reserves and ATP regeneration rate may decrease, O2 and energy supply could be hindered by blood flow occlusion because of increased intramuscular pressure, pH levels could decrease, Ca2+

release from sarcoplasmic reticulum could decrease, affinity of troponin to Ca2+ could decrease all leading to impairment of propagation of action potential. The problem in understanding fatigue is that any one of these factors in the chain can be a limiting factor in force/power production of the muscle. Identifying fatigue causing factors and to determine which one is most responsible for different tasks and experiment conditions are challenging tasks, and investigations are ongoing for achieving these aims. It is a challenging task to isolate a single step in this process chain, especially on humans [128]. It can be put forward that simultaneous use of NIRS and EMG could help us identification of possible fatigue causing factor(s) and isolate them from other possible ones.

Such studies will be important in exploiting the use of cw-NIRS and searching endurance and fatigue background mechanisms. These studies are valuable also in both performance monitoring of athletes, evaluation and planning of new training programs as well as in ergonomics to make work places healthier for employees. As it has been put forward by Sparto et al. [167], break times at work can be set to coincide with fatigue times with the knowledge acquired in studies like this study, increasing work safety. There is also need for biometrics that could be derived from cw-NIRS along with parameters from sEMG in physical medicine and rehabilitation to monitor the recovery of patients with objective parameters.

6.5.2.7 Limitations of the Study. The basic and biggest limitation in this study is that whether the probed muscle volumes by cw-NIRS and sEMG are the same or not. The difference in probed muscle volumes may have caused investigations of different muscle groups by the simultaneous use of cw-NIRS and sEMG. The flexor digitorum superficialis muscle is located by palpation during forth finger resisting against external resistance [140] and then sEMG and cw-NIRS electrodes are placed on top of the muscle next to each other. The silver/silver chloride (Ag/AgCl) sEMG electrode probes are trimmed from borders since space was needed. The center line between the two probes is on the muscle. However, this muscle is not so big, i.e. compared to biceps brachii muscle which is the muscle investigated in the study of Felici et al. [144] who used

simultaneously cw-NIRS and sEMG. The size of the muscle may have caused in some subjects crosstalk from other muscles since there are other muscle in the very close neighborhood.

Another point of consideration is skin blood flow effect. Influence of skin blood flow on NIRS measurements have been found to contribute less than 5% for a source-detector distance greater than 2 cm by Hampson et al. [217, 218]. In our study, the used source detector distance is 3.0 cm. In some studies however, it is proposed that skin blood flow contribution can be significant by Buono et al. [219] and Davis et al. [220]. These findings have been criticized by Quaresima and Ferrari [221] and Ferrari et al. [222] that in these studies source-detector distances are rather small (2.5 and 2.0 cm) which will decrease sensitivity, and they added that source-detector distances in new studies are longer. The common comment in all these studies is that more studies are needed to clarify the skin layer effect. It is also expected that local blood flow occlusion caused by high level of exercise contractions (50% and 75% MVC) employed in this thesis limits skin blood flow effect.

Another problem is that cw-NIRS has a quantification problem not for only absolute but also for concentration changes since partial path length in the muscle (or gray matter for brain measurements) is not known. Further complicating the problem, DPF changes during exercise. As stated in section 4.2.1 of chapter 4, Ferreira et al. [117] reports 5-10% decrease during forearm ischemia with and without maximal voluntary contraction and during brain hypoxic hypoxia [113]. Using another NIRS technique, Ferreira et al. [117] found that assumption of constant optical scattering leads to an overestimation of the changes in NIRS variables during exercise. DPF is also found to be varied by 4-10% during the occlusion through arm [20].

One method for alleviating this problem is dividing concentration changes to another value obtained for some known exercise. Obtaining this relative measure can be useful and adequate for the purposes of monitoring oxygenation levels compared to a known state level (or comparing levels before and after exercise) [153]. The normalization of NIRS signal to the range obtained by values starting from rest (0% MVC) to

50% MVC was the method in the study of Yamada et al. [223]. Hamaoka et al. also used normalization using maximal deoxygenation during exercise [224]. In our study, the amplitude values obtained at 75% MVC level were used to obtain normalized amplitude parameters.

7. CONCLUSION

The first aim of the thesis which was to provide a detailed analysis of the fat layer effect on continuous wave near infrared measurements. The analysis was carried out with Monte Carlo simulations for homogeneous skin-fat-layer layered heterogeneous tissue model. The system assumed was a two-wavelength system where the wavelengths are in 675 to 775 nm range for the first wavelength and in 825 to 900 nm range for the second wavelength and in total twenty four wavelength pairs have been used. We found an explicit effect that is mean values of the absolute underestimation errors and absolute crosstalks computed over considered wavelength pairs increase for a thicker fat layer. An interesting result was that means of absolute underestimation errors $E_{\mathrm{HbO_2},3.0,h_\mathrm{f}}$ and absolute crosstalks $C_{\mathrm{Hb}\rightarrow\mathrm{HbO_2},3.0,h_\mathrm{f}}$ over considered wavelength pairs have been found to be higher while the estimation errors for the concentration changes of the two chromophores are calculated to be closer for the ischemia protocol due to the crosstalks. We came to the conclusion that measurement of the fat thickness values and providing information about it should become a standard routine as suggested by van Beekvelt et al. [116] for the cw-NIRS measurements.

A correction algorithm is outlined for the homogeneous medium assumption based MBLL calculations with the use of wavelength dependent partial path length in the muscle layer derived with Monte-Carlo simulations instead of the used constant $d\times$DPF factor. The algorithm can be used with multi-wavelength cw-NIRS systems also. The usefulness of the proposed algorithm is shown in chapter 4 on the data of van Beekvelt et al. [21] in comparison with the correction curves of Niwayama et al. [105, 104].

Two detector cw-NIRS system is also analyzed and compared with 1-detector cw-NIRS system. The performance is promising but 'true' assumption of initial optical coefficients of the layers poses a challenge for the performance. Theoretical investigation of the two detector system with $\pm 5, 10$ and 15 % erroneous assumption of partial

pathlengths and mean pathlengths is done also, where the underestimation error of muscle layer increases with deviation from real partial path lengths (both increase and decrease of the used values from real partial path lengths increase the error). Detailed experimental studies are needed for applicability of the method and for the investigation of offered improvement.

Muscle measurements for muscle fatigue and endurance investigations have been done using the three measurement modalities of cw-NIRS, SEMG and force-time. The study aimed at deriving fatigue and endurance related biometrics for possible use in sports and ergonomics as well as investigation of physiology of fatigue. The study revealed some physiological processes related to fatigue. Blood flow impairment was observed through reduced oxygenation which impairs clearance of metabolic by-products and supply of oxygen and other metabolites needed for energy production, all leading to fatigue. cw-NIRS derived inflection duration gave promising results for endurance prediction. High correlation coefficients were obtained at both 50% and 75% MVC levels. sEMG frequency parameters of MNF and MDF had also moderate correlations at 50% MVC but not at 75% MVC level. A lot of statistical significant correlations were found between sEMG and cw-NIRS derived parameters, especially at 50% MVC level. These provided the evidence the link between muscle energetic processes monitored with cw-NIRS technique and neuromuscular characteristics reflected in sEMG technique during fatigue.

Other studies should be performed to validate the results obtained in the hand grip exercise study in this thesis. There are still few studies in the literature with simultaneous sEMG and cw-NIRS measurements. In the future studies, a bigger muscle having more volume should be selected for simultaneous cw-NIRS and sEMG measurements to eliminate to crosstalk from other muscles for sEMG and to ensure examination of same muscle property by both sEMG and cw-NIRS techniques.

In addition to understanding physiological processes underlying fatigue, these type of studies are valuable also in both performance monitoring of athletes, evaluation and planning of new training programs as well as in ergonomics to make work places

healthier for employees. There is also need for such biometrics in physical medicine and rehabilitation to monitor the recovery with objective parameters. This way, evaluation of physical training programs could be possible.

APPENDIX A. Calculating △[Hb] and △[HbO_2] from cw-NIRS Data

In cw NIRS, *resting state* of the tissue is measured by 30 seconds to 1 minute and detected light intensity is averaged to get resting level detected light intensity I^{λ}_{rest}. Time varying light intensity changes starting from resting duration are denoted as $OD^{\lambda}(t)$.

$$OD^{\lambda}_{rest} = ln\left(\frac{I^{\lambda}_{o}}{I^{\lambda}_{rest}}\right) = \left(\epsilon^{\lambda}_{1} \times c_{1,rest} + \epsilon^{\lambda}_{2} \times c_{2,rest} + ... + \epsilon^{\lambda}_{n} \times c_{n,rest}\right) \times r \times \mathrm{DPF}^{\lambda} + G^{\lambda} \quad \text{(A.1)}$$

$$OD^{\lambda}(t) = ln\left(\frac{I^{\lambda}_{o}}{I^{\lambda}(t)}\right) = \left(\epsilon^{\lambda}_{1} \times c_{1}(t) + \epsilon^{\lambda}_{2} \times c_{2}(t) + ... + \epsilon^{\lambda}_{n} \times c_{n}(t)\right) \times r \times \mathrm{DPF}^{\lambda} + G^{\lambda} \quad \text{(A.2)}$$

superscript λ indicates a particular wavelength, OD^{λ} is optical density, I_o is the intensity of the light sent into the tissue, ϵ^{λ}_{i} and c_i are the specific absorption coefficient (OD/cm/mM) and concentration (mM) of the chromophore i in the medium respectively, r (cm) is the minimal geometric distance between light source and detector, DPF^{λ} is the differential path length factor. DPF^{λ} equals mean optical path length of the photons ($<L^{\lambda}>$) divided by r. G^{λ} factor is due to medium geometry and light scattering.

Difference between the $OD^{\lambda}(t)$ and OD^{λ}_{rest} eliminates geometry dependent factor G^{λ} and is proportional to the concentration changes of absorbing chromophores;

$$OD^{\lambda}(t) - OD^{\lambda}_{rest} = ln\left(\frac{I^{\lambda}_{rest}}{I^{\lambda}(t)}\right) = \left(\epsilon^{\lambda}_{1} \times \triangle c_{1}(t) + \ldots + \epsilon^{\lambda}_{n} \times \triangle c_{n}(t)\right) \times r \times \mathrm{DPF}^{\lambda} \quad \text{(A.3)}$$

$$(\triangle c_{k}(t) = c_{k}(t) - c_{k,rest})$$

It is assumed that geometry and scattering dependent G^{λ} and DPF^{λ} factors does not change during measurement time. Moreover it is assumed that concentration changes are small.

In general constant DPF value is used instead of wavelength dependent DPF$^{\lambda}$ value. For a cw-NIRS system having two wavelengths of light at 730 nm and 850 nm, we have

$$OD^{850\ \mathrm{nm}}(t) = \left(\epsilon_{\mathrm{Hb}}^{850} \times \triangle c_{\mathrm{Hb}}(t) + \epsilon_{\mathrm{HbO_2}}^{850} \times \triangle c_{\mathrm{HbO_2}}(t)\right) \times r \times \mathrm{DPF} \tag{A.4}$$

$$OD^{730\ \mathrm{nm}}(t) = \left(\epsilon_{\mathrm{Hb}}^{730} \times \triangle c_{\mathrm{Hb}}(t) + \epsilon_{\mathrm{HbO_2}}^{730} \times \triangle c_{\mathrm{HbO_2}}(t)\right) \times r \times \mathrm{DPF} \tag{A.5}$$

This equations can be written in matrix form as;

$$\begin{bmatrix} OD^{850\ \mathrm{nm}}(t) \\ OD^{730\ \mathrm{nm}}(t) \end{bmatrix} = r \cdot \mathrm{DPF} \cdot \begin{bmatrix} \epsilon_{\mathrm{Hb}}^{850} & \epsilon_{\mathrm{HbO_2}}^{850} \\ \epsilon_{\mathrm{Hb}}^{730} & \epsilon_{\mathrm{HbO_2}}^{730} \end{bmatrix} \cdot \begin{bmatrix} \triangle c_{\mathrm{Hb}}(t) \\ \triangle c_{\mathrm{HbO_2}}(t) \end{bmatrix} \tag{A.6}$$

Using this matrix formulation, it is straightforward to get concentration changes of HbO_2 and Hb as given below;

$$\begin{bmatrix} \triangle c_{\mathrm{Hb}}(t) \\ \triangle c_{\mathrm{HbO_2}}(t) \end{bmatrix} = \frac{1}{r \cdot \mathrm{DPF}} \cdot \begin{bmatrix} \epsilon_{\mathrm{Hb}}^{850} & \epsilon_{\mathrm{HbO_2}}^{850} \\ \epsilon_{\mathrm{Hb}}^{730} & \epsilon_{\mathrm{HbO_2}}^{730} \end{bmatrix}^{-1} \begin{bmatrix} OD^{850\ \mathrm{nm}}(t) \\ OD^{730\ \mathrm{nm}}(t) \end{bmatrix} \tag{A.7}$$

$$\begin{bmatrix} \triangle c_{\mathrm{Hb}}(t) \\ \triangle c_{\mathrm{HbO_2}}(t) \end{bmatrix} = \frac{1}{r \cdot \mathrm{DPF} \cdot (\epsilon_{\mathrm{Hb}}^{850}.\epsilon_{\mathrm{HbO_2}}^{730} - \epsilon_{\mathrm{Hb}}^{730}.\epsilon_{\mathrm{HbO_2}}^{850})} \begin{bmatrix} \epsilon_{\mathrm{HbO_2}}^{730} & -\epsilon_{\mathrm{HbO_2}}^{850} \\ -\epsilon_{\mathrm{Hb}}^{730} & \epsilon_{\mathrm{Hb}}^{850} \end{bmatrix} \cdot \begin{bmatrix} OD^{850\ \mathrm{nm}}(t) \\ OD^{730\ \mathrm{nm}}(t) \end{bmatrix} \tag{A.8}$$

and finally;

$$\triangle c_{\mathrm{Hb}}(t) = \frac{\epsilon_{\mathrm{HbO_2}}^{730}.OD^{850\ \mathrm{nm}}(t) - \epsilon_{\mathrm{HbO_2}}^{850}.OD^{730\ \mathrm{nm}}(t)}{r \cdot \mathrm{DPF} \cdot (\epsilon_{\mathrm{Hb}}^{850}.\epsilon_{\mathrm{HbO_2}}^{730} - \epsilon_{\mathrm{Hb}}^{730}.\epsilon_{\mathrm{HbO_2}}^{850})} \tag{A.9}$$

$$\triangle c_{\mathrm{HbO_2}}(t) = \frac{-\epsilon_{\mathrm{Hb}}^{730}.OD^{850\ \mathrm{nm}}(t) + \epsilon_{\mathrm{Hb}}^{850}.OD^{730\ \mathrm{nm}}(t)}{r \cdot \mathrm{DPF} \cdot (\epsilon_{\mathrm{Hb}}^{850}.\epsilon_{\mathrm{HbO_2}}^{730} - \epsilon_{\mathrm{Hb}}^{730}.\epsilon_{\mathrm{HbO_2}}^{850})} \tag{A.10}$$

Using these two final Eq. A.9 and A.10, it is possible to calculate the concentration changes of HbO_2 and Hb relative to a resting baseline level.

APPENDIX B. EMGALY.1.2: Surface Electromyography Analysis Software with Graphical User Interface

Surface electromyography is the temporal and positional summation of muscle fiber action potentials triggered by the central nervous system. This signal contains valuable information about central nervous system, peripheral nerve-muscle system and related physiological processes. EMGALY.1.2 software [225] has been developed to assist researchers probing this signal for basic variables' investigations. The software has been developed in MATLAB environment for upgrade easiness and for the ease of the user a graphical user interface has been provided for execution of all commands. In its current form software use has been maximized for studies using isometric exercise protocols and enables investigation of the basic variables like root mean square, mean frequency (MNF) and median frequency (MDF). Time range for analysis can be labelled by the user and this selected range can be divided up to 20 segments for analysis. The program is still being improved for add-ons, shortcomings and possible errors.

B.1 General Properties

The program allows all operations to be executed using the GUI. With the help of a found program, it can read data in BIOPAC format. Non-overlapping window size, threshold value (percentage of peak RMS value) to be used for noise removal can be set by the user. Raw-EMG signal is high pass filtered by a 10 Hz 4^{th} order Butterworth filter. Besides a notch filter is added to the program for 50 Hz power line noise removal. EMG signal, MNF, MDF, and averaged instantaneous frequency (AIF) computed from analytic signal [226, 227] can be all shown in the GUI. For sEMG signal s, RMS signal in a time window is computed by;

$$RMS = \sqrt{\frac{1}{N}\sum_{i=1}^{N} s_i^2} \tag{B.1}$$

sEMG signal s having a power spectrum $P(f)$ in a time window, MNF and MDF are calculated using the equations below;

$$MNF = \frac{\int_0^\infty fP(f)df}{\int_0^\infty P(f)df} \tag{B.2}$$

$$\int_0^{MDF} P(f)df = \int_{MDF}^\infty P(f)df \tag{B.3}$$

$$\tag{B.4}$$

Analytic signal $z(t)$ for corresponding signal $s(t)$ is defined by the equation

$$z(t) = s(t) + jH[s(t)] \tag{B.5}$$

$$\text{with analytic phase } \phi(t) = arctan\left(\frac{H[s(t)]}{s(t)}\right) \tag{B.6}$$

$H[]$ defining the Hilbert operator defined by the equation;

$$H[s(t)] = \int_{-\infty}^\infty \frac{s(\tau)}{t-\tau}d\tau \tag{B.7}$$

Averaged instantaneous frequency is computed from the first derivative of the analytic phase function averaged over the computed time window.

$$AIF = \frac{1}{t_{final} - t_{initial}} \int_{t_{initial}}^{t_{final}} \phi'(t)d\tau \tag{B.8}$$

The time portion to be processed can be selected with the help of RMS signal or MNF signal shown on the graph. The program -if it can find- automatically labels exercise start and stop times for guiding the user. Slopes of least squares fittings for the mentioned parameters are found for the entire selected exercise time portion as well as initial and final values, % changes, slopes in %/seconds. Selected time range can be divided into up to 20 segments for segment based analysis. For each segment, same analysis is done as in selected whole time range. Results for the EMG signal analysis can be written to a file including results for whole selected time range and results for each time segment.

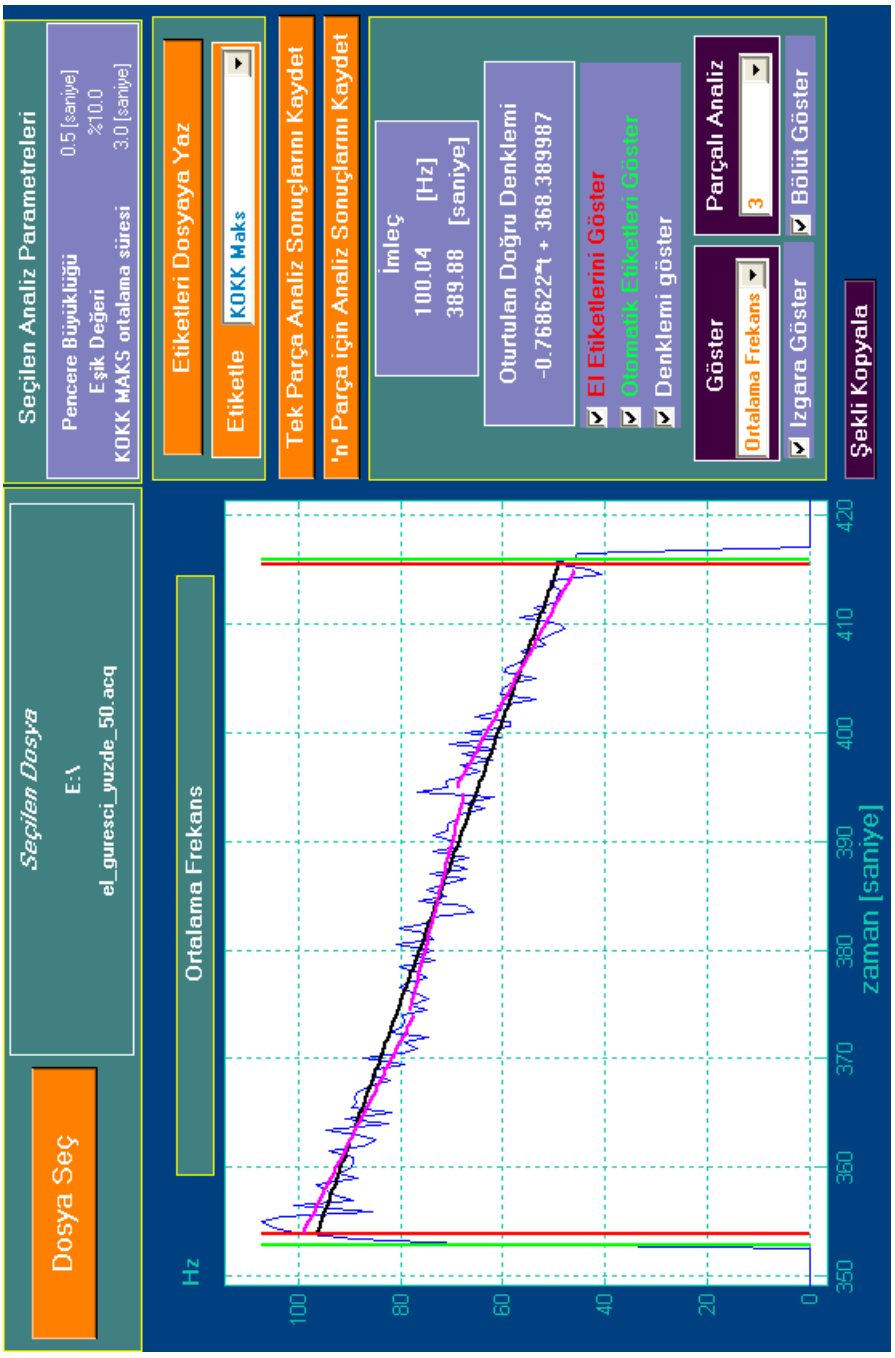

Figure B.1 Graphical user interface of the developed surface EMG signal analysis program

APPENDIX C. Partial Path Length Values in the Muscle Layer

Partial path length in the muscle $< L_{\mathrm{m}}^{\lambda} >$ computed with Monte Carlo simulations are given in this appendix for source-detector distances of r = 2.0, 2.5, 3.5, 4.0, 4.5, 5.0 cm and the ring thickness dr is 0.5 mm. Details of simulations are given in chapter 3. Skin thickness is taken as 1.4 mm.

Table C.1
Partial path length in the muscle $< L_{\mathrm{m}}^{\lambda} >$ [cm] computed with Monte Carlo simulation for $r = 2.0$ cm, h_s=1.4 mm

h_f [mm]	λ [nm]										
	675	**700**	**725**	**750**	**760**	**775**	**800**	**825**	**850**	**875**	**900**
0	7.4359	8.0783	8.1224	7.3983	7.1031	7.1656	7.1157	6.7403	6.3232	6.0389	5.8018
1	6.2549	6.9328	7.0240	6.3149	6.0680	6.1633	6.1498	5.8044	5.4216	5.1545	4.9298
2	4.9367	5.6866	5.7884	5.1115	4.8902	5.0421	5.0490	4.7183	4.3711	4.1260	3.9347
3	3.6492	4.3831	4.5081	3.8921	3.6998	3.8503	3.8920	3.5953	3.2775	3.0804	2.8959
4	2.5662	3.2162	3.3266	2.8139	2.6477	2.7883	2.8434	2.5961	2.3272	2.1667	2.0124
5	1.7657	2.2769	2.3698	1.9664	1.8419	1.9573	2.0016	1.8106	1.6099	1.4815	1.3538
6	1.2064	1.5953	1.6677	1.3611	1.2661	1.3587	1.3972	1.2606	1.1033	1.0095	0.8990
7	0.8257	1.1060	1.1672	0.9437	0.8747	0.9438	0.9704	0.8750	0.7657	0.6907	0.6022
8	0.5696	0.7739	0.8161	0.6559	0.6047	0.6598	0.6799	0.6124	0.5318	0.4772	0.4003
9	0.3946	0.5416	0.5718	0.4562	0.4216	0.4575	0.4773	0.4299	0.3713	0.3330	0.2714
10	0.2730	0.3780	0.3998	0.3200	0.2946	0.3245	0.3388	0.3029	0.2615	0.2328	0.1829
11	0.1896	0.2657	0.2805	0.2236	0.2053	0.2283	0.2401	0.2150	0.1858	0.1638	0.1234
12	0.1305	0.1853	0.1980	0.1567	0.1432	0.1608	0.1707	0.1522	0.1316	0.1159	0.0834
13	0.0906	0.1310	0.1399	0.1098	0.1000	0.1140	0.1215	0.1095	0.0938	0.0825	0.0567
14	0.0629	0.0919	0.0973	0.0764	0.0703	0.0805	0.0869	0.0774	0.0670	0.0578	0.0379

Table C.2
Partial path length in the muscle $< L_{\mathrm{m}}^{\lambda} >$ [cm] computed with Monte Carlo simulation for $r = 2.5$ cm, h_s=1.4 mm

h_f [mm]	λ [nm]										
	675	**700**	**725**	**750**	**760**	**775**	**800**	**825**	**850**	**875**	**900**
0	9.6207	10.4251	10.4696	9.5558	9.1678	9.2371	9.1908	8.7051	8.1741	7.8057	7.4901
1	8.3157	9.2303	9.2944	8.3789	8.0349	8.1786	8.1514	7.6931	7.2015	6.8336	6.5575
2	6.8217	7.8375	7.9653	7.0697	6.7733	6.9568	6.9620	6.5358	6.0451	5.7402	5.4879
3	5.3284	6.3746	6.5087	5.6574	5.4106	5.6077	5.6399	5.2536	4.8163	4.5369	4.3116
4	3.9389	4.9193	5.0529	4.3096	4.0566	4.2968	4.3610	3.9986	3.6372	3.3809	3.1878
5	2.8248	3.6678	3.8101	3.1794	2.9740	3.1612	3.2266	2.9389	2.6090	2.4226	2.2708
6	1.9920	2.6732	2.8003	2.2858	2.1205	2.2896	2.3521	2.1099	1.8635	1.7117	1.5746
7	1.4036	1.9195	2.0228	1.6257	1.5122	1.6352	1.6859	1.5047	1.3247	1.2085	1.0821
8	0.9968	1.3803	1.4567	1.1608	1.0798	1.1741	1.2063	1.0865	0.9445	0.8485	0.7464
9	0.7142	0.9863	1.0548	0.8294	0.7688	0.8378	0.8679	0.7700	0.6712	0.6064	0.5155
10	0.5040	0.7083	0.7543	0.5974	0.5489	0.6034	0.6301	0.5613	0.4836	0.4324	0.3562
11	0.3611	0.5115	0.5426	0.4264	0.3922	0.4362	0.4546	0.4060	0.3497	0.3107	0.2481
12	0.2565	0.3647	0.3928	0.3067	0.2811	0.3142	0.3320	0.2951	0.2546	0.2252	0.1723
13	0.1823	0.2625	0.2825	0.2208	0.2024	0.2269	0.2428	0.2150	0.1845	0.1623	0.1196
14	0.1305	0.1886	0.2032	0.1585	0.1448	0.1646	0.1749	0.1554	0.1340	0.1181	0.0832

Table C.3
Partial path length in the muscle $< L_{\mathrm{m}}^{\lambda} >$ [cm] computed with Monte Carlo simulation for $r = 3.0$ cm, h_s=1.4 mm.

h_f [mm]	λ [nm]										
	675	**700**	**725**	**750**	**760**	**775**	**800**	**825**	**850**	**875**	**900**
0	11.8019	12.8202	12.8908	11.7408	11.2356	11.3898	11.2421	10.6893	10.0431	9.5826	9.1817
1	10.4172	11.5008	11.6130	10.5124	10.0839	10.2073	10.1655	9.6417	8.9937	8.5702	8.2386
2	8.8246	10.0277	10.1950	9.0822	8.7258	8.8887	8.8957	8.3688	7.7735	7.3695	7.0746
3	7.1098	8.3950	8.5939	7.5313	7.1379	7.4334	7.5046	7.0028	6.4326	6.0838	5.7962
4	5.3838	6.7597	6.9388	5.9750	5.6475	5.9222	5.9785	5.5498	5.0481	4.7154	4.5145
5	4.0148	5.1969	5.4248	4.5494	4.3069	4.5351	4.5929	4.2102	3.7943	3.5170	3.3354
6	2.9189	3.9227	4.1298	3.3721	3.1310	3.3832	3.4754	3.1278	2.7778	2.5414	2.4124
7	2.1057	2.9080	3.0880	2.4791	2.3013	2.4983	2.5685	2.3084	2.0234	1.8392	1.6885
8	1.5248	2.1409	2.2839	1.8123	1.6688	1.8297	1.8907	1.6866	1.4695	1.3229	1.2073
9	1.1118	1.5750	1.6810	1.3163	1.2220	1.3327	1.3911	1.2281	1.0724	0.9593	0.8431
10	0.8119	1.1576	1.2383	0.9658	0.8908	0.9851	1.0235	0.9106	0.7784	0.6999	0.6006
11	0.5873	0.8452	0.9091	0.7027	0.6469	0.7250	0.7514	0.6727	0.5768	0.5141	0.4244
12	0.4326	0.6284	0.6675	0.5212	0.4793	0.5366	0.5604	0.4983	0.4256	0.3781	0.3040
13	0.3156	0.4570	0.4923	0.3857	0.3492	0.3921	0.4178	0.3665	0.3155	0.2750	0.2166
14	0.2291	0.3326	0.3597	0.2785	0.2559	0.2877	0.3070	0.2725	0.2331	0.2032	0.1544
15	0.1675	0.2454	0.2639	0.2063	0.1874	0.2130	0.2282	0.2023	0.1739	0.1510	0.1081

Table C.4
Partial path length in the muscle $<L_{\mathrm{m}}^{\lambda}>$ [cm] computed with Monte Carlo simulation for $r = 3.5$ cm, h_s=1.4 mm

h_f [mm]	λ [nm]										
	675	**700**	**725**	**750**	**760**	**775**	**800**	**825**	**850**	**875**	**900**
0	13.9483	15.2526	15.3021	13.9235	13.3977	13.4308	13.4249	12.6147	11.8679	11.3190	10.8722
1	12.5090	13.8303	14.0044	12.6992	12.1209	12.2572	12.2463	11.5076	10.7971	10.3327	9.8610
2	10.7987	12.2998	12.5017	11.1185	10.6456	10.9068	10.8562	10.2620	9.4779	9.0313	8.6538
3	8.9817	10.5032	10.7398	9.4394	8.9801	9.3406	9.3411	8.7257	8.0617	7.5981	7.3766
4	7.0066	8.6542	8.9242	7.6833	7.3021	7.6424	7.7615	7.1911	6.4885	6.1427	5.8953
5	5.3538	6.8920	7.2170	6.0137	5.6769	6.0574	6.0757	5.6164	5.0206	4.6925	4.5177
6	3.9401	5.3121	5.6258	4.5695	4.2837	4.6228	4.7107	4.2893	3.8072	3.5190	3.3110
7	2.8902	4.0477	4.3254	3.4697	3.2022	3.4862	3.5704	3.2266	2.8236	2.5715	2.4508
8	2.1258	3.0450	3.2406	2.5819	2.3730	2.5958	2.6857	2.3928	2.0801	1.8898	1.7580
9	1.5901	2.2993	2.4595	1.9220	1.7541	1.9345	2.0094	1.7871	1.5540	1.3873	1.2687
10	1.1903	1.7108	1.8435	1.4313	1.3192	1.4588	1.5213	1.3326	1.1488	1.0398	0.9180
11	0.8658	1.2764	1.3854	1.0675	0.9853	1.0888	1.1369	0.9972	0.8606	0.7720	0.6645
12	0.6530	0.9591	1.0227	0.8039	0.7238	0.8175	0.8502	0.7519	0.6448	0.5720	0.4827
13	0.4835	0.7131	0.7795	0.6002	0.5475	0.6103	0.6391	0.5691	0.4860	0.4257	0.3520
14	0.3610	0.5375	0.5810	0.4409	0.4115	0.4543	0.4818	0.4291	0.3690	0.3230	0.2561

Table C.5
Partial path length in the muscle $< L_{\mathrm{m}}^{\lambda} >$ [cm] computed with Monte Carlo simulation for $r = 4.0$ cm, h_s=1.4 mm

h_f [mm]	λ [nm]										
	675	**700**	**725**	**750**	**760**	**775**	**800**	**825**	**850**	**875**	**900**
0	16.1171	17.6592	17.7316	16.1629	15.4399	15.5045	15.5053	14.6579	13.7585	13.1428	12.6929
1	14.9069	16.1722	16.4122	14.7328	14.2148	14.2427	14.2804	13.4278	12.5336	12.0718	11.5083
2	12.8656	14.6668	14.7276	13.2229	12.6721	12.9507	12.8938	12.0405	11.2573	10.7783	10.2114
3	10.7469	12.6798	12.9896	11.3488	10.7070	11.0989	11.2616	10.4345	9.7501	9.1880	8.8460
4	8.5532	10.5739	11.0017	9.3501	8.9648	9.4140	9.4616	8.7984	8.0219	7.5566	7.3680
5	6.7670	8.6325	9.0600	7.5861	7.1841	7.4900	7.7815	7.0307	6.4522	5.9288	5.7266
6	5.0362	6.8797	7.1878	5.9577	5.5425	5.9341	6.1714	5.5162	4.8366	4.5972	4.3729
7	3.7652	5.2704	5.6391	4.5685	4.1713	4.5742	4.7577	4.2596	3.7707	3.4169	3.2397
8	2.8054	4.0801	4.3912	3.4441	3.2328	3.4897	3.5995	3.1985	2.7962	2.5190	2.4302
9	2.1109	3.1418	3.3658	2.6055	2.3696	2.6483	2.7529	2.4436	2.0798	1.8648	1.7525
10	1.6182	2.4143	2.5544	1.9763	1.8177	1.9974	2.0835	1.8158	1.5715	1.4122	1.3123
11	1.2064	1.8283	1.9479	1.4828	1.3894	1.4857	1.5768	1.3844	1.1809	1.0757	0.9421
12	0.9153	1.3618	1.5148	1.1428	1.0273	1.1436	1.2044	1.0616	0.8902	0.8077	0.6961
13	0.6932	1.0304	1.1138	0.8676	0.7780	0.8794	0.9166	0.8000	0.6860	0.6057	0.5134
14	0.5251	0.7926	0.8491	0.6578	0.5961	0.6671	0.6958	0.6213	0.5299	0.4706	0.3817

Table C.6
Partial path length in the muscle $<L_{\mathrm{m}}^{\lambda}>$ [cm] computed with Monte Carlo simulation for $r = 4.5$ cm, h_s=1.4 mm

h_f [mm]	λ [nm]										
	675	**700**	**725**	**750**	**760**	**775**	**800**	**825**	**850**	**875**	**900**
0	18.2704	19.9040	20.1439	18.2218	17.8608	17.7363	17.7002	16.6119	15.6425	14.8769	14.2769
1	16.9025	18.3621	18.6710	16.8578	16.0909	16.4810	16.4187	15.4687	14.4567	13.7897	13.1883
2	14.9224	16.6965	17.1888	15.0491	14.7829	14.9355	14.9404	14.0446	13.1379	12.2465	11.8508
3	12.5760	14.8048	15.2616	13.3226	12.8062	13.1645	13.1990	12.3176	11.4867	10.9349	10.5407
4	10.4151	12.6256	12.9437	11.2212	10.8071	11.2662	11.2029	10.5809	9.5982	8.9850	8.7036
5	7.9029	10.4165	10.9285	9.1775	8.6802	9.2746	9.4058	8.7203	7.6445	7.3084	7.1315
6	6.1632	8.5508	8.8877	7.2683	6.8955	7.3097	7.5418	6.8635	5.8253	5.5708	5.4484
7	4.6392	6.6324	7.0753	5.7081	5.2955	5.6667	5.9030	5.3280	4.6975	4.3675	4.2086
8	3.5368	5.2587	5.4943	4.3082	3.9162	4.4524	4.7590	4.0642	3.5267	3.2116	3.0772
9	2.7443	3.9387	4.3042	3.3352	3.1325	3.5156	3.5940	3.1732	2.7088	2.3849	2.3297
10	2.0751	3.1225	3.2476	2.5968	2.3982	2.6134	2.7271	2.3721	2.0305	1.8293	1.7171
11	1.5778	2.3353	2.5782	1.9842	1.7865	2.0437	2.0611	1.8750	1.5732	1.4131	1.2917
12	1.2148	1.8460	2.0129	1.5167	1.4099	1.5286	1.6166	1.4422	1.2112	1.0575	0.9538
13	0.9447	1.4246	1.5347	1.1698	1.0839	1.1893	1.2451	1.0853	0.9241	0.8204	0.7165
14	0.6922	1.0705	1.1635	0.8772	0.8271	0.9372	0.9688	0.8427	0.7233	0.6322	0.5517

Table C.7
Partial path length in the muscle $< L_{\mathrm{m}}^{\lambda} >$ [cm] computed with Monte Carlo simulation for $r = 5.0$ cm, h_s=1.4 mm

h_f [mm]	λ [nm]										
	675	**700**	**725**	**750**	**760**	**775**	**800**	**825**	**850**	**875**	**900**
0	20.6940	22.4342	22.6701	20.4096	19.7758	19.9135	19.6581	18.7463	17.6009	16.8564	16.4818
1	19.0485	20.6201	20.8992	18.9568	18.0695	18.6793	18.3497	17.2860	16.4441	15.4871	15.1093
2	16.5214	19.1407	19.4082	17.3650	16.5283	16.7186	16.8454	15.8521	14.9055	13.9017	13.2110
3	14.8208	17.1420	17.2003	15.2439	14.2494	15.1071	15.0673	14.2226	13.0266	12.2567	11.7455
4	11.9020	14.5110	15.3924	13.0527	12.5473	12.6088	13.4191	12.4367	11.1338	10.8076	10.4438
5	9.7019	12.4417	13.2401	10.9064	10.0748	11.0400	11.1048	9.8739	9.2713	8.6145	8.5557
6	6.8780	9.9441	10.6275	8.6590	8.3039	8.9120	9.2527	8.2484	7.0796	6.4842	6.7824
7	5.7919	8.1485	8.5307	7.0368	6.4699	6.9464	7.3310	6.3722	5.5237	5.1082	5.0568
8	4.3773	6.3835	6.9806	5.3334	5.0666	5.3893	5.5717	4.9358	4.2585	4.0027	3.9626
9	3.4037	4.9500	5.4795	4.1986	3.8481	4.2017	4.3292	3.8955	3.3851	3.0854	3.0356
10	2.6655	3.7883	4.1091	3.2071	2.9129	3.2825	3.4313	2.9224	2.5858	2.2860	2.1695
11	2.0091	2.9651	3.3048	2.5175	2.2989	2.5156	2.6941	2.3346	1.9731	1.7651	1.6874
12	1.5500	2.4204	2.5605	1.9200	1.8019	1.9886	2.0928	1.7977	1.5648	1.3714	1.2552
13	1.2091	1.8199	2.0602	1.5257	1.3582	1.5427	1.6222	1.4438	1.1945	1.0590	0.9727
14	0.9688	1.4421	1.6284	1.1881	1.0576	1.2272	1.2557	1.1159	0.9393	0.8289	0.7329

APPENDIX D. Individual Parameter Values for Hand Grip Exercise

Table D.1
Physical characteristics of the subjects

Subject No.	Age [years]	Height [m.]	Weight [kg.]	BMI [kg./m^2]	Fat thickness on FDS muscle [mm.]	Maximum grip force [kg.]
1	19	1.76	73.0	23.6	2.00	47
2	22	1.85	69.0	20.2	1.75	54
3	21	1.82	75.0	22.6	2.00	56
4	24	1.96	105.0	27.3	4.00	65
5	23	1.90	74.0	20.5	1.50	52
6	21	1.87	72.5	20.7	2.50	48
7	30	1.74	75.0	24.8	1.50	52
8	23	1.78	75.0	23.7	2.00	51
9	18	1.76	73.0	23.6	2.00	47
10	24	1.84	74.0	21.9	1.50	57
11	24	1.81	82.0	25.0	2.00	45
μ	22.6	1.8	77.0	23.1	2.1	52.2
σ	3.2	0.1	9.8	2.2	0.7	5.9

Table D.2
sEMG parameters of 50% MVC hand grip exercise for each subject

		RMS		Mean Frequency			Median Frequency		
Subject No.	Duration [s.]	% change	Slope [%/s.]	% change	Slope [Hz/s.]	Slope [%/s.]	% change	Slope [Hz/s.]	Slope [%/s.]
1	61.0	-1.2	0.0	-25.0	-0.6	-0.4	-25.4	-0.5	-0.4
2	86.5	15.7	0.2	-52.6	-0.6	-0.6	-51.3	-0.5	-0.6
3	102.5	197.2	1.9	-33.1	-0.3	-0.3	-34.6	-0.3	-0.3
4	62.5	9.8	0.2	-38.4	-0.5	-0.6	-37.6	-0.4	-0.6
5	96.5	414.1	4.3	-8.8	-0.1	-0.1	-1.4	0.0	0.0
6	76.0	52.5	0.7	-73.1	-1.3	-1.0	-74.1	-1.1	-1.0
7	73.0	-10.3	-0.1	-39.8	-0.8	-0.5	-37.7	-0.6	-0.5
8	52.0	78.0	1.5	-33.8	-0.7	-0.7	-31.6	-0.6	-0.6
9	100.5	28.3	0.3	-12.3	-0.1	-0.1	-13.6	-0.1	-0.1
10	82.0	103.5	1.3	-32.9	-0.3	-0.4	-31.3	-0.3	-0.4
11	121.0	114.2	0.9	-32.4	-0.2	-0.3	-37.6	-0.2	-0.3
μ	83.0	91.1	1.0	-34.8	-0.5	-0.5	-34.2	-0.4	-0.4
σ	20.8	123.7	1.3	17.6	0.3	0.3	18.7	0.3	0.3

Table D.3
sEMG parameters of 75% MVC hand grip exercise for each subject ($^*P \leq 3 \times 10^{-4}$, paired t-test results for mean difference compared with 50% MVC exercise values)

		RMS		Mean Frequency			Median Frequency		
Subject No.	Duration [s.]	% change	Slope [%/s.]	% change	Slope [Hz/s.]	Slope [%/s.]	% change	Slope [Hz/s.]	Slope [%/s.]
1	39.0	-14.2	-0.4	-33.5	-1.0	-0.9	-30.9	-0.8	-0.8
2	41.5	43.2	1.1	-51.6	-1.3	-1.3	-49.6	-0.9	-1.2
3	42.5	25.2	0.6	-36.2	-1.0	-0.9	-37.2	-0.8	-0.9
4	30.5	39.1	1.3	-18.0	-0.4	-0.6	-20.1	-0.5	-0.7
5	45.0	117.9	2.7	-35.3	-0.9	-0.8	-36.8	-0.9	-0.8
6	31.5	42.1	1.4	-43.6	-1.4	-1.4	-41.0	-1.1	-1.3
7	33.5	11.3	0.3	-35.4	-1.4	-1.1	-38.1	-1.3	-1.2
8	38.5	59.4	1.6	-42.8	-1.2	-1.1	-41.7	-1.0	-1.1
9	41.0	95.7	2.4	-34.9	-0.8	-0.9	-33.6	-0.7	-0.8
10	33.5	55.6	1.7	-30.5	-0.7	-0.9	-23.7	-0.5	-0.7
11	37.5	41.6	1.1	-33.8	-0.8	-0.9	-33.2	-0.6	-0.9
μ	**37.6***	47.0	1.2	-36.0	**-1.0***	**-1.0***	-35.1	**-0.8***	**-0.9***
σ	4.8	36.4	0.9	8.4	0.3	0.2	8.3	0.3	0.2
P-value	1×10^{-5}				8×10^{-5}	8×10^{-6}		3×10^{-4}	1×10^{-5}

Table D.4
NIRS parameter values for 50% hand grip isometric exercise level (No. is subject number)

No.	△Hb						△HbO_2						Oxy					
	ΔR_f	$\frac{\Delta R_f}{\Delta R_f^{75}}$	t_n	ΔR_n	$\frac{\Delta R_n}{\Delta R_n^{75}}$	m	ΔR_f	$\frac{\Delta R_f}{\Delta R_f^{75}}$	t_n	ΔR_n	$\frac{\Delta R_n}{\Delta R_n^{75}}$	m	ΔR_f	$\frac{\Delta R_f}{\Delta R_f^{75}}$	t_n	ΔR_n	$\frac{\Delta R_n}{\Delta R_n^{75}}$	m
	[a.u.]	[n.u.]	[s.]	[a.u.]	[n.u.]	[a.u.]	[a.u.]	[n.u.]	[s.]	[a.u.]	[n.u.]	[a.u.]	[a.u.]	[n.u.]	[s.]	[a.u.]	[n.u.]	[a.u.]
1	17.9	1.0	9.9	8.7	1.2	1.2	-13.9	0.9	9.8	-10.1	1.2	-1.3	-29.6	0.9	10.0	-18.5	1.2	-2.3
2	13.0	3.2	33.7	8.0	3.2	0.2	-12.6	1.6	38.7	-9.8	1.7	-0.2	-25.2	2.7	41.7	-18.9	2.7	-0.4
3	23.9	1.2	13.3	19.1	1.0	1.9	-21.1	1.0	12.1	-16.0	0.9	-2.0	-41.0	1.0	13.0	-33.8	0.9	-3.7
4	12.6	0.7	14.3	11.2	0.8	0.9	-14.3	0.9	14.5	-10.9	1.1	-0.8	-25.5	1.0	13.5	-20.7	1.1	-1.8
5	14.0	1.0	28.0	10.5	1.0	0.7	-16.8	1.0	35.6	-9.3	0.9	-0.4	-31.0	1.1	30.3	-18.8	0.8	-1.0
6	16.9	1.3	6.8	11.0	1.5	1.8	-15.8	1.5	7.0	-13.6	1.5	-1.7	-28.7	1.3	6.9	-22.9	1.5	-3.5
7	13.1	0.9	9.9	7.4	0.9	1.0	-9.4	0.5	8.6	-8.5	0.7	-0.9	-20.6	0.7	9.6	-14.9	0.8	-1.8
8	13.3	1.0	9.6	8.0	1.0	0.9	-14.8	0.9	9.4	-8.4	0.7	-0.8	-26.9	1.0	9.7	-15.3	0.8	-1.7
9	15.5	0.8	16.0	5.9	0.5	0.5	-11.9	0.8	12.1	-3.5	0.3	-0.4	-26.0	0.9	14.0	-9.1	0.4	-1.0
10	21.9	1.3	12.6	15.9	1.1	1.7	-14.7	0.7	11.9	-12.8	0.8	-1.5	-35.7	0.9	12.4	-28.9	1.0	-3.2
11	12.6	0.8	13.5	8.7	0.6	1.1	-13.7	0.8	15.6	-12.2	0.8	-1.1	-24.6	0.8	14.9	-20.8	0.7	-1.9
μ	15.9	1.2	15.2	10.4	1.2	1.1	-14.4	1.0	15.9	-10.5	1.0	-1.0	-28.6	1.1	16.0	-20.2	1.1	-2.0
σ	3.9	0.7	8.2	3.9	0.7	0.5	3.0	0.3	10.8	3.3	0.4	0.6	5.7	0.5	10.5	6.7	0.6	1.1

Table D.5
NIRS parameter values for 75% hand grip isometric exercise level (* $P<0.05$, ** $P \leq 0.01$, paired t-test results for mean difference compared with 50% MVC exercise values)

Subject	△Hb				△HbO_2				Oxy			
No.	ΔR_f	t_n	ΔR_n	m	ΔR_f	t_n	ΔR_n	m	ΔR_f	t_n	ΔR_n	m
1	17.7	8.7	7.3	1.4	-15.1	9.7	-8.2	-1.0	-32.0	9.7	-16.0	-2.0
2	4.0	12.6	2.5	0.3	-7.6	12.8	-5.8	-0.4	-9.5	13.7	-6.9	-0.6
3	20.4	8.7	18.6	2.9	-20.9	8.7	-18.3	-2.7	-40.8	8.7	-36.5	-5.6
4	17.0	9.0	13.7	0.9	-15.6	9.1	-10.0	-1.4	-25.1	8.6	-19.2	-2.5
5	13.5	12.2	10.6	1.1	-16.4	11.4	-10.3	-1.5	-29.0	13.1	-22.1	-2.2
6	12.8	6.0	7.5	1.6	-10.4	6.2	-8.8	-1.3	-21.8	6.4	-15.7	-3.0
7	14.6	8.2	7.9	1.3	-17.7	8.8	-12.2	-1.4	-30.0	8.5	-19.0	-2.5
8	12.8	5.9	8.1	1.6	-17.0	5.3	-12.9	-2.3	-27.8	5.4	-19.8	-4.0
9	18.2	10.4	12.9	2.1	-15.0	10.0	-12.1	-2.0	-29.6	10.0	-24.3	-4.1
10	17.0	8.3	14.0	2.3	-21.0	9.2	-16.8	-2.2	-37.9	8.7	-30.4	-4.5
11	15.7	10.4	14.0	2.3	-16.8	10.5	-14.6	-2.0	-32.1	10.5	-28.5	-4.0
μ	14.9	**9.1****	10.6	**1.6****	-15.8	**9.2***	-11.8	**-1.6****	-28.7	**9.4***	-21.7	**-3.2****
σ	4.3	2.2	4.5	0.7	4.0	2.1	3.7	0.7	8.3	2.5	8.1	1.4
P-value		0.010		0.009		0.038		0.008		0.026		0.006

Table D.6
Correlation coefficients between sEMG parameters and NIRS parameters for 50% hand grip isometric exercise level (bold font indicates $P < 0.05$)

				RMS		Mean Frequency			Median Frequency		
			Duration [s.]	% Change	Slope [%/s.]	% Change	Slope [Hz/s.]	Slope [%/s.]	% Change	Slope [Hz/s.]	Slope [%/s.]
Duration		[s.]	1	0.44	0.30	0.26	0.59	**0.60**	0.18	0.56	0.55
$\triangle$[Hb]	ΔR_f	[a.u.]	0.13	0.17	0.16	0.02	0.11	0.14	0.00	0.03	0.10
	$\frac{\Delta R_f}{\Delta R_f^{75}}$	[n.u.]	0.04	-0.13	-0.13	-0.44	-0.19	-0.27	-0.39	-0.20	-0.28
	t_n	[s.]	0.33	0.38	0.35	0.21	0.41	0.34	0.27	0.46	0.36
	ΔR_n	[a.u.]	0.17	0.38	0.36	-0.09	0.13	0.03	-0.09	0.07	0.01
	$\frac{\Delta R_n}{\Delta R_n^{75}}$	[n.u.]	-0.13	-0.17	-0.16	-0.52	-0.35	-0.40	-0.46	-0.35	-0.41
	m	[a.u.]	0.00	0.09	0.09	-0.32	-0.27	-0.25	-0.35	-0.34	-0.28
$\triangle$[HbO_2]	ΔR_f	[a.u.]	-0.21	**-0.62**	**-0.61**	-0.03	-0.16	-0.07	-0.03	-0.11	-0.10
	$\frac{\Delta R_f}{\Delta R_f^{75}}$	[n.u.]	0.00	0.02	0.03	-0.59	-0.41	-0.49	-0.55	-0.43	-0.48
	t_n	[s.]	0.31	0.47	0.43	0.17	0.35	0.28	0.24	0.41	0.32
	ΔR_n	[a.u.]	-0.14	-0.21	-0.17	0.47	0.22	0.31	0.49	0.28	0.34
	$\frac{\Delta R_n}{\Delta R_n^{75}}$	[n.u.]	-0.22	-0.14	-0.15	**-0.69**	-0.55	**-0.60**	**-0.65**	-0.55	**-0.62**
	m	[a.u.]	-0.01	0.01	0.03	0.34	0.29	0.26	0.39	0.37	0.30
oxy	ΔR_f	[a.u.]	-0.20	-0.50	-0.49	-0.14	-0.27	-0.22	-0.14	-0.20	-0.22
	$\frac{\Delta R_f}{\Delta R_f^{75}}$	[n.u.]	0.01	-0.10	-0.09	-0.43	-0.20	-0.30	-0.38	-0.20	-0.30
	t_n	[s.]	0.30	0.33	0.29	0.10	0.31	0.24	0.16	0.36	0.26
	ΔR_n	[a.u.]	-0.20	-0.30	-0.27	0.27	-0.01	0.10	0.28	0.05	0.13
	$\frac{\Delta R_n}{\Delta R_n^{75}}$	[n.u.]	-0.18	-0.26	-0.26	**-0.62**	-0.42	-0.50	-0.57	-0.43	-0.52
	m	[a.u.]	0.05	-0.01	0.00	0.36	0.31	0.30	0.40	0.39	0.34

Table D.7
Correlation coefficients between sEMG parameters and NIRS parameters for 50% hand grip isometric exercise level when two outliers (subjects 2 and 5) are excluded (bold font indicates $P < 0.05$)

				RMS		Mean Frequency			Median Frequency		
			Duration [s.]	% Change	Slope [%/s.]	% Change	Slope [Hz/s.]	Slope [%/s.]	% Change	Slope [Hz/s.]	Slope [%/s.]
Duration		[s.]	1.00	0.56	0.26	0.22	0.57	0.59	0.10	0.54	0.55
$\triangle$[Hb]	ΔR_f	[a.u.]	0.20	0.61	0.55	0.03	0.17	0.21	0.03	0.11	0.18
	$\frac{\Delta R_f}{\Delta R_f^{75}}$	[n.u.]	-0.06	0.46	0.55	-0.48	-0.38	-0.36	-0.46	-0.45	-0.37
	t_n	[s.]	0.53	0.21	0.05	**0.73**	**0.92**	**0.81**	**0.68**	**0.92**	**0.80**
	ΔR_n	[a.u.]	0.19	**0.74**	**0.67**	-0.19	0.13	0.00	-0.19	0.07	-0.03
	$\frac{\Delta R_n}{\Delta R_n^{75}}$	[n.u.]	-0.50	0.01	0.14	**-0.72**	**-0.78**	**-0.73**	**-0.67**	**-0.82**	**-0.75**
	m	[a.u.]	0.12	0.60	0.54	-0.56	-0.30	-0.32	-0.57	-0.37	-0.37
$\triangle$[HbO_2]	ΔR_f	[a.u.]	-0.18	**-0.80**	**-0.78**	0.19	-0.06	0.09	0.23	0.03	0.09
	$\frac{\Delta R_f}{\Delta R_f^{75}}$	[n.u.]	-0.08	0.18	0.22	**-0.67**	-0.56	-0.63	**-0.71**	-0.63	-0.64
	t_n	[s.]	0.54	0.31	0.13	0.50	**0.81**	0.59	0.43	**0.80**	0.58
	ΔR_n	[a.u.]	-0.17	-0.64	-0.54	0.54	0.19	0.31	0.57	0.26	0.35
	$\frac{\Delta R_n}{\Delta R_n^{75}}$	[n.u.]	-0.34	-0.07	-0.07	**-0.76**	**-0.69**	**-0.71**	**-0.76**	**-0.72**	**-0.76**
	m	[a.u.]	-0.16	-0.62	-0.53	0.49	0.25	0.25	0.51	0.32	0.29
oxy	ΔR_f	[a.u.]	-0.19	**-0.75**	**-0.72**	-0.03	-0.23	-0.16	-0.02	-0.15	-0.15
	$\frac{\Delta R_f}{\Delta R_f^{75}}$	[n.u.]	-0.23	0.16	0.29	-0.66	-0.56	**-0.68**	-0.66	-0.63	**-0.69**
	t_n	[s.]	0.63	0.34	0.14	**0.68**	**0.93**	**0.79**	0.61	**0.93**	**0.78**
	ΔR_n	[a.u.]	-0.22	**-0.74**	-0.64	0.32	-0.04	0.09	0.33	0.03	0.13
	$\frac{\Delta R_n}{\Delta R_n^{75}}$	[n.u.]	-0.47	-0.11	-0.06	**-0.77**	**-0.74**	**-0.76**	**-0.75**	**-0.76**	**-0.81**
	m	[a.u.]	-0.08	-0.58	-0.54	0.56	0.31	0.34	0.57	0.39	0.38

Table D.8
Correlation coefficients between sEMG parameters and NIRS parameters for 75% hand grip isometric exercise level (bold font indicates $P<0.05$)

				RMS		Mean Frequency			Median Frequency		
			Duration [s.]	% Change	Slope [%/s.]	% Change	Slope [Hz/s.]	Slope [%/s.]	% Change	Slope [Hz/s.]	Slope [%/s.]
Duration		[s.]	1.00	0.40	0.23	-0.40	-0.09	0.07	-0.45	-0.04	0.13
$\triangle$[Hb]	ΔR_f	[a.u.]	-0.11	-0.12	-0.12	**0.71**	0.53	**0.65**	**0.70**	0.39	**0.63**
	t_n	[s.]	0.60	0.38	0.27	-0.06	0.25	0.26	-0.12	0.28	0.29
	ΔR_n	[a.u.]	0.01	0.15	0.16	**0.63**	**0.66**	**0.67**	**0.61**	0.58	**0.64**
	m	[a.u.]	0.06	-0.01	0.00	0.20	0.21	0.20	0.27	0.28	0.29
$\triangle$[HbO_2]	ΔR_f	[a.u.]	0.00	0.01	0.03	-0.55	-0.41	-0.59	-0.55	-0.28	-0.55
	t_n	[s.]	0.48	0.18	0.08	-0.01	0.25	0.24	-0.03	0.31	0.30
	ΔR_n	[a.u.]	-0.02	-0.05	-0.06	-0.31	-0.30	-0.34	-0.34	-0.30	-0.35
	m	[a.u.]	-0.08	-0.22	-0.23	-0.28	-0.30	-0.34	-0.29	-0.27	-0.34
oxy	ΔR_f	[a.u.]	-0.04	0.09	0.11	-0.51	-0.37	-0.53	-0.54	-0.29	-0.55
	t_n	[s.]	0.59	0.29	0.18	-0.14	0.14	0.16	-0.18	0.19	0.21
	ΔR_n	[a.u.]	-0.12	-0.14	-0.13	-0.43	-0.45	-0.50	-0.44	-0.42	-0.51
	m	[a.u.]	0.00	-0.10	-0.14	-0.25	-0.27	-0.25	-0.30	-0.30	-0.29

Table D.9
Correlation coefficients between sEMG parameters and NIRS parameters using data of both 50% and 75% hand grip isometric exercise levels (bold font indicates $P<0.05$)

				RMS		Mean Frequency			Median Frequency		
			Duration [s.]	% Change	Slope [%/s.]	% Change	Slope [Hz/s.]	Slope [%/s.]	% Change	Slope [Hz/s.]	Slope [%/s.]
Duration		[s.]	1.00	**0.43**	0.05	0.14	**0.69**	**0.79**	0.09	**0.69**	**0.78**
$\triangle$[Hb]	ΔR_f	[a.u.]	0.14	0.11	0.02	0.24	0.32	0.35	0.21	0.23	0.32
	t_n	[s.]	**0.56**	**0.44**	0.22	0.18	**0.52**	**0.52**	0.21	**0.56**	**0.54**
	ΔR_n	[a.u.]	0.03	0.26	0.27	0.15	0.29	0.21	0.13	0.23	0.18
	m	[a.u.]	-0.33	-0.05	0.08	-0.11	-0.25	-0.30	-0.10	-0.25	-0.28
$\triangle$[HbO$_2$]	ΔR_f	[a.u.]	0.10	-0.29	-0.30	-0.20	-0.11	-0.08	-0.18	-0.03	-0.07
	t_n	[s.]	**0.50**	**0.50**	0.28	0.15	**0.46**	**0.45**	0.21	**0.50**	**0.48**
	ΔR_n	[a.u.]	0.12	-0.09	-0.14	0.19	0.09	0.14	0.19	0.12	0.15
	m	[a.u.]	0.40	0.08	-0.13	0.12	0.29	0.34	0.15	0.33	0.35
oxy	ΔR_f	[a.u.]	-0.06	-0.24	-0.18	-0.26	-0.25	-0.25	-0.25	-0.19	-0.25
	t_n	[s.]	**0.50**	0.39	0.19	0.08	**0.43**	**0.43**	0.13	**0.47**	**0.45**
	ΔR_n	[a.u.]	0.01	-0.18	-0.21	0.02	-0.12	-0.06	0.03	-0.08	-0.05
	m	[a.u.]	0.38	0.08	-0.11	0.12	0.27	0.33	0.13	0.29	0.33

REFERENCES

1. Schmidt, F. E. W., *Development of a Time-Resolved Optical Tomography System for Neonatal Brain Imaging*. PhD thesis, University College London (UCL), 1999.

2. Branco, G., *The development and evaluation of head probes for optical imaging of the infant head*. PhD thesis, University College London (UCL), 2007.

3. Bolin, F. P., L. E. Preuss, R. C. Taylor, and R. J. Ference, "Refractive index of some mammalian tissues using a fiber optic cladding method," *Appl. Opt.*, Vol. 28, no. 12, pp. 2297–2303, 1989.

4. van der Zee, P., *Measurement and modelling of optical properties of human tissue in the near infrared*. PhD thesis, University College London, 1993.

5. Branco, G., *The Development and Evaluation of Head Probes for Optical Imaging of the Infant Head*. PhD thesis, University College London (UCL), 2007.

6. Oregon Medical Laser Center, "http://omlc.ogi.edu/."

7. Patterson, M. S., B. C. Wilson, and D. R. Wyman, "The propagation of optical radiation in tissue ii. optical properties of tissue and resulting fluence distributions," *Lasers Med. Sci.*, Vol. 6, pp. 379 – 390, 1991.

8. Hollis, V. S., *Non-Invasive Monitoring of Brain Tissue Temperature by Near-Infrared Spectroscopy*. PhD thesis, University College London, 2002.

9. Cope, M., *The application of near infrared spectroscopy to non invasive monitoring of cerebral oxygenation in the newborn infant*. PhD thesis, University College London, 1991.

10. Sassaroli, M., and D. L. Rousseau, "Time dependence of near-infrared spectra of photodissociated hemoglobin and myoglobin," *Biochemistry*, Vol. 26, no. 11, pp. 3092–3098, 1987.

11. Cope, M., and D. T. Delpy, "System for long-term measurement of cerebral blood and tissue oxygenation on newborn infants by near infra-red transillumination," *Med. Biol. Eng. Comput.*, Vol. 26, pp. 289–294, May 1988.

12. Chance, B., M. Cope, E. Gratton, N. Ramanujam, and B. Tromberg, "Phase measurement of light absorption and scatter in human tissue," *Review of Scientific Instruments*, Vol. 69, no. 10, pp. 3457–3481, 1998.

13. Delpy, D. T., and M. Cope, "Quantification in tissue near-infrared spectroscopy," *Phil. Tran. R. Soc. Lond. B*, Vol. 352, pp. 649–659, 1997.

14. Wolf, M., M. Ferrari, and V. Quaresima, "Progress of near-infrared spectroscopy and topography for brain and muscle clinical applications," *J. Biomed. Opt.*, Vol. 12, no. 6, p. 062104, 2007.

15. Ito, Y., R. P. Kennan, E. Watanabe, and H. Koizumi, "Assessment of heating effects in skin during continuous wave near infrared spectroscopy," *J. Biomed. Opt.*, Vol. 5, no. 4, pp. 383–390, 2000.

16. Bozkurt, A., and B. Onaral, "Safety assessment of near infrared light emitting diodes for diffuse optical measurements.," *Biomed. Eng. Online*, Vol. 3, p. 9, Mar 2004.

17. Sassaroli, A., and S. Fantini, "Comment on the modified beer-lambert law for scattering media," *Phys. Med. Biol.*, Vol. 49, pp. N255–N257, Jul 2004.

18. Hiraoka, M., M. Firbank, M. Essenpreis, M. Cope, S. R. Arridge, P. van der Zee, and D. T. Delpy, "A monte carlo investigation of optical pathlength in inhomogeneous tissue and its application to near-infrared spectroscopy," *Phys. Med. Biol.*, Vol. 38, no. 12, pp. 1859–1876, 1993.

19. Kocsis, L., P. Herman, and A. Eke, "The modified beer-lambert law revisited," *Phys. Med. Biol.*, Vol. 51, pp. N91–N98, Mar 2006.

20. Duncan, A., T. L. Whitlock, M. Cope, and D. T. Delpy, "Measurement of changes in optical pathlength through human muscle during cuff occlusion on the arm," *Opt. Laser Technol.*, Vol. 27, no. 4, pp. 269–274, 1995.

21. van Beekvelt, M. C., M. S. Borghuis, B. G. van Engelen, R. A. Wevers, and W. N. Colier, "Adipose tissue thickness affects in vivo quantitative near-IR spectroscopy in human skeletal muscle," *Clin. Sci. (Lond.)*, Vol. 101, pp. 21–28, Jul 2001.

22. Yang, Y., O. Soyemi, M. Landry, and B. Soller, "Influence of a fat layer on the near infrared spectra of human muscle: quantitative analysis based on two-layered monte carlo simulations and phantom experiments," *Opt. Express*, Vol. 13, no. 5, pp. 1570–1579, 2005.

23. Lin, L., M. Niwayama, T. Shiga, N. Kudo, M. Takahashi, and K. Yamamoto, "Influence of a fat layer on muscle oxygenation measurement using near-IR spectroscopy: quantitative analysis based on two-layered phantom experiments and Monte Carlo simulation," *Front. Med. Biol. Eng.*, Vol. 10, no. 1, pp. 43–58, 2000.

24. Wang, L., S. L. Jacques, and L. Zheng, "MCML–Monte Carlo modeling of light transport in multi-layered tissues," *Comput. Methods Programs Biomed.*, Vol. 47, pp. 131–146, Jul 1995.

25. Wang, L., S. L. Jacques, and L. Zheng, "Conv - convolution for responses to a finite diameter photon beam incident on multi-layered tissues," *Comput. Methods Programs Biomed.*, Vol. 54, no. 3, pp. 141–150, 1997.

26. Prahl, S. A., M. Keijzer, S. L. Jacques, and A. J. Welch, "A monte carlo model of light propagation in tissue," in *SPIE Proceedings of Dosimetry of Laser Radiation in Medicine and Biology* (Müller, G. J., and D. H. Sliney, eds.), Vol. IS 5, pp. 102–111, 1989.

27. Hamaoka, T., K. K. McCully, V. Quaresima, K. Yamamoto, and B. Chance, "Near-infrared spectroscopy/imaging for monitoring muscle oxygenation and oxidative metabolism in healthy and diseased humans," *J. Biomed. Opt.*, Vol. 12, no. 6, p. 062105, 2007.

28. Quaresima, V., R. Lepanto, and M. Ferrari, "The use of near infrared spectroscopy in sports medicine," *J. Sports Med. Phys. Fitness*, Vol. 43, pp. 1–13, Mar 2003.

29. Boushel, R., H. Langberg, J. Olesen, J. Gonzales-Alonzo, J. Bülow, and M. Kjaer, "Monitoring tissue oxygen availability with near infrared spectroscopy (nirs) in health and disease," *Scand. J. Med. Sci. Sports*, Vol. 11, pp. 213–222, Aug 2001.

30. Boushel, R., and C. A. Piantadosi, "Near-infrared spectroscopy for monitoring muscle oxygenation," *Acta Physiol. Scand.*, Vol. 168, no. 4, pp. 615–622, 2000.

31. Neary, J. P., "Application of near infrared spectroscopy to exercise sports science," *Can. J. Appl. Physiol.*, Vol. 29, no. 4, pp. 488–503, 2004.

32. Ferrari, M., L. Mottola, and V. Quaresima, "Principles, techniques, and limitations of near infrared spectroscopy," *Can. J. Appl. Physiol.*, no. 4, pp. 463–87, 2004.

33. Chance, B., S. Nioka, J. Kent, K. McCully, M. Fountain, R. Greenfeld, and G. Holtom, "Time-resolved spectroscopy of hemoglobin and myoglobin in resting and ischemic muscle," *Anal. Biochem.*, Vol. 174, pp. 698–707, Nov 1988.

34. Patterson, M. S., B. Chance, and B. C. Wilson, "Time resolved reflectance and transmittance for the non-invasive measurement of tissue optical properties," *Appl. Opt.*, Vol. 28, no. 12, pp. 2331–2336, 1989.

35. Cui, W., C. Kumar, and B. Chance, "Experimental study of migration depth for the photons measured at sample surface," in *I. Time resolved spectroscopy and imaging. Proc. Int. Sot. Opt. Eng.*, 1991.

36. Okada, E., M. Firbank, and D. T. Delpy, "The effect of overlying tissue on the spatial sensitivity profile of near-infrared spectroscopy," *Phys. Med. Biol.*, Vol. 40, no. 12, pp. 2093–2108, 1995.

37. Mancini, D. M., L. Bolinger, H. Li, K. Kendrick, B. Chance, and J. R. Wilson, "Validation of near-infrared spectroscopy in humans," *J. Appl. Physiol.*, Vol. 77, no. 6, pp. 2740–2747, 1994.

38. Ding, H., G. Wang, W. Lei, R. Wang, L. Huang, Q. Xia, and J. Wu, "Non-invasive quantitative assessment of oxidative metabolism in quadriceps muscles by near infrared spectroscopy.," *Br. J. Sports Med.*, Vol. 35, pp. 441–444, Dec 2001.

39. Belardinelli, R., T. J. Barstow, J. Porszasz, and K. Wasserman, "Changes in skeletal muscle oxygenation during incremental exercise measured with near infrared spectroscopy," *Eur. J. Appl. Physiol. Occup. Physiol.*, Vol. 70, no. 6, pp. 487–492, 1995.

40. Blangsted, A. K., P. Vedsted, G. Sjøgaard, and K. Søgaard, "Intramuscular pressure and tissue oxygenation during low-force static contraction do not underlie muscle fatigue," *Acta Physiol. Scand.*, Vol. 183, pp. 379–388, Apr 2005.

41. Blasi, R. A. D., M. Ferrari, A. Natali, G. Conti, A. Mega, and A. Gasparetto, "Noninvasive measurement of forearm blood flow and oxygen consumption by near-infrared spectroscopy," *J. Appl. Physiol.*, Vol. 76, pp. 1388–1393, Mar 1994.

42. Homma, S., H. Eda, S. Ogasawara, and A. Kagaya, "Near-infrared estimation of o2 supply and consumption in forearm muscles working at varying intensity," *J. Appl. Physiol.*, Vol. 80, pp. 1279–1284, Apr 1996.

43. Hamaoka, T., H. Iwane, T. Shimomitsu, T. Katsumura, N. Murase, S. Nishio, T. Osada, Y. Kurosawa, and B. Chance, "Noninvasive measures of oxidative metabolism on working human muscles by near-infrared spectroscopy," *J. Appl. Physiol.*, Vol. 81, pp. 1410–1417, Sep 1996.

44. Chance, B., M. T. Dait, C. Zhang, T. Hamaoka, and F. Hagerman, "Recovery from exercise-induced desaturation in the quadriceps muscles of elite competitive rowers.," *Am. J. Physiol.*, Vol. 262, pp. 766–775, Mar 1992.

45. Hamaoka, T., C. Albani, B. Chance, and H. Iwane, "A new method for the evaluation of muscle aerobic capacity in relation to physical activity measured by near-infrared spectroscopy," in *Integration of Medical and Sports Sciences* (Sato, Y., J. Poortmas, I. Hashimoto, and Y. Oshida, eds.), Vol. 37, pp. 421–429, Basel-Karger, 1992.

46. Bhambhani, Y., R. Maikala, and S. Buckley, "Muscle oxygenation during incremental arm and leg exercise in men and women.," *Eur. J. Appl. Physiol. Occup. Physiol.*, Vol. 78, pp. 422–431, Oct 1998.

47. Takaishi, T., K. Ishida, K. Katayama, K. Yamazaki, T. Yamamoto, and T. Moritani, "Effect of cycling experience and pedal cadence on the near-infrared spectroscopy parameters.," *Med. Sci. Sports Exerc.*, Vol. 34, pp. 2062–2071, Dec 2002.

48. Bringard, A., and S. Perrey, "Influence of repeated isometric contractions on muscle deoxygenation and pulmonary oxygen uptake kinetics in humans.," *Clin. Physiol. Funct. Imaging*, Vol. 24, pp. 229–236, Jul 2004.

49. Tachi, M., M. Kouzaki, H. Kanehisa, and T. Fukunaga, "The influence of circulatory difference on muscle oxygenation and fatigue during intermittent static dorsiflexion," *Eur. J. Appl. Physiol.*, Vol. 91, pp. 682–688, May 2004.

50. Yoshitake, Y., H. Ue, M. Miyazaki, and T. Moritani, "Assessment of lower-back muscle fatigue using electromyography, mechanomyography, and near-infrared spectroscopy.," *Eur. J. Appl. Physiol.*, Vol. 84, pp. 174–179, Mar 2001.

51. van Beekvelt, M. C. P., B. G. M. van Engelen, R. A. Wevers, and W. N. J. M. Colier, "In vivo quantitative near-infrared spectroscopy in skeletal muscle during incremental isometric handgrip exercise," *Clin. Physiol. Funct. Imaging*, Vol. 22, no. 3, pp. 210–217, 2002.

52. Hicks, A., S. McGill, and R. L. Hughson, "Tissue oxygenation by near-infrared spectroscopy and muscle blood flow during isometric contractions of the forearm.," *Can. J. Appl. Physiol.*, Vol. 24, pp. 216–230, Jun 1999.

53. Kime, R., T. Hamaoka, T. Sako, M. Murakami, T. Homma, T. Katsumura, and B. Chance, "Delayed reoxygenation after maximal isometric handgrip exercise in high oxidative capacity muscle.," *Eur. J. Appl. Physiol.*, Vol. 89, pp. 34–41, Mar 2003.

54. Praagman, M., H. E. J. Veeger, E. K. J. Chadwick, W. N. J. M. Colier, and F. C. T. van der Helm, "Muscle oxygen consumption, determined by nirs, in relation to external force and emg.," *J. Biomech.*, Vol. 36, pp. 905–912, Jul 2003.

55. Kragelj, R., T. Jarm, T. Erjavec, M. Presern-Strukelj, and D. Miklavcic, "Parameters of postocclusive reactive hyperemia measured by near infrared spectroscopy in patients with peripheral vascular disease and in healthy volunteers," *Ann. Biomed. Eng.*, Vol. 29, pp. 311–320, Apr 2001.

56. McCully, K. K., L. Landsberg, M. Suarez, M. Hofmann, and J. D. Posner, "Identification of peripheral vascular disease in elderly subjects using optical spectroscopy," *J. Gerontol. A Biol. Sci. Med. Sci.*, Vol. 52, pp. B159–B165, May 1997.

57. Komiyama, T., H. Shigematsu, H. Yasuhara, and T. Muto, "Near-infrared spectroscopy grades the severity of intermittent claudication in diabetics more accurately than ankle pressure measurement.," *Br. J. Surg.*, Vol. 87, pp. 459–466, Apr 2000.

58. Kragelj, R., T. Jarm, and D. Miklavcic, "Reproducibility of parameters of postocclusive reactive hyperemia measured by near infrared spectroscopy and transcutaneous oximetry," *Ann. Biomed. Eng.*, Vol. 28, pp. 168–173, Feb 2000.

59. Gratton, E., V. Toronov, U. Wolf, M. Wolf, and A. Webb, "Measurement of brain activity by near-infrared light," *J. Biomed. Opt.*, Vol. 10, no. 1, p. 11008, 2005.

60. Villringer, A., and B. Chance, "Non-invasive optical spectroscopy and imaging of human brain function," *Trends Neurosci.*, Vol. 20, pp. 435–442, Oct 1997.

61. Heffer, E., V. Pera, O. Schutz, H. Siebold, and S. Fantini, "Near-infrared imaging of the human breast: complementing hemoglobin concentration maps with oxygenation images," *J. Biomed. Opt.*, Vol. 9, no. 6, pp. 1152–1160, 2004.

62. Ferrari, M., T. Binzoni, and V. Quaresima, "Oxidative metabolism in muscle," *Philos. Trans. R. Soc. Lond. B Biol. Sci.*, Vol. 352, pp. 677–683, June 1997.

63. Suzuki, S., S. Takasaki, T. Ozaki, and Y. Kobayashi, "Tissue oxygenation monitor using nir spatially resolved spectroscopy," in *Proc. SPIE* (Chance, B., R. R. Alfano, and B. J. Tromberg, eds.), Vol. 3597, pp. 582–592, SPIE, 1999.

64. Delpy, D. T., M. Cope, P. van der Zee, S. Arridge, S. Wray, and J. Wyatt, "Estimation of optical pathlength through tissue from direct time of flight measurement," *Phys. Med. Biol.*, Vol. 33, pp. 1433–1442, Dec 1988.

65. Arridge, S. R., M. Cope, and D. T. Delpy, "The theoretical basis for the determination of optical pathlengths in tissue: temporal and frequency analysis," *Phys. Med. Biol.*, Vol. 37, pp. 1531–1560, Jul 1992.

66. Kienle, A., and T. Glanzmann, "In vivo determination of the optical properties of muscle with time-resolved reflectance using a layered model," *Phys. Med. Biol.*, Vol. 44, no. 11, pp. 2689–2702, 1999.

67. Hunter, R. J., M. S. Patterson, T. J. Farrell, and J. E. Hayward, "Haemoglobin oxygenation of a two-layer tissue-simulating phantom from time-resolved reflectance: effect of top layer thickness," *Phys. Med. Biol.*, Vol. 47, no. 2, pp. 193–208, 2002.

68. Kienle, A., M. S. Patterson, N. Dögnitz, R. Bays, G. Wagniνres, and H. van den Bergh, "Noninvasive determination of the optical properties of two-layered turbid media," *Appl. Opt.*, Vol. 37, no. 4, pp. 779–791, 1998.

69. Fabbri, F., A. Sassaroli, M. E. Henry, and S. Fantini, "Optical measurements of absorption changes in two-layered diffusive media," *Phys. Med. Biol.*, Vol. 49, pp. 1183–1201, Apr 2004.

70. Li, A., R. Kwong, A. Cerussi, S. Merritt, C. Hayakawa, and B. Tromberg, "Method for recovering quantitative broadband diffuse optical spectra from layered media," *Appl. Opt.*, Vol. 46, no. 21, pp. 4828–4833, 2007.

71. Ripoll, J., V. Ntziachristos, J. P. Culver, D. N. Pattanayak, A. G. Yodh, and M. Nieto-Vesperinas, "Recovery of optical parameters in multiple-layered diffusive media: theory and experiments," *J. Opt. Soc. Am. A*, Vol. 18, no. 4, pp. 821–830, 2001.

72. Martelli, F., S. D. Bianco, G. Zaccanti, A. Pifferi, A. Torricelli, A. Bassi, P. Taroni, and R. Cubeddu, "Phantom validation and in vivo application of an inversion procedure for retrieving the optical properties of diffusive layered media from time-resolved reflectance measurements.," *Opt. Lett.*, Vol. 29, pp. 2037–2039, Sep 2004.

73. Martelli, F., A. Sassaroli, S. D. Bianco, and G. Zaccanti, "Solution of the time-dependent diffusion equation for a three-layer medium: application to study photon migration through a simplified adult head model.," *Phys. Med. Biol.*, Vol. 52, pp. 2827–2843, May 2007.

74. Sato, C., M. Shimada, Y. Yamada, and Y. Hoshi, "Extraction of depth-dependent signals from time-resolved reflectance in layered turbid media," *J. Biomed. Opt.*, Vol. 10, no. 6, p. 064008, 2005.

75. Steinbrink, J., H. Wabnitz, H. Obrig, A. Villringer, and H. Rinneberg, "Determining changes in nir absorption using a layered model of the human head," *Phys. Med. Biol.*, Vol. 46, no. 3, pp. 879–896, 2001.

76. Boas, D. A., T. Gaudette, G. Strangman, X. Cheng, J. J. Marota, and J. B. Mandeville, "The accuracy of near infrared spectroscopy and imaging during focal changes in cerebral hemodynamics," *Neuroimage*, Vol. 13, pp. 76–90, Jan 2001.

77. Strangman, G., M. A. Franceschini, and D. A. Boas, "Factors affecting the accuracy of near-infrared spectroscopy concentration calculations for focal changes in oxygenation parameters," *Neuroimage*, Vol. 18, pp. 865 – 879, Apr 2003.

78. Farrell, T. J., M. S. Patterson, and M. Essenpreis, "Influence of layered tissue architecture on estimates of tissue optical properties obtained from spatially resolved diffuse reflectometry," *Appl. Opt.*, Vol. 37, no. 10, pp. 1958–1972, 1998.

79. Okada, E., and D. T. Delpy, "Near-infrared light propagation in an adult head model. ii. effect of superficial tissue thickness on the sensitivity of the near-infrared spectroscopy signal," *Appl. Opt.*, Vol. 42, no. 16, pp. 2915–2922, 2003.

80. Franceschini, M. A., S. Fantini, L. A. Paunescu, J. S. Maier, and E. Gratton, "Influence of a superficial layer in the quantitative spectroscopic study of strongly scattering media," *Appl. Opt.*, Vol. 37, no. 31, pp. 7447–7458, 1998.

81. Homma, S., T. Fukunaga, and A. Kagaya, "Influence of adipose tissue thickness on near infrared spectroscopic signal in the measurement of human muscle," *J. Biomed. Opt.*, Vol. 1, pp. 418–424, 1996.

82. Matsushita, K., S. Homma, and E. Okada, "Influence of adipose tissue on muscle oxygenation measurement with an nirs instrument," in *Proc. SPIE*, Vol. 3194, pp. 159–165, 1998.

83. Matsushita, K., and E. Okada, "Influence of adipose tissue on near infrared oxygenation monitoring in muscle," in *Proc. 20th Ann. Int. Conf. IEEE/EMBS (Hong Kong)*, Vol. 4, pp. 1864–1867, 1998.

84. Yamamoto, K., M. Niwayama, L. Lin, T. Shiga, N. Kudo, and M. Takahashi, "Accurate nirs measurement of muscle oxygenation by correcting the influence of a subcutaneous fat layer," in *Proc. SPIE*, Vol. 3194, pp. 166–173, 1998.

85. Yamamoto, K., M. Niwayama, L. Lin, T. Shiga, N. Kudo, and M. Takahashi, "Near-infrared muscle oximeter that can correct the influence of a subcutaneous fat layer," in *Proc. SPIE*, Vol. 3257, pp. 146–155, 1998.

86. Lin, L., M. Niwayama, T. Shiga, N. Kudo, M. Takahashi, and K. Yamamoto, "Two-layered phantom experiments for characterizing the influence of a fat layer on measurement of muscle oxygenation using nirs," in *Proc. SPIE*, Vol. 3257, pp. 156–166, 1998.

87. Feng, W., D. Haishu, T. Fenghua, Z. Jun, X. Qing, and T. Xianwu, "Influence of overlying tissue and probe geometry on the sensitivity of a near-infrared tissue oximeter," *Physiol. Meas.*, Vol. 22, no. 1, pp. 201–208, 2001.

88. Okada, E., M. Firbank, M. Schweiger, S. R. Arridge, M. Cope, and D. T. Delpy, "Theoretical and experimental investigation of near-infrared light propagation in a model of the adult head," *Appl. Opt.*, Vol. 36, no. 1, pp. 21–31, 1997.

89. Kohl, M., C. Nolte, H. R. Heekeren, S. Horst, U. Scholz, H. Obrig, and A. Villringer, "Determination of the wavelength dependence of the differential pathlength factor from near-infrared pulse signals," *Phys. Med. Biol.*, Vol. 43, no. 6, pp. 1771–1782, 1998.

90. Mayhew, J., Y. Zheng, Y. Hou, B. Vuksanovic, J. Berwick, S. Askew, and P. Coffey, "Spectroscopic analysis of changes in remitted illumination: the response to increased neural activity in brain.," *Neuroimage*, Vol. 10, pp. 304–326, Sep 1999.

91. Uludag, K., M. Kohl, J. Steinbrink, H. Obrig, and A. Villringer, "Cross talk in the Lambert-Beer calculation for near-infrared wavelengths estimated by Monte Carlo simulations," *J. Biomed. Opt.*, Vol. 7, pp. 51–59, Jan 2002.

92. Kohl, M., U. Lindauer, G. Royl, M. Kuhl, L. Gold, A. Villringer, and U. Dirnagl, "Physical model for the spectroscopic analysis of cortical intrinsic optical signals," *Phys. Med. Biol.*, Vol. 45, no. 12, pp. 3749–3764, 2000.

93. Iwasaki, A., and E. Okada, "Influence of cross talk on near-infrared oxygenation monitoring of muscle," in *APBP 2004*, pp. 159–160, 2004.

94. Okui, N., and E. Okada, "Wavelength dependence of crosstalk in dual-wavelength measurement of oxy- and deoxy-hemoglobin," *J. Biomed. Opt.*, Vol. 10, no. 1, p. 11015, 2005.

95. Simpson, C. R., M. Kohl, M. Essenpreis, and M. Cope, "Near-infrared optical properties of ex vivo human skin and subcutaneous tissues measured using the monte carlo inversion technique," *Phys. Med. Biol.*, Vol. 43, no. 9, pp. 2465–2478, 1998.

96. Duck, F. A., *Physical Properties of Tissue: A Comprehensive Reference Book*, Academic Press, 1990.

97. Hamaoka, T., T. Katsumura, N. Murase, S. Nishio, T. Osada, T. Sako, H. Higuchi, Y. Kurosawa, T. Shimomitsu, M. Miwa, and B. Chance, "Quantification of ischemic muscle deoxygenation by near infrared time-resolved spectroscopy," *J. Biomed. Opt.*, Vol. 5, pp. 102–105, Jan 2000.

98. Ding, H., F. Wang, F. Lin, G. Wang, W. Li, and W. Lichty, "Analysis of the sensitivity of reflectance near-infrared tissue oximeter using the methods of simulation and experiment," in *Proc. SPIE*, Vol. 3863, pp. 59–65, 1999.

99. Kienle, A., M. S. Patterson, N. Doegnitz-Utke, R. Bays, G. A. Wagnieres, and H. van den Bergh, "Two-layered turbid media with steady-state and frequency- and time-domain reflectance," in *Proc. SPIE*, Vol. 3194, pp. 269–278, 1998.

100. Niwayama, M., L. Lin, J. Shao, T. Shiga, N. Kudo, and K. Yamamoto, "Quantitative measurement of muscle oxygenation by nirs: Analysis of the influences of a subcutaneous fat layer and skin," in *Proc. SPIE*, Vol. 3597, pp. 291–299, 1999.

101. Essenpreis, M., M. Cope, C. E. Elwell, S. R. Arridge, P. van der Zee, and D. T. Delpy, "Wavelength dependence of the differential pathlength factor and the log slope in time-resolved tissue spectroscopy," *Adv. Exp. Med. Biol.*, Vol. 333, pp. 9–20, 1993.

102. Duncan, A., J. H. Meek, M. Clemence, C. E. Elwell, L. Tyszczuk, M. Cope, and D. T. Delpy, "Optical pathlength measurements on adult head, calf and forearm and the head of the newborn infant using phase resolved optical spectroscopy," *Phys. Med. Biol.*, Vol. 40, pp. 295–304, Feb 1995.

103. van der Zee, P., M. Cope, S. R. Arridge, M. Essenpreis, L. A. Potter, A. D. Edwards, J. S. Wyatt, D. C. McCormick, S. C. Roth, and E. O. Reynolds, "Experimentally measured optical pathlengths for the adult head, calf and forearm and the head of the newborn infant as a function of inter optode spacing," *Adv. Exp. Med. Biol.*, Vol. 316, pp. 143–153, 1992.

104. Niwayama, M., T. Hamaoka, L. Lin, J. Shao, N. Kudo, C. Katoh, and K. Yamamoto, "Quantitative muscle oxygenation measurement using nirs with correction for the influence of a fat layer: comparison of oxygen consumption rates with measurements by other techniques," in *Proc. SPIE*, Vol. 3911, pp. 256 – 265, 2000.

105. Niwayama, M., L. Lin, J. Shao, N. Kudo, and K. Yamamoto, "Quantitative measurement of muscle hemoglobin oxygenation using near-infrared spectroscopy with correction for the influence of a subcutaneous fat layer," *Rev. Sci. Instrum.*, Vol. 71, no. 12, pp. 4571–4575, 2000.

106. Niwayama, M., T. Shiga, L. Lin, N. Kudo, M. Takahashi, and K. Yamamoto, "Correction of the influences of a subcutaneous fat layer and skin in a near-infrared muscle oximeter," in *Proc. 20th Ann. Int. Conf. IEEE/EMBS (Hong Kong)*, Vol. 4, pp. 1849–1850, 1998.

107. Lin, L., Y. Chen, G. Li, J. Gao, and K. Wu, "A novel method for determination of the optical properties of two-layer tissue model from spatially resolved diffuse reflectance," in *Proc. SPIE* (Chance, B., M. Chen, A. E. T. Chiou, and Q. Luo, eds.), Vol. 5630, pp. 486–497, SPIE, 2005.

108. Yang, Y., M. R. Landry, O. O. Soyemi, M. A. Shear, D. S. Anunciacion, and B. R. Soller, "Simultaneous correction of the influence of skin color and fat on tissue spectroscopy by use of a two-distance fiber-optic probe and orthogonalization technique," *Opt. Lett.*, Vol. 30, no. 17, pp. 2269–2271, 2005.

109. Yang, Y., O. Soyemi, P. J. Scott, M. R. Landry, S. M. Lee, L. Stroud, and B. R. Soller, "Quantitative measurement of muscle oxygen saturation without influence from skin and fat using continuous-wave near infrared spectroscopy," *Opt. Express*, Vol. 15, no. 21, pp. 13715–13730, 2007.

110. Geraskin, D., P. Platen, J. Franke, and M. Kohl-Bareis, "Algorithms for muscle oxygenation monitoring corrected for adipose tissue thickness," Vol. 6629, p. 66290P, SPIE, 2007.

111. Geraskin, D., P. Platen, J. Franke, and M. Kohl-Bareis, *Advances in Medical Engineering*, ch. Algorithms for Muscle Oxygenation Monitoring Corrected for Adipose Tissue Thickness, pp. 384–388. Springer proceedings in physics, 2007.

112. Shao, J., L. Lin, M. Niwayama, N. Kudo, and K. Yamamoto, "Determination of a quantitative algorithm for the measurement of muscle oxygenation using cw near-infrared spectroscopy: mean optical pathlength without the influence of the adipose tissue," in *Proc. SPIE*, Vol. 4082, pp. 76–86, July 2000.

113. Ferrari, M., Q. Wei, R. A. D. Blasi, V. Quaresima, and G. Zaccanti, "Variability of human brain and muscle optical pathlength in different experimental conditions," in *Proc. SPIE*, Vol. 1888, pp. 466–472, 1993.

114. Nickell, S., M. Hermann, M. Essenpreis, T. J. Farrell, U. Krämer, and M. S. Patterson, "Anisotropy of light propagation in human skin," *Phys. Med. Biol.*, Vol. 45, pp. 2873–2886, Oct 2000.

115. Binzoni, T., C. Courvoisier, R. Giust, G. Tribillon, T. Gharbi, J. C. Hebden, T. S. Leung, J. Roux, and D. T. Delpy, "Anisotropic photon migration in human skeletal muscle," *Phys. Med. Biol.*, Vol. 51, pp. N79–N90, Mar 2006.

116. van Beekvelt, M. C. P., B. G. M. van Engelen, R. A. Wevers, and W. N. J. M. Colier, "Near-infrared spectroscopy in chronic progressive external ophthalmoplegia: Adipose tissue thickness confounds decreased muscle oxygen consumption," *Ann. Neurol.*, Vol. 51, no. 2, pp. 272–273, 2002.

117. Ferreira, L. F., D. M. Hueber, and T. J. Barstow, "Effects of assuming constant optical scattering on measurements of muscle oxygenation by near-infrared spectroscopy during exercise.," *J. Appl. Physiol.*, Vol. 102, pp. 358–367, Jan 2007.

118. Ferrari, M., Q. Wei, L. Carraresi, R. A. D. Blasi, and G. Zaccanti, "Time-resolved spectroscopy of the human forearm.," *J. Photochem. Photobiol. B*, Vol. 16, pp. 141–153, Oct 1992.

119. Bashkatov, A. N., E. A. Genina, V. I. Kochubey, and V. V. Tuchin, "Optical properties of human skin, subcutaneous and mucous tissues in the wavelength range from 400 to 2000 nm," *J. Phys. D: Appl.Phys.*, Vol. 38, pp. 2543–2555, 2005.

120. Henyey, L., and J. Greenstein, "Diffuse radiation in the galaxy," *Astrophys. J.*, Vol. 93, pp. 70–83, 1941.

121. Coppack, S. W., R. M. Fisher, G. F. Gibbons, S. M. Humphreys, M. J. McDonough, J. L. Potts, and K. N. Frayn, "Postprandial substrate deposition in human forearm and adipose tissues in vivo," *Clin. Sci. (Lond.)*, Vol. 79, pp. 339–348, Oct 1990.

122. Simonsen, L., J. Bulow, and J. Madsen, "Adipose tissue metabolism in humans determined by vein catheterization and microdialysis techniques," *Am. J. Physiol. Endocrinol. Metab.*, Vol. 266, pp. E357–E365, Mar 1994.

123. Silverthon, D. U., *Human Physiology: An Integrated Approach with Interactive Physiology*, Benjamin-Cummings Publishing Company, third ed., 2003.

124. *http://muscle.ucsd.edu/musintro/props.shtml*, Muscle Physiology Home Page of UCSD.

125. Silverthon, D. U., *Human Physiology: an integrated approach*, Prentice Hall, 2001.

126. Ekblom, B., and L. Hermansen, "Cardiac output in athletes," *J. Appl. Physiol.*, Vol. 25, no. 5, pp. 619–625, 1968.

127. Fox, S. I., *Human Physiology*, McGraw-Hill, eight ed., 2004.

128. Vøllestad, N. K., "Measurement of human muscle fatigue," *J. Neurosci. Methods*, Vol. 74, pp. 219–227, Jun 1997.

129. Edwards, R. H., D. K. Hill, D. A. Jones, and P. A. Merton, "Fatigue of long duration in human skeletal muscle after exercise.," *J. Physiol.*, Vol. 272, pp. 769–778, Nov 1977.

130. Kamen, G., and G. E. Caldwell, "Physiology and interpretation of the electromyogram," *J. Clin. Neurophysiol.*, Vol. 13, pp. 366–384, Sep 1996.

131. Basmajian, J. V., and C. J. DeLuca, *Muscles Alive: Their Functions Revealed by Electromyography*, Baltimore MD: William and Wilkins, 5th ed., 1985.

132. Rash, G. S., "Electromyography fundamentals," tech. rep.

133. Webster, J. G., ed., *Medical Instrumentation: Application and Design*, John Wiley & Sons, third ed., 1998.

134. Farina, D., R. Merletti, and R. M. Enoka, "The extraction of neural strategies from the surface EMG," *J. Appl. Physiol.*, Vol. 96, no. 4, pp. 1486–1495, 2004.

135. *http://www.mathworks.com*, MATLAB (MATHWORKS, USA).

136. Blasi, R. A. D., M. Cope, and M. Ferrari, "Oxygen consumption of human skeletal muscle by near infrared spectroscopy during tourniquet-induced ischemia in maximal voluntary contraction.," *Adv. Exp. Med. Biol.*, Vol. 317, pp. 771–777, 1992.

137. Kasikcioglu, E., A. Arslan, B. Topcu, O. Sayli, H. Akhan, H. Oflaz, A. Akin, A. Kayserilioglu, and M. Meric, "Cardiac fatigue and oxygen kinetics after prolonged exercise," *Int. J. Cardiol.*, Vol. 108, pp. 286–288, Apr 2006.

138. Dinler, M., E. Kasikcioglu, A. Akin, O. Sayli, C. Aksoy, A. Oncel, and E. Berker, "Exercise capacity and oxygen recovery half times of skeletal muscle in patients with fibromyalgia," *Rheumatol. Int.*, Vol. 27, pp. 311–313, Jan 2007.

139. Dinler, M., D. Diracoglu, E. Kasikcioglu, O. Sayli, A. Akin, C. Aksoy, A. Oncel, and E. Berker, "Effect of aerobic exercise training on oxygen uptake and kinetics in patients with fibromyalgia," *Rheumatol. Int.*, Sep 2009.

140. Blackwell, J. R., K. W. Kornatz, and E. M. Heath, "Effect of grip span on maximal grip force and fatigue of flexor digitorum superficialis," *Appl. Ergon.*, Vol. 30, pp. 401–405, Oct 1999.

141. Yamaji, S., S. Demura, Y. Nagasawa, and M. Nakada, "Relationships between decreasing force and muscle oxygenation kinetics during sustained static gripping," *J. Physiol. Anthropol. Appl. Human Sci.*, Vol. 23, pp. 41–47, Mar 2004.

142. Montgemery, D. C., and G. C. Runger, *Applied Statistics and Probability for Engineers*, John Wiley & Sons, Inc., third ed., 2003.

143. DeLorey, D. S., J. M. Kowalchuk, and D. H. Paterson, "Relationship between pulmonary o2 uptake kinetics and muscle deoxygenation during moderate-intensity exercise," *J. Appl. Physiol.*, Vol. 95, pp. 113–120, Jul 2003.

144. Felici, F., V. Quaresima, L. Fattorini, P. Sbriccoli, G. C. Filligoi, and M. Ferrari, "Biceps brachii myoelectric and oxygenation changes during static and sinusoidal isometric exercises," *J. Electromyogr. Kinesiol.*, Vol. 19, pp. e1–11, Apr 2009.

145. Moalla, W., G. Dupont, F. Costes, R. Gauthier, Y. Maingourd, and S. Ahmaidi, "Performance and muscle oxygenation during isometric exercise and recovery in children with congenital heart diseases," *Int. J. Sports Med.*, Vol. 27, pp. 864–869, Nov 2006.

146. Nakada, M., S. Demura, S. Yamaji, M. Minami, T. Kitabayashi, and Y. Nagasawa, "Relationships between force curves and muscle oxygenation kinetics during repeated handgrip," *J. Physiol. Anthropol. Appl. Human Sci.*, Vol. 23, pp. 191–196, Nov 2004.

147. Kahn, J. F., J. C. Jouanin, J. L. Bussière, E. Tinet, S. Avrillier, J. P. Ollivier, and H. Monod, "The isometric force that induces maximal surface muscle deoxygenation," *Eur. J. Appl. Physiol. Occup. Physiol.*, Vol. 78, pp. 183–187, Jul 1998.

148. Cheatle, T. R., L. A. Potter, M. Cope, D. T. Delpy, P. D. C. Smith, and J. H. Scurr, "Near-infrared spectroscopy in peripheral vascular disease," *Br. J. Surg.*, Vol. 78, pp. 405–408, Apr 1991.

149. Colier, W. N., I. B. Meeuwsen, H. Degens, and B. Oeseburg, "Determination of oxygen consumption in muscle during exercise using near infrared spectroscopy," *Acta Anaesthesiol. Scand. Suppl.*, Vol. 107, pp. 151–155, 1995.

150. Kooijman, H. M., M. T. Hopman, W. N. Colier, J. A. van der Vliet, and B. Oeseburg, "Near infrared spectroscopy for noninvasive assessment of claudication," *J. Surg. Res.*, Vol. 72, pp. 1–7, Sep 1997.

151. Tamaki, T., S. Uchiyama, T. Tamura, and S. Nakano, "Changes in muscle oxygenation during weight-lifting exercise," *Eur. J. Appl. Physiol. Occup. Physiol.*, Vol. 68, no. 6, pp. 465–469, 1994.

152. Fujii, A., T. Shinogaya, S. Toda, and I. Hayakawa, "Quantification of oxidative metabolism in masseter muscle of denture wearers," *Clin. Oral Investig.*, Vol. 9, pp. 173–179, Sep 2005.

153. Murthy, G., N. J. Kahan, A. R. Hargens, and D. M. Rempel, "Forearm muscle oxygenation decreases with low levels of voluntary contraction," *J. Orthop. Res.*, Vol. 15, pp. 507–511, Jul 1997.

154. Pitcher, J. B., and T. S. Miles, "Influence of muscle blood flow on fatigue during intermittent human hand-grip exercise and recovery," *Clin. Exp. Pharma. and Physiol.*, Vol. 24, pp. 471–476, 1997.

155. Lowery, M., P. Nolan, and M. O'Malley, "Electromyogram median frequency, spectral compression and muscle fibre conduction velocity during sustained submaximal contraction of the brachioradialis muscle," *J. Electromyogr. Kinesiol.*, Vol. 12, pp. 111–118, Apr 2002.

156. Broman, H., G. Bilotto, and C. J. D. Luca, "Myoelectric signal conduction velocity and spectral parameters: influence of force and time," *J. Appl. Physiol.*, Vol. 58, pp. 1428–1437, May 1985.

157. Nagata, S., A. B. Arsenault, D. Gagnon, G. Smyth, and P. A. Mathieu, "Emg power spectrum as a measure of muscular fatigue at different levels of contraction," *Med. Biol. Eng. Comput.*, Vol. 28, pp. 374–378, Jul 1990.

158. Rainoldi, A., G. Galardi, L. Maderna, G. Comi, L. L. Conte, and R. Merletti, "Repeatability of surface emg variables during voluntary isometric contractions of the biceps brachii muscle," *J. Electromyogr. Kinesiol.*, Vol. 9, pp. 105–119, Apr 1999.

159. Zwarts, M. J., and L. Arendt-Nielsen, "The influence of force and circulation on average muscle fibre conduction velocity during local muscle fatigue," *Eur. J. Appl. Physiol. Occup. Physiol.*, Vol. 58, no. 3, pp. 278–283, 1988.

160. Brody, L. R., M. T. Pollock, S. H. Roy, C. J. D. Luca, and B. Celli, "ph-induced effects on median frequency and conduction velocity of the myoelectric signal," *J. Appl. Physiol.*, Vol. 71, pp. 1878–1885, Nov 1991.

161. Kranz, H., A. M. Williams, J. Cassell, D. J. Caddy, and R. B. Silberstein, "Factors determining the frequency content of the electromyogram," *J. Appl. Physiol.*, Vol. 55, pp. 392–399, Aug 1983.

162. Lindström, L., R. Kadefors, and I. Petersén, "An electromyographic index for localized muscle fatigue," *J. Appl. Physiol.*, Vol. 43, pp. 750–754, Oct 1977.

163. Luca, C. J. D., and J. L. Creigh, *Biomechanics, Int. Series on Biomechanics, 5A*, ch. Do the firing statistics of motor units modify the frequency component of the EMG signal during sustained contractions?, pp. 358–362. Human Kinetics Publishers, Inc., 1985.

164. Moritani, T., M. Muro, and T. Takaishi, "Electromyographic analysis of low back pain," *J. Sport Med. Sci.*, Vol. 3, pp. 11–19, 1989.

165. Luca, C. J. D., "The use of surface electromyography in biomechanics," *J. Appl. Biomech.*, Vol. 13, pp. 135–163, 1997.

166. Merletti, R., L. R. L. Conte, and C. Orizio, "Indices of musle fatigue," *J. Electromyog. Kinesiol.*, Vol. 1, pp. 20–33, 1991.

167. Sparto, P., M. Parnianpour, E. Barria, and J. Jagadeesh, "Wavelet and short-time fourier transform analysis of electromyography for detection of back muscle fatigue," *Rehabilitation Engineering, IEEE Transactions on*, Vol. 8, pp. 433–436, September 2000.

168. Arendt-Nielsen, L., and K. R. Mills, "Muscle fibre conduction velocity, mean power frequency, mean emg voltage and force during submaximal fatiguing contractions of human quadriceps," *Eur. J. Appl. Physiol. Occup. Physiol.*, Vol. 58, no. 1-2, pp. 20–25, 1988.

169. Eberstein, A., and B. Beattie, "Simultaneous measurement of muscle conduction velocity and emg power spectrum changes during fatigue," *Muscle Nerve*, Vol. 8, no. 9, pp. 768–773, 1985.

170. Stulen, F. B., and C. J. D. Luca, "The relation between the myoelectric signal and physiological properties of constant-force isometric contractions," *Electroencephalogr. Clin. Neurophysiol.*, Vol. 45, pp. 681–698, Dec 1978.

171. Mortimer, J. T., R. Magnusson, and I. Petersén, "Conduction velocity in ischemic muscle: effect on emg frequency spectrum," *Am. J. Physiol.*, Vol. 219, pp. 1324–1329, Nov 1970.

172. Sjøgaard, G., "Medicine and sport science," pp. 98–109, 1987.

173. Kiens, B., and B. Saltin, "Endurance training of man decreases muscle potassium loss during exercise," *Acta Physiol. Scand.*, Vol. 20A, p. 126, 1986.

174. Madsen, K., P. K. Pedersen, M. S. Djurhuus, and N. A. Klitgaard, "Effects of detraining on endurance capacity and metabolic changes during prolonged exhaustive exercise," *J. Appl. Physiol.*, Vol. 75, pp. 1444–1451, Oct 1993.

175. Milner-Brown, H. S., and R. G. Miller, "Muscle membrane excitation and impulse propagation velocity are reduced during muscle fatigue," *Muscle Nerve*, Vol. 9, pp. 367–374, May 1986.

176. Masuda, K., T. Masuda, T. Sadoyama, M. Inaki, and S. Katsuta, "Changes in surface emg parameters during static and dynamic fatiguing contractions," *J. Electromyogr. Kinesiol.*, Vol. 9, pp. 39–46, Feb 1999.

177. Moritani, T., H. Tanaka, T. Yoshida, C. Ishii, T. Yoshida, and M. Shindo, "Relationship between myoelectric signals and blood lactate during incremental forearm exercise," *Am. J. Phys. Med.*, Vol. 63, pp. 122–132, Jun 1984.

178. Horita, T., and T. Ishiko, "Relationships between muscle lactate accumulation and surface emg activities during isokinetic contractions in man," *Eur. J. Appl. Physiol. Occup. Physiol.*, Vol. 56, no. 1, pp. 18–23, 1987.

179. Allen, D. G., J. A. Lee, and H. Westerblad, "Intracellular calcium and tension during fatigue in isolated single muscle fibres from xenopus laevis," *J. Physiol.*, Vol. 415, pp. 433–458, Aug 1989.

180. Sadoyama, T., T. Masuda, and H. Miyano, "Relationships between muscle fibre conduction velocity and frequency parameters of surface emg during sustained contraction," *European Journal of Applied Physiology and Occupational Physiology*, Vol. 51, no. 2, pp. 247–256, 1983.

181. Zwarts, M. J., T. W. V. Weerden, and H. T. Haenen, "Relationship between average muscle fibre conduction velocity and emg power spectra during isometric contraction, recovery and applied ischemia," *Eur. J. Appl. Physiol. Occup. Physiol.*, Vol. 56, no. 2, pp. 212–216, 1987.

182. Milner-Brown, H. S., and R. B. Stein, "The relation between the surface electromyogram and muscular force," *J. Physiol.*, Vol. 246, pp. 549–569, Apr 1975.

183. Henneman, E., "Relation between size of neurons and their susceptibility to discharge," *Science*, Vol. 126, pp. 1345–1347, Dec 1957.

184. Sadoyama, T., T. Masuda, H. Miyata, and S. Katsuta, "Fibre conduction velocity and fibre composition in human vastus lateralis," *Eur. J. Appl. Physiol. Occup. Physiol.*, Vol. 57, no. 6, pp. 767–771, 1988.

185. Komi, P. V., and P. Tesch, "Emg frequency spectrum, muscle structure, and fatigue during dynamic contractions in man," *Eur. J. Appl. Physiol. Occup. Physiol.*, Vol. 42, pp. 41–50, Sep 1979.

186. Moritani, T., A. Nagata, and M. Muro, "Electromyographic manifestations of muscular fatigue," *Med. Sci. Sports Exerc.*, Vol. 14, no. 3, pp. 198–202, 1982.

187. Moritani, T., M. Muro, and A. Kijima, "Electromechanical changes during electrically induced and maximal voluntary contractions: electrophysiologic responses of different muscle fiber types during stimulated contractions," *Exp. Neurol.*, Vol. 88, pp. 471–483, Jun 1985.

188. Moritani, T., M. Muro, A. Kijima, F. A. Gaffney, and D. Parsons, "Electromechanical changes during electrically induced and maximal voluntary contractions: surface and intramuscular emg responses during sustained maximal voluntary contraction," *Exp. Neurol.*, Vol. 88, pp. 484–499, Jun 1985.

189. Bigland-Ritchie, B. R., N. J. Dawson, R. S. Johansson, and O. C. Lippold, "Reflex origin for the slowing of motoneurone firing rates in fatigue of human voluntary contractions," *J. Physiol.*, Vol. 379, pp. 451–459, Oct 1986.

190. Moritani, T., M. Muro, and A. Nagata, "Intramuscular and surface electromyogram changes during muscle fatigue," *J. Appl. Physiol.*, Vol. 60, pp. 1179–1185, Apr 1986.

191. Kent-Braun, J. A., "Noninvasive measures of central and peripheral activation in human muscle fatigue," *Muscle Nerve Suppl.*, Vol. 5, pp. S98–101, 1997.

192. Milner-Brown, H. S., and R. G. Miller, "Increased muscular fatigue in patients with neurogenic muscle weakness: quantification and pathophysiology," *Arch. Phys. Med. Rehabil.*, Vol. 70, pp. 361–366, May 1989.

193. Barnes, W. S., "The relationship between maximum isometric strength and intramuscular circulatory occlusion," *Ergonomics*, Vol. 23, pp. 351–357, Apr 1980.

194. Lind, A. R., S. H. Taylor, P. W. Humphreys, B. M. Kennelly, and K. W. Donald, "The circulatiory effects of sustained voluntary muscle contraction," *Clin. Sci.*, Vol. 27, pp. 229–244, Oct 1964.

195. Humphreys, P. W., and A. R. Lind, "The blood flow through active and inactive muscles of the forearm during sustained hand-grip contractions.," *J. Physiol.*, Vol. 166, pp. 120–135, Apr 1963.

196. Bonde-Petersen, F., A. L. Mork, and E. Nielsen, "Local muscle blood flow and sustained contractions of human arm and back muscles," *Eur. J. Appl. Physiol. Occup. Physiol.*, Vol. 34, no. 1, pp. 43–50, 1975.

197. Sadamoto, T., F. Bonde-Petersen, and Y. Suzuki, "Skeletal muscle tension, flow, pressure, and emg during sustained isometric contractions in humans," *Eur. J. Appl. Physiol. Occup. Physiol.*, Vol. 51, no. 3, pp. 395–408, 1983.

198. Degens, H., S. Salmons, and J. C. Jarvis, "Intramuscular pressure, force and blood flow in rabbit tibialis anterior muscles during single and repetitive contractions," *Eur. J. Appl. Physiol. Occup. Physiol.*, Vol. 78, pp. 13–19, Jun 1998.

199. Sjøgaard, G., B. R. Jensen, A. R. Hargens, and K. Søgaard, "Intramuscular pressure and emg relate during static contractions but dissociate with movement and fatigue," *J. Appl. Physiol.*, Vol. 96, pp. 1522–9; discussion, Apr 2004.

200. Sjøgaard, G., "Muscle blood flow during isometric activity and its relation to muscle fatigue," *J. Appl. Physiol.*, Vol. 57, pp. 327–335, 1988.

201. Sjøgaard, G., B. Kiens, K. Jørgensen, and B. Saltin, "Intramuscular pressure, emg and blood flow during low-level prolonged static contraction in man," *Acta Physiol. Scand.*, Vol. 128, pp. 475–484, Nov 1986.

202. Sejersted, O. M., A. R. Hargens, K. R. Kardel, P. Blom, O. Jensen, and L. Hermansen, "Intramuscular fluid pressure during isometric contraction of human skeletal muscle," *J. Appl. Physiol.*, Vol. 56, pp. 287–295, Feb 1984.

203. Wigmore, D. M., K. Propert, and J. A. Kent-Braun, "Blood flow does not limit skeletal muscle force production during incremental isometric contractions," *Eur. J. Appl. Physiol.*, Vol. 96, pp. 370–378, Mar 2006.

204. Sahlin, K., M. Tonkonogi, and K. Söderlund, "Energy supply and muscle fatigue in humans," *Acta Physiol. Scand.*, Vol. 162, pp. 261–266, Mar 1998.

205. Vedsted, P., A. K. Blangsted, K. Søgaard, C. Orizio, and G. Sjøgaard, "Muscle tissue oxygenation, pressure, electrical, and mechanical responses during dynamic and static voluntary contractions.," *Eur. J. Appl. Physiol.*, Vol. 96, pp. 165–177, Jan 2006.

206. Byrd, S. K., L. J. McCutcheon, D. R. Hodgson, and P. D. Gollnick, "Altered sarcoplasmic reticulum function after high-intensity exercise," *J. Appl. Physiol.*, Vol. 67, pp. 2072–2077, Nov 1989.

207. Metzger, J. M., and R. L. Moss, "Effects of tension and stiffness due to reduced ph in mammalian fast- and slow-twitch skinned skeletal muscle fibres," *J. Physiol.*, Vol. 428, pp. 737–750, Sep 1990.

208. Pate, E., and R. Cooke, "A model of crossbridge action: the effects of atp, adp and pi," *J. Muscle Res. Cell Motil.*, Vol. 10, pp. 181–196, Jun 1989.

209. Hamaoka, T., T. Osada, N. Murase, T. Sako, H. Higuchi, Y. Kurosawa, M. Miwa, T. Katsumura, and B. Chance, "Quantitative evaluation of oxygenation and metabolism in the human skeletal muscle," *Opt. Rev.*, Vol. 5, pp. 493–497, 2003.

210. Sahlin, K., K. Söderlund, M. Tonkonogi, and K. Hirakoba, "Phosphocreatine content in single fibers of human muscle after sustained submaximal exercise," *Am. J. Physiol.*, Vol. 273, pp. C172–C178, Jul 1997.

211. Kimura, N., T. Hamaoka, Y. Kurosawa, and T. Katsumura, "Contribution of intramuscular oxidative metabolism to total atp production during forearm isomet-

ric exercise at varying intensities," *The Tohoku Journal of Experimental Medicine*, Vol. 208, no. 4, pp. 307–320, 2006.

212. Person, R. S., "Rhythmic activity of a group of human motoneurones during voluntary contraction of a muscle," *Electroencephalogr. Clin. Neurophysiol.*, Vol. 36, pp. 585–595, Jun 1974.

213. Westgaard, R. H., and C. J. de Luca, "Motor unit substitution in long-duration contractions of the human trapezius muscle," *J. Neurophysiol.*, Vol. 82, pp. 501–504, Jul 1999.

214. Luca, C. J. D., "Use of the surface emg signal for performance evaluation of back muscles," *Muscle Nerve*, Vol. 16, pp. 210–216, Feb 1993.

215. Farina, D., R. Merletti, and R. M. Enoka, "The extraction of neural strategies from the surface emg," *J. Appl. Physiol.*, Vol. 96, pp. 1486–1495, Apr 2004.

216. Kumar, D. K., N. D. Pah, and A. Bradley, "Wavelet analysis of surface electromyography to determine muscle fatigue," *IEEE Trans. Neural Syst. Rehabil. Eng.*, Vol. 11, pp. 400–406, Dec 2003.

217. Hampson, N. B., and C. A. Piantadosi, "Near infrared monitoring of human skeletal muscle oxygenation during forearm ischemia," *J. Appl. Physiol.*, Vol. 64, pp. 2449–2457, Jun 1988.

218. Piantadosi, C. A., T. M. Hemstreet, and F. F. Jöbsis-Vandervliet, "Near-infrared spectrophotometric monitoring of oxygen distribution to intact brain and skeletal muscle tissues," *Crit. Care Med.*, Vol. 14, pp. 698–706, Aug 1986.

219. Buono, M. J., P. W. Miller, C. Hom, R. S. Pozos, and F. W. Kolkhorst, "Skin blood flow affects in vivo near-infrared spectroscopy measurements in human skeletal muscle," *Jpn. J. Physiol.*, Vol. 55, pp. 241–244, Aug 2005.

220. Davis, S. L., P. J. Fadel, J. Cui, G. D. Thomas, and C. G. Crandall, "Skin blood flow influences near-infrared spectroscopy-derived measurements of tissue oxygenation during heat stress," *J. Appl. Physiol.*, Vol. 100, pp. 221–224, Jan 2006.

221. Quaresima, V., and M. Ferrari, "Evaluation of the skin blood flow contribution to the non-invasive measurement of muscle oxygenation by near infrared spectroscopy," *J. Physiol. Sci.*, Vol. 56, pp. 267–8; author reply 268, Jun 2006.

222. Ferrari, M., V. Cettolo, and V. Quaresima, "Light source-detector spacing of near-infrared-based tissue oximeters and the influence of skin blood flow," *J. Appl Physiol.*, Vol. 100, p. 1426; author reply 1427, Apr 2006.

223. Yamada, E., T. Kusaka, K. Miyamoto, S. Tanaka, S. Morita, S. Tanaka, Y. Cao, S. Mori, H. Norimatsu, and S. Itoh, "Relationships between changes in oxygenation during exercise and recovery in trained athletes," *Opt. Rev.*, Vol. 5, pp. 436–439, 2003.

224. Hamaoka, T., M. Mizuno, T. Osada, A. Retkevicius, A. N. Nielsen, Y. Nakagawa, T. Katsumura, T. Shimomitsu, and B. Quistorff in *Proc. SPIE*, Vol. 3196, p. 478, 1998.

225. Ömer Şayli, S. Uzun, A. Akın, and B. Çotuk, "Emgaly.1: Grafik kullanici ara yüzlü yüzeyel elektromyografİ İnceleme yazilimi," in *BİYOMUT*, 2007.

226. Georgakis, A., L. Stergioulas, and G. Giakas, "Fatigue analysis of the surface emg signal in isometric constant force contractions using the averaged instantaneous frequency," *Biomedical Engineering, IEEE Transactions on*, Vol. 50, pp. 262–265, Feb. 2003.

227. Ömer Şayli, and A. Akın, "Elektromiyografi (emg) analizinde ortalama anlık frekans parametresinin ortalama ve medyan frekansla beraber kullanımının araştırılması (investigation of the usage of averaged instantaneous frequency parameter along with mean and median frequency in electromyogram (emg) analysis)," in *Signal Processing and Communications Applications Conference, Proceedings of the IEEE 13th*, pp. 597–600, 16-18 May 2005.